INAUGURAL - DISSERTATION

zur

Erlangung der Doktorwürde

der

Naturwissenschaftlich - Mathematischen

Gesamtfakultät

der Ruprecht - Karls - Universität

Heidelberg

vorgelegt von

Dipl.-Phys. Alexander Kaplan

aus Heidelberg

Tag der mündlichen Prüfung: 1. Juni 2011

Hadronic Imaging Calorimetry

Gutachter: Prof. Dr. Hans-Christian Schultz-Coulon
Prof. Dr. Dirk Dubbers

Abstract

This thesis focuses on a prototype of a highly granular hadronic calorimeter at the planned International Linear Collider optimized for the Particle Flow Approach. The $5.3\,\lambda_{\mathrm{int}}$ deep sandwich calorimeter was built by the CALICE collaboration and consists of 38 active plastic scintillator layers. Steel is used as absorber material and the active layers are subdivided into small tiles. In total 7608 tiles are read out individually via embedded Silicon Photomultipliers (SiPM). The prototype is one of the first large scale applications of these novel and very promising miniature photodetectors.

The work described in this thesis comprises the commissioning of the detector and the data acquisition with test beam particles over several months at CERN and Fermilab. The calibration of the calorimeter and the analysis of the recorded data is presented. A method to correct for the temperature dependent response of the SiPM has been developed and implemented. Its successful application shows that it is possible to handle the SiPM temperature dependency in a calorimeter with a large number of channels. The high-resolution 3D image data with analogue energy information are used to study properties and composition of hadron showers at a new level of detail. The spatial shower development and the detector response are analyzed. The performance of a clustering algorithm in accessing the electromagnetic component of hadron showers is studied. Simulations with several different Geant 4 models are compared to data and the results are a valuable source of information for future improvement of the models.

Zusammenfassung

Diese Arbeit befasst sich mit einem hoch-granularen Prototyp eines analogen Hadronenkalorimeters für den geplanten Internationalen Linear Collider, welches für den Particle Flow Ansatz optimiert wurde. Das $5.3\,\lambda_{\mathrm{int}}$ Sandwich Kalorimeter wurde von der CALICE Kollaboration gebaut und besteht aus 38 aktiven Plastikszintillatorlagen. Das Absorbermaterial ist Stahl und die aktiven Lagen sind in kleine Kacheln unterteilt. Die insgesamt 7608 Kacheln werden einzeln über eingebaute Silizium Photomultiplier (SiPM) ausgelesen. Der Prototyp ist eine der ersten Anwendungen dieses neuartigen und vielversprechenden Photodetektors in großen Stückzahlen.

Die hier beschriebene Arbeit umfasst die Inbetriebnahme und Datenerfassung über mehrere Monate im Teststrahlbetrieb am CERN und am Fermilab. Die Kalibration des Kalorimeters und die Analyse der aufgenommenen Daten werden präsentiert. Eine Methode um das temperaturabhängige Ansprechverhalten der SiPM zu korrigieren wurde entwickelt und in die Datenrekonstruktion integriert. Ihre erfolgreiche Anwendung zeigt, dass es möglich ist die Temperaturabhängigkeit der SiPM in einem Kalorimeter mit einer großen Anzahl von Kanälen zu beherrschen. Die hochauflösenden 3D Aufnahmen mit analoger Energieinformation werden verwendet um die Eigenschaften von hadronischen Schauern und deren Zusammensetzung auf einem neuen Detaillierungsgrad zu untersuchen. Die räumliche Entwicklung der Schauer und das Ansprechverhalten des Kalorimeters werden analysiert. Die Möglichkeit auf den elektromagnetischen Anteil von hadronischen Schauern mit einem Clustering-Algorithmus zuzugreifen wird untersucht. Simulationen mit unterschiedlichen Geant 4 Modellen werden mit Daten verglichen und sind eine wertvolle Informationsquelle für eine zukünftige Verbesserung der Modelle.

Contents

Contents

1. Introduction

Mankind has always investigated the matter surrounding it in order to gain a deeper understanding of the world. Patterns recognized in the chemical laws led to the discovery of molecules and the atoms they consist of. The observation of atomic disintegration and the investigation of the decay products revealed the subatomic structures. Ways to accelerate the subatomic particles have been found. In experiments beams of particles with known energy and momentum are brought into collision with target objects to be investigated. Conclusions about the target structure and the forces between the particles can be drawn from the relation between the impact parameters and the results of the interaction. Quantum Mechanics describes the behaviour of the particles by wave functions. The structure of an object can only be resolved if the De-Broglie wavelength $\lambda = h/p$ of the projectile is comparable to the target's dimensions. In order to resolve extremely small objects very high momentum is necessary. In inelastic collisions the target object can be excited or new particles can be created if the energy available in the interaction exceeds their rest mass.

Advancements in technology increased the available energies and smaller and smaller structures have been discovered and studied. Today we know that matter consists of leptons and quarks. Three forces play a significant role in the interaction of these elementary particles: the electromagnetic, the weak, and the strong force. They are mediated via the exchange of vector bosons. Photons are the vector bosons of the electromagnetic force, the weak force is mediated by the Z and $W^{\pm}$ bosons and the strong force via the gluons. The theories describing these phenomena are comprised in the Standard Model of particle physics. It is very successful and all its predictions could be observed up to now, except of the missing Higgs boson. The Higgs mechanism delivers an explanation for the particles masses.

However, the Standard Model cannot be the theory of everything. Gravity is the fourth known fundamental force and could not yet be combined with the other forces of the Standard Model. The strength of the gravitational force is not relevant on the scale of elementary particles. However, the reason for the weakness of gravity compared to the other three forces is not understood yet. Some theories suggest the existence of extra-dimensions as the reason. Cosmological observations show that the Standard Model only describes only a tiny fraction of the matter in the universe. Supersymmetry is an extension of the Standard Model that could bring better agreement between the theory of particle physics and cosmological observations.

The phenomena that would give away some secrets of the unknown physics are expected to be observable in collision experiments at very high energies in the TeV range. In order to create conditions allowing the investigation of new physics, very large accelerators and high performance detectors have to be built. High energy particle physics experiments nowadays are big multi-national enterprises bringing together thousands of physicists and engineers from all over the world. At the point of time this thesis is written, the Large Hadron Collider (LHC) at CERN[1] is the largest particle accelerator with the highest energies available for collisions of protons and heavy ions. The experiments at the LHC are discovery machines. Some of the missing pieces to solve the puzzle of understanding the universe such as the Higgs boson, super symmetric particles or maybe even miniature black holes may be discovered there, if they exist. However, protons are brought to collision which are no elementary particles. The energy of the accelerated protons is shared between its constituents, the quarks and gluons. Only a small fraction of the beam energy is available for the reactions between single constituents and the exact initial state is unknown.

Complementary precision measurements will be necessary to understand the new physics. They are possible at a lepton collider in the corresponding energy range, as no substructure or exited states of the leptons are known. The International Linear Collider (ILC) is a planned electron-positron collider with a centre of mass energy of up to 500 GeV in the first stage and up to 1 TeV as possible upgrade. The planned measurements require a jet energy resolution of $3 - 4\,\%$ in order to separate clearly the hadronic decays of the Z and W bosons [1]. One way to achieve this is the Particle Flow Approach. It combines very high spatial resolution of the detector system with sophisticated software algorithms. The energies of the different particles created in the collisions are measured in the best suitable detector subsystem according to the particles' properties. The energy of charged particles is measured in the tracking detector, photons are measured in the electromagnetic calorimeter and neutral hadrons are measured in the combination of the electromagnetic and hadronic calorimeters. The International Large Detector (ILD) is one of the two foreseen experiments at the ILC based on Particle Flow. To be able to separate showers from neutral and charged particles, calorimeters with an unprecedented high granularity are necessary. The CALICE collaboration built several high performance calorimeter prototypes exploring different technologies. Three different approaches for the hadronic calorimeter exist: a digital, a semi-digital and an analogue one. The ILC, the Particle Flow Approach, the ILD concept and the CALICE prototypes are introduced in chapter 3.

This thesis focuses on the Analogue Hadronic Calorimeter (AHCAL) prototype. The AHCAL is an $1\,\mathrm{m}^3$ steel scintillator calorimeter. The core consists of $3 \times 3 \times 0.5\,\mathrm{cm}^3$ cells. Its 7608 channels are read out via Silicon Photomultipliers (SiPM). The AHCAL is one of the first large scale applications of the novel and very promising

---

[1]CERN - Conseil Européen pour la Recherche Nucléaire at the border between France and Switzerland

SiPM photodetectors. In chapter 2, a brief introduction into calorimetry is given. The prototype and the SiPM are described in chapter 4.

The work described in this thesis comprises the commissioning and data acquisition over several months at test beam sites at CERN and FNAL[2]. The beam line and detector setup, the trigger system and the different particles recorded are described in chapter 5.

The calibration of all AHCAL channels is described in chapter 6. Variations in the production and construction of the prototype lead to a non-uniform response over the calorimeter cells. In addition, the SiPM photodetectors show a saturation behaviour at high light intensities. The AHCAL calibration chain aims to compensate these detector effects. In the framework of this thesis, a method to correct for the temperature dependent response of the SiPM has been developed and integrated into the calibration chain.

For the design of high energy physics experiments simulations are of great importance. Realistic modelling of the physical processes taking place in the detectors is required for the choice of technology and material to be used, as well as for the estimation of the optimal detector geometry. Also the development of the reconstruction algorithms such as Particle Flow heavily relies on simulations. However, hadronic interactions in matter are very complex. Several models, each valid in a limited energy range, exist and make partially contradictory predictions. The data measured in the AHCAL prototype give insight in hadronic shower physics with unprecedented high spatial resolution. This allows to test the existing hadronic models and to improve them. This thesis concentrates on different physics models implemented in the Geant 4 Monte Carlo framework which are described in chapter 7.

In chapter 8, the analysis of pion showers in the range from 8 to 80 GeV recorded during the test beam program is presented. An algorithm to determine the position of the first hadronic interaction in the calorimeter is introduced. Its performance has been studied and improved for this analysis. Several different simulation models are compared to data using several variables: the hadronic interaction length in the AHCAL, the detector response, the longitudinal shower development relative to the first hard interaction and the energy deposition in transverse direction.

One of the main reasons for the worse resolution of non-compensating hadronic calorimeters is the energy carried by the highly fluctuating electromagnetic component inside the hadronic showers. A clustering algorithm based on the highly granular energy density information is applied to access the electromagnetic fraction in pion showers. The study of the performance of the algorithm is shown in chapter 9.

---

[2]FNAL - Fermi National Accelerator Laboratory in Illinois, USA

1. Introduction

2. Calorimetry

The word calorimetry was derived from *calor*, the Latin word for heat. In the classical sense, a calorimeter is an instrument to measure heat in biological, chemical or physical processes. Since heat is a form of energy, in a wider sense calorimeters can be seen as devices measuring energy.

In particle physics, calorimeters are used to determine the energy of subatomic particles. This is done in a destructive way: when traversing the calorimeter material, the particles deposit their kinetic energy completely. However, the term calorimeter might be misleading since the energy is not determined from the negligible amount of heat produced in the absorption. The measurement rather bases on the amount of charge or light produced in the particles' reactions with the calorimeter material. As long as the particle energy is high enough, new particles can be created in the reactions with the material. These child particles carry part of their parent's energy and can in turn react and create more particles. This cascade of reactions is also called particle *shower* and lasts until the particles' energy falls below a certain threshold and they are absorbed.

Calorimeters are not only used to measure the energy of particles. They also play an important role in the identification of the particle type. From the behaviour of the particle in the calorimeter and in some cases even from the energy *not deposited*, conclusions on its species can be drawn.

In the past decades calorimetry developed to a special field of instrumentation in high energy particle physics. Here, only a very condensed introduction to the wide field of calorimetry and the science of shower physics is given based on the detailed description in [2] and [3].

2.1. Sampling Calorimeters

One distinguishes between homogeneous and sampling calorimeters. In homogeneous calorimeters, the entire detector volume is used as absorber and as source of the detector signal simultaneously. This results in a high energy resolution because all of the deposited energy can be detected, but is an expensive technique since a huge amount of material with a high purity is needed to contain the particle showers. Sampling calorimeters usually consist of alternating layers of relatively cheap passive absorber material and active detector medium. Figure 2.1 shows a sketch of a sampling calorimeter with the absorber layers in blue and the active layers in green. In the high density absorber (typically iron, copper, lead or uranium) the
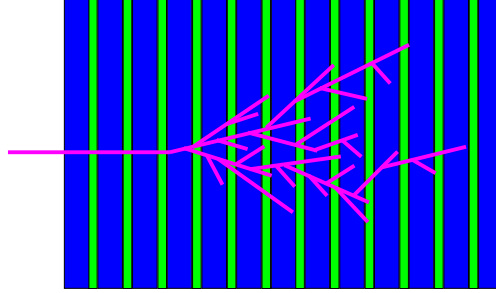
Figure 2.1.: Sketch of a sampling calorimeter consisting of alternating layers of absorber material (blue) and active readout medium (green). A particle is impinging from the left and secondary particles are created in a shower (purple).

particles react and secondary particles are created. Traversing the active material the particles generate light or charge which can be measured. Typical active materials are scintillators, silicon detectors, lead glass or liquid ionization media. Sampling calorimeters are more economic at the price of a worse energy resolution compared to homogeneous calorimeters, since the amount of energy deposited in the absorber varies from event to event and is much larger than the fraction of energy detected in the active layers. This thesis focuses on a sampling calorimeter and some of the characteristics of this calorimeter type will be introduced in the following.

Sampling Fraction

The disadvantage of sampling calorimeters is that the visible energy in the active medium E_{vis} is only a small part of the total energy E_{tot} deposited in the calorimeter. The sampling fraction F is defined as

$$F = E_{\mathrm{vis}}/E_{\mathrm{tot}} \tag{2.1}$$

and is typically in the range of a few percent. The division of the deposited energy into energy loss in the absorber and the visible energy in the active media differs from event to event. This sampling fluctuation degrades the energy resolution.

Landau Fluctuations

Heavy charged particles loose most of their energy via ionization which is described by the Landau distribution. The asymmetry of the Landau distribution additionally degrades the energy resolution. As the sampling fraction is typically quite small, the contribution of the Landau fluctuations can be significant.

Fluctuations of the Path Length

Multiple scattering within the detector volume results in a broad angular distribution of the shower particles. As a consequence, the angle and thus the distance travelled in the active medium varies for every single shower particle. This leads to a fluctuation of the visible energy.

Resolution

For a linear calorimeter response $E_{\text{vis}} = \frac{1}{F} \cdot E_{\text{tot}}$, the energy resolution of a sampling calorimeter as a function of the particle energy can be described as[1]

$$\frac{\sigma}{E} = \frac{a}{\sqrt{E}} \oplus \frac{b}{E} \oplus c. \tag{2.2}$$

The first term $a/\sqrt{E}$ is the contribution of fluctuations, also called the stochastic term. Besides those mentioned above, for hadronic showers additional fluctuations in their electromagnetic component and the invisible energy are important. These phenomena are described later in this chapter. The second term b/E originates from electronic noise. The constant term c is due to incorrect calibration, leakage and other detector effects.

2.2. Electromagnetic Showers

Electromagnetic showers in a calorimeter are governed by the interactions of electrons, positrons and photons in the absorber material. High energy electrons and positrons loose most of their energy by bremsstrahlung. In this process high energy photons are created which in turn generate electrons and positrons in pair production. Such particle cascades are called electromagnetic showers. The multiplicative shower processes alternate until the energy of the particles gets too small and other processes come into play. The most important phenomena in an electromagnetic cascade are summarized in the following.

Electron and Positron Interactions in Matter

Changes in the velocity of a charged particle result in the emission of **bremsstrahlung**, i.e. the radiation of photons with a continuous spectrum. For positrons and electrons above 10 MeV traversing matter, this is the most probable energy loss. By traversing the distance dx in matter, a charged particle with the kinetic energy E looses on average the energy dE due to the emission of bremsstrahlung:

$$-\left\langle \frac{dE}{dx} \right\rangle_{\text{bremsstrahlung}} = \frac{E}{X_0}. \tag{2.3}$$

---

[1]$a \oplus b = \sqrt{a^2 + b^2}$

The radiation length X_0 is the mean distance over which a high-energy electron looses all but $1/e$ of its energy by bremsstrahlung. It is a material property and can be approximated by:

$$X_0 \approx 180 \frac{A}{Z^2} \left[\frac{\text{g}}{\text{cm}^2} \right], \tag{2.4}$$

where A is the atomic weight and Z the number of protons in the nuclei of the medium.

At lower energies ($< 10\,\text{MeV}$), electrons and positrons loose most of their energy by **ionization** and excitation of the atoms in the medium they traverse. A minor part of the energy is also lost in processes like Møller and Bhabba scattering, annihilation $e^+ e^- \rightarrow \gamma\gamma$ and multiple scattering on the absorber nuclei.

The multiplicative shower processes start to slow down when the electrons and positrons loose as much energy in ionization as in bremsstrahlung. This is the case if their kinetic energy reaches the **critical energy** E_c, which is approximately

$$\epsilon_c \approx \frac{550\,\text{MeV}}{Z} \tag{2.5}$$

for an absorber with $Z > 13$.

Interactions of Photons in Matter

Photons of energies above twice the electron rest mass can convert to electron-positron pairs in the field of the absorber nuclei. The process $\gamma \rightarrow e^+ e^-$ is called **pair production** and is dominant for photon energies above $\approx 100\,\text{MeV}$. The mean free path length λ_{pair} a photon travels before pair production takes place is related to the electron radiation length:

$$\lambda_{pair} = \frac{9}{7} X_0. \tag{2.6}$$

Photons with energies in the range $0.1 - 10\,\text{MeV}$ loose most of their energy in **Compton scattering** which is the inelastic scattering with electrons: $\gamma + e^- \rightarrow \gamma + e^-$. Below $0.1\,\text{MeV}$ most photons are absorbed in the **photoelectric effect**: $\gamma + X \rightarrow X'$.

The Molière Radius

A measure for the transverse extension of an electromagnetic shower in the absorber is the Molière radius ρ_M. It is the radius of a cylinder containing 90% of the total shower energy. It can be calculated [2] as

$$\rho_M = m_e c^2 \sqrt{\frac{4\pi}{\alpha}} \frac{X_0}{\epsilon_c}. \tag{2.7}$$

2.3. Muons

The energy of muons is usually not measured with calorimeters. Due to their higher mass compared to electrons, the energy loss of muons by bremsstrahlung is suppressed by a factor of $(m_\mu/m_e)^2 \approx 40000$ [4] and they therefore primarily loose energy by ionization at energies below $100\,\mathrm{GeV}$. They penetrate long distances in matter and are usually not stopped in calorimeters because of their relative long life time. The mean ionization energy loss traversing an absorber with atomic number Z and atomic mass A is described by the Bethe-Bloch equation [5]:

$$-\left\langle \frac{dE}{dx} \right\rangle = Kz^2 \frac{Z}{A} \frac{1}{\beta^2} \left[\frac{1}{2} \ln \frac{2m_e c^2 \beta^2 \gamma^2 T_{\max}}{I^2} - \beta^2 - \frac{\delta}{2} \right]. \tag{2.8}$$

It depends on their charge z of the particles, their velocity $\beta\gamma = p/Mc$, the ionization energy I of the absorber material and the maximum kinetic energy T_{max} that can be imparted to an electron in a single collision. The constant $K = 4\pi N_A r_e^2 m_e c^2$ is a normalization factor and $\delta = \delta(\beta\gamma)$ corrects for relativistic density effects. The equation is valid for velocities $0.1 \lesssim \beta\gamma \lesssim 1000$ and intermediate-Z materials. For muons, the energy dependence of the ionization is almost constant in this range. They have the properties of minimum ionizing particles and can therefore be used for calibration purposes.

2.4. Hadronic Showers

Additionally to the electromagnetic interaction, hadrons are subject to the strong force. For neutral hadrons interacting via the strong force is the only way to deposit energy in the traversed medium (unless they decay before via the weak or electromagnetic force). A charged hadron behaves much the same way as a muon of the same energy and continuously looses energy by ionization. After traversing some depth of material however, a hadron may dramatically change its identity in the strong interaction with a nucleus. Also the struck nucleus is left in an excited state and further interacts. A hadronic shower develops, which is much more complicated than an electromagnetic one, since the variety of processes that may occur both at particle level and those involving the struck nucleus is much larger. Particles produced in the first nuclear interaction may in turn loose their energy by ionization or induce new nuclear reactions. From this point of view, hadron showers are similar to electromagnetic ones. Initially, the number of shower particles increases (multiplication process) as well as the energy deposited in a slice of given thickness. At some depth however, further multiplication is balanced by absorption. Beyond this shower maximum the number of particles and the deposited energy (per slice of matter) decrease. But there are also major differences between electromagnetic and hadronic showers, e.g. in the scale of the shower development, due to different cross sections for nuclear and electromagnetic interactions.

The Nuclear Interaction Length

High-energy hadrons traverse on average one interaction length λ_{int} of absorber material before they interact via the strong force and an hadronic shower starts to develop. The nuclear interaction length is inversely proportional to the total cross section for nuclear interactions:

$$\lambda_{\text{int}} = \frac{A}{N_{\text{A}} \cdot \sigma_{\text{tot}}}, \tag{2.9}$$

where A is the atomic weight of the nuclei in the absorber and N_A is Avogadro's constant. The cross section σ_{tot} depends on the size of the projectile and the size of the nuclei in the absorber material. The nuclear interaction length for pions in steel is therefore larger than the one for protons: $\lambda_{\text{int}}(\pi, \text{Fe}) > \lambda_{\text{int}}(p, \text{Fe})$. The proportionality of the nuclear interaction length on A implies that a pion travels a shorter distance in higher density material, e.g. tungsten: $\lambda_{\text{int}}(\pi, \text{W}) < \lambda_{\text{int}}(\pi, \text{Fe})$.

However, the interaction of the projectile in the target is a statistical process and the probability to travel the distance z before the first hadronic interaction is

$$P(z) = \exp(-z/\lambda_{\text{int}}). \tag{2.10}$$

Equation 2.9 is only valid for pure materials. The effective nuclear interaction length for a structure composited of different materials can be calculated as

$$\frac{1}{\lambda_{\text{int}}} = \sum_k f_k \cdot \frac{1}{\lambda_{\text{int},k}}, \tag{2.11}$$

where $\lambda_{\text{int},k}$ is the interaction length of composite k and f_k its fraction of the total structure depth.

Hadronic Interactions in Matter

Hadrons are compound of quarks and gluons and are no elementary particles. Also the nuclei of the absorber material are composed objects and subject to the strong force. The interaction of hadrons in matter is a complicated multi body interaction via the strong force and no theoretical description comprising all details exists. In general hadronic processes are described in a phenomenological way.

Nuclear Breakup

A high energy hadron can enter a nucleus of the traversed medium and collide with its constituents, the nucleons. In an intra-nuclear cascade new hadrons are created. These particles leave the nucleus and continue to interact in the medium (inter-nuclear cascade). This process is called nuclear breakup or **spallation** and takes place at a time scale in the order of $10^{-22}\,\text{s}$.

De-excitation of the Nuclei

After being hit by an incoming particle, the struck nucleus is left in an exited state. The dominant de-excitation process for lighter nuclei is **evaporation**. In this process protons, neutrons, and smaller nuclei like deuteron, tritium, ^{3}He, and α particles escape from the excited nucleus. When the energy of the exited nucleus falls below the binding energy of a single nucleon, the rest of the energy is released in the emission of photons. Heavier nuclei also de-excite via **nuclear fission**. The nuclear de-excitation happens on a time scale of $10^{-18} - 10^{-13}$ s which is different from the nuclear breakup.

Invisible Energy

In the spallation reactions, a considerable amount of energy is used to release nucleons from the nuclei in which they are bound. This nuclear binding energy does not contribute to the calorimeter signal, it is invisible. This results in a lower calorimeter response for showers caused by hadrons than for electromagnetic showers. On average, 30-40% of the non-electromagnetic shower energy is invisible [3]. Large event-to-event fluctuations in the visible energy are decreasing the precision of hadronic energy measurement in calorimeters.

The Electromagnetic Component

Pions as the lightest hadrons are produced most dominantly in a hadronic cascade. They are produced in equal parts as π^+, π^- and π^0. The π^0s immediately decay into two photons. Hadron showers therefore generally contain an electromagnetic component. The amount of produced π^0s strongly varies from event to event and depends on the processes occurring in the early phase of the shower development (during which their production is energetically possible). The production of π^0s is an irreversible process in the shower development. The photons originating from the decay of the π^0s can only interact electromagnetically and their energy is no longer available for strong interactions. As the total number of particles created in a cascade depends on the energy available, the electromagnetic fraction f_{EM} is a function of the primary particle's energy. It can be described [6] by the parametrization

$$f_{\text{EM}} = 1 - \left(\frac{E}{E_0} \right)^{(k-1)}. \tag{2.12}$$

The scale factor E_0 corresponds to the energy at which multiple pion production becomes significant. The exponent $(k - 1)$ is related to the average number of secondary particles and the fraction of π^0s among them produced per hadronic interaction. Both E_0 and k must be determined in experiments for a given calorimeter; typical values are $k \approx 0.8$ and $E_0 \approx 1$ GeV for pions in iron [7]. Due to the different calorimeter response to hadrons and electrons, this has important consequences on the energy resolution of hadronic calorimeters discussed below.

2.5. Calorimeter Response

The calorimeter response is the average calorimeter signal divided by the energy of the particle that caused it [3]. The calorimeter response in general is different depending on the incident particle type. In order to quantify the difference in the calorimeter response, minimum ionizing particles (MIPs) can be used as benchmark particles. Real minimum ionizing particles do not exist, but muons are a good approximation for MIPs.

The e/MIP Ratio

For homogeneous calorimeters, the e/MIP ratio is equal to 1. This means, the response to a MIP depositing the energy E in the calorimeter is the same as the response to an electromagnetic shower caused by an incident electron or photon of the energy E. For sampling calorimeters the e/MIP ratio depends on the difference in the Z values for absorber layers and the active layers. It is e/MIP < 1 for $Z_{absorber} > Z_{active}$, e/MIP ≈ 1 for $Z_{absorber} = Z_{active}$ and e/MIP > 1 for $Z_{absorber} < Z_{active}$ [8]. The reason for this are soft photons that are better absorbed in low Z materials than in high Z materials. The e/MIP ratio is energy independent and around 0.9 for a scintillator-steel calorimeter.

The Response to Hadrons

Hadrons not only loose their energy in electromagnetic processes, they are subject to the strong interaction and thus deposit energy in nuclear reactions. This is different from purely electromagnetic showers. As mentioned above, part of the energy is invisibly used as nuclear binding energy. Therefore, the calorimeter signal for an ideal hadron h, i.e. a hadron causing a shower without an electromagnetic component ($f_{EM} = 0$), is in general different from signals caused by muons, electrons or photons: $e/h \neq 1$. As the energy deposited by an ideal hadron is proportional to its energy, the e/h ratio is energy independent. The nuclear interactions of hadrons not only lead to a different calorimeter signal for hadronic showers compared to electromagnetic ones on average. It also decreases the resolution of the hadronic energy measurement, due to the event-by-event fluctuation of the invisible energy fraction - even for ideal hadrons.

Real showers caused by hadrons have an electromagnetic component $f_{EM} \neq 0$. For example, the visible energy $E_{vis}(\pi)$ deposited by a pion can be written [2] as

$$E_{vis}(\pi) = f_{EM} \cdot E_{vis}(e) + (1 - f_{EM}) \cdot E_{vis}(h), \tag{2.13}$$

where $E_{vis}(e)$ and $E_{vis}(h)$ are the visible energy deposited by the electromagnetic shower fraction and the purely hadronic fraction, respectively. The ratio

$$e/\pi = \frac{E_{vis}(e)}{E_{vis}(\pi)} = \frac{e/h}{1 - f_{EM} \cdot (1 - e/h)} \tag{2.14}$$

is energy dependent because of the energy dependence of f_{EM}. The average calorimeter response to real hadronic showers is therefore energy dependent and differs from the one to electromagnetic showers. The energy resolution is degraded by fluctuations in the amount of invisible energy and additionally by fluctuations of the amount of energy used for the electromagnetic fraction.

Compensation

Calorimeters fulfilling the condition $e/h = 1$ are called *compensating calorimeters*. Compensating calorimeters do not suffer from the fluctuations of the electromagnetic shower component and the fluctuations of the invisible energy. One can realise the compensation condition of a calorimeter by enhancing the hadronic signal or attenuating the signal caused by the electromagnetic shower part. The neutrons generated in the cascade process are usually not detected and do not contribute to the hadronic signal. An increase of the hadronic shower component can therefore be achieved converting the neutrons to ionising protons due to scattering in hydrogen-rich materials. Also the use of U^{238} as absorber can lead to compensation since slow neutrons cause nuclear fission and generate a detectable signal this way. The signal caused by the electromagnetic shower part can by reduced shielding the active layers with low Z material. This decreases the contributions of soft photons generated in the cascade.

Compensation can also be achieved after the data acquisition, in so-called *offline* or *software compensation*. It is necessary to measure the electromagnetic shower fraction event-wise for this. If the sharing between the electromagnetic and hadronic shower component is determined successfully, compensation can be achieved by applying a weight factor e/h to the portion of the signals generated by the hadronic shower components.

The radiation length for electrons and positrons is much shorter than the hadronic interaction length. This results in a much denser energy deposition of the electromagnetic sub-showers. Their contribution therefore can be obtained from the spatial shower development and the energy density inside the calorimeter. As electromagnetic showers deposit their energy through relativistic electrons and positrons, the electromagnetic fraction in a hadronic shower can also be determined measuring the Čerenkov light emitted in certain materials [9].

2. Calorimetry

3. Detectors for the International Linear Collider

The LHC at CERN is currently the world largest particle accelerator and is able to collide protons with centre-of-mass energies of up to 14 TeV. New physics phenomena are expected to be discovered by the LHC experiments. However, the protons consist of quarks and gluons - they are no elementary particles. The momenta of the colliding protons are shared between their constituents and the exact initial states of the investigated reactions are unknown. This leads to a large QCD background in the detector signals at LHC. Being elementary particles, leptons can be brought to collision with defined energy and spin orientation. This will enable precision measurements complementary to the LHC measurements which will be necessary to understand the new physics.

The LHC is realised as a ring accelerator in the same tunnel as the former Large Electron-Positron Collider (LEP). LEP was running from 1989 to 2000 and brought electrons and positrons to collision with centre-of-mass energies of up to 209 GeV. The energies achievable for electrons and positrons in a ring accelerator are limited by the losses due to the emitted synchrotron radiation

$$E_{\text{sync}} \propto \frac{E^4}{R \cdot m^4}, \tag{3.1}$$

where E is the energy of the particles, m is their mass, and R the accelerator radius. Due to economic reasons, it is not possible to reach electron energies much higher than at LEP in a ring accelerator.

A linear accelerator is a way to achieve electron positron collisions with energies comparable to the parton-parton energies at the LHC. However, very high acceleration gradients are necessary to build a linear accelerator with a reasonable length. Their realisation is a challenge and new acceleration technology has to be developed for this.

3.1. The International Linear Collider

The International Linear Collider (ILC) is a proposed electron - positron collider. In this section, the ILC is described as it has been defined in the ILC reference design report [10]. It will operate at centre-of-mass energies in the range $200 - 500$ GeV in its first phase. The design foresees also running at the 91 GeV Z-pole for electroweak
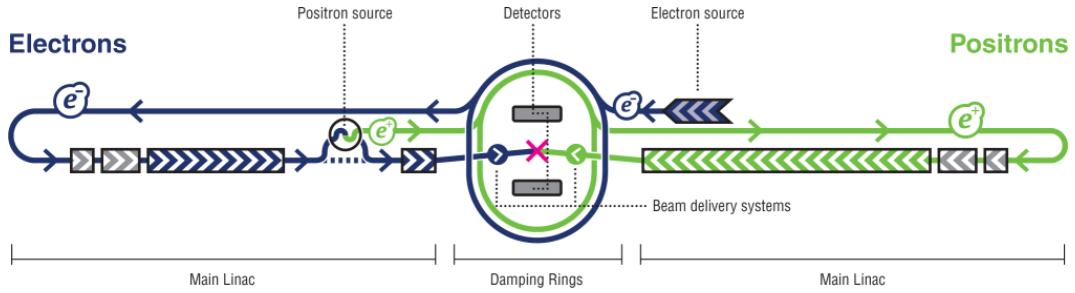
Figure 3.1.: Schematic layout of the planned International Linear Collider [11].

precision measurements. The major next step would be an upgrade to 1 TeV in order to produce higher mass particles. Figure 3.1 shows the schematic layout of the accelerator design.

Electron Acceleration

The electrons are created by laser light hitting onto a photocathode inside a direct current (DC) gun where they are accelerated to 150 keV [12]. In the second step they are accelerated to 76 MeV in a system of cavities via a radio frequency (RF) electromagnetic field and the bunch structure is created. They are then further accelerated to 5 GeV in super-conducting RF structures. After leaving their source the electrons are filled into the damping rings where synchrotron radiation is induced via superconducting wigglers to reduce the beam jitter and the beam emittance. The electron bunch trains are transported to the main accelerator via the ring-to-main-linac (RTML). In the RTML, they are further accelerated to 15 GeV and the orientation of the beam polarisation is adjusted, the beam halo reduced, and the bunch length compressed. In the 11 km long main linac, the electrons are accelerated to their final energy in superconducting niobium cavities. Figure 3.2 shows one of the cavities which has been developed in the R&D program of the TESLA[1] collaboration. They are operated at 1.3 GHz RF and reach an acceleration gradient of 31.5 MeV/m. About 17000 of such cavities will be necessary for the construction of the ILC. The same technology is currently in operation in the free electron laser FLASH[2] which is the pilot facility for the XFEL[3] at DESY.

Positron Acceleration

In Order to generate the positrons, electrons with a energy of 150 GeV are extracted from the main linac and sent through a 150 m helical undulator which consists of a periodic structure of dipole magnets. In the helical field of the undulator, the

---

[1]TESLA - Tera Electron-Volt Energy Superconducting Linear Accelerator
[2]FLASH - Free electron LASer in Hamburg
[3]XFEL - X-Ray Free-Electron Laser

Figure 3.2.: A TESLA nine-cell 1.3 GHz superconducting niobium cavity [13].

electrons emit synchrotron radiation which is circularly polarised. These photons hit a titanium alloy target and generate electromagnetic showers. The charged shower particles are accelerated to 125 MeV and the positrons are separated from the electrons and photons. The positrons are further accelerated to 5 GeV before they are injected to the positron damping ring. Similar to the electrons, they are then guided to a RTML and brought to their final collision energy in the main linac.

Beam Collision

In the beam delivery system (BDS), the electrons and positrons are focused to reach the aimed peak luminosity of $2 \cdot 10^{34} \, \mathrm{cm}^{-2} \, \mathrm{s}^{-1}$. The beams are brought to collision under a crossing angle of 14 mrad. There is only one interaction point that is going to be shared alternately by two independent detectors in a push-pull configuration. During the data acquisition with one of the detectors, on the other detector maintenance and repair work can be done. It is planned to collect an integrated luminosity of 500 fb^{-}1 in the first four years of operation.

3.2. The Particle Flow Algorithm

An excellent jet energy resolution is necessary to fully exploit the physics potential of the ILC. The goal is to clearly separate the hadronic decays of Z and W which requires a jet energy resolution comparable to their decay width $\sigma_m/m = 2.7\%$ [1]. For an ILC operation at $0.5 - 1$ TeV di-jet energies in the range $150 - 350$ GeV are expected. In the classical calorimetry approach, the jet energy is obtained from the sum of the total energy deposition in the calorimeters. Neglecting the other terms in equation (2.2), the jet energy resolution is mainly determined by the stochastic term: $\sigma_E/E \approx a/\sqrt{E}$. The aimed jet energy resolution of 2.7% for di-jet energies of 150 GeV would require a stochastic term of $a/\sqrt{E} \lesssim 30\%/\sqrt{E}$. This is not achievable with a traditional calorimetry approach.

The Particle Flow approach combines sophisticated software algorithms with high performance imaging detectors to reach the aimed jet energy resolution. A typical high energy physics detector with an onion like structure consisting of an inner tracking system in a strong magnetic field, followed by an electromagnetic calorimeter (ECAL), and a hadronic calorimeter (HCAL) is foreseen. Depending on their type,

the jet particles are measured in different detector systems. The tracking system has the highest energy resolution up to energies of $\sim 100\,\mathrm{GeV}$ but is only capable of measuring charged particles. Photons are not visible in the tracking system and are measured in the ECAL. Neutral hadrons, to which the tracker is also insensitive, are measured with the ECAL and the HCAL. Different from classical calorimeter measurements, only the energy deposited by the neutral particles in the calorimeters is taken into account. As the charged particles not only leave tracks in the tracker but also deposit energy in the calorimeters, it is very important to separate this contribution from the neutral particle energy. This is possible combining the high resolution image data from the tracker and the calorimeters. A good matching between the tracker and calorimeter information is crucial as wells as a very high transverse and longitudinal granularity of the calorimeters. The calorimeters have to be inside the magnetic field and dead material between the detectors has to be minimized.

Energy Resolution

A jet is a bundle of charged particles, photons and neutral hadrons. On average, roughly $f_\mathrm{c} = 60\%$ of the jet energy is carried by charged particles and is measured with the high resolution σ_trk of the tracking system. Approximately $f_\gamma = 30\%$ of the energy is carried by photons, which are measured with the resolution σ_ECAL of the ECAL. Only about $f_0 = 10\%$ of the jet energy is carried by neutral hadrons and measured in the HCAL which has the worst energy resolution. This leads to a better Particle Flow energy resolution compared to classical approaches, where the total energy is measured inside the calorimeters. The total jet energy resolution for Particle Flow adds up to:

$$\sigma_\mathrm{jet} \;=\; f_\mathrm{c} \cdot \sigma_\mathrm{trk} \;\oplus\; f_\gamma \cdot \sigma_\mathrm{ECAL} \;\oplus\; f_0 \cdot \sigma_\mathrm{HCAL} \;\oplus\; \sigma_\mathrm{conf} \tag{3.2}$$

The confusion term σ_conf comprises the uncertainty of the Particle Flow approach. It depends on the correct identification of neutral particles in a jet and the proper separation of their signal from that of charged particles. The overlap of particle showers in the calorimeters can lead to *missing energy*. If a neutral shower is by mistake assigned to be part of an overlapping charged shower, only the energy measured in the tracking system will be taken into account. The measured energy is smaller than the true energy in this case. The other way around, if part of a charged shower is accidentally split and considered as a neutral shower this leads to *double counting*. The energy of an additional neutral particle would be added to the total energy which is then larger than the true energy.

3.3. The ILD Concept

Initially, four detector concepts have been proposed for the ILC:

- The Global Large Detector (GLD) [14]
- The Large Detector Concept (LDC) [15]
- The Silicon Detector Concept (SiD) [16]
- The Fourth Concept [17]

The GLD and LDC concepts both base on a gaseous Time Projection Chamber (TPC) for the track detection and highly granular calorimeters. It was decided to merge the two concepts into the International Large Detector Concept (ILD) [18]. A silicon track detector instead of a TPC is foreseen in the SiD concept which has similar calorimeter options as the ILD. Both SiD and ILD are optimized for Particle Flow. The Fourth Concept plans to use the Dual Readout Module (DREAM) for calorimeters to achieve the required energy resolution for the ILC. Complementary information from scintillation and Čerenkov light is used by the DREAM calorimeters to measure the electromagnetic fraction in hadronic showers. The compensation of the fluctuation in hadronic showers leads to a considerable improvement of the energy resolution [19].

Figure 3.3 sketches the layout of the ILD concept. The several subdetectors are discussed briefly in the following.

Tracking System

The vertex detector is closest to the interaction point and is required for the flavour tagging of long living b- and c-hadrons [18, 20]. It also contributes to the track reconstruction. The main tracking device is a large volume TPC filled with gas. A high electric field is applied between the end plates of the chamber. Charged particles traversing the volume ionize the gas. Free electrons along their path are created which drift in the electric field towards the anode where they are detected. The TPC is surrounded by silicon tracking systems which contribute to alignment and time stamping.

Electromagnetic Calorimeter

Two highly segmented concepts exist for the ECAL, both using tungsten as absorber [18, 20]. The first uses silicon PIN diodes[4] for the readout. The second one uses scintillator strips and miniature silicon photodetectors for the readout. Prototypes evaluating both concepts have been built and are introduced in section 3.4.

---

[4]PIN diode - a semiconductor device with a wide intrinsic, i.e. pure or only lightly doped, region between the p- and n-doped regions which can be used for particle detection
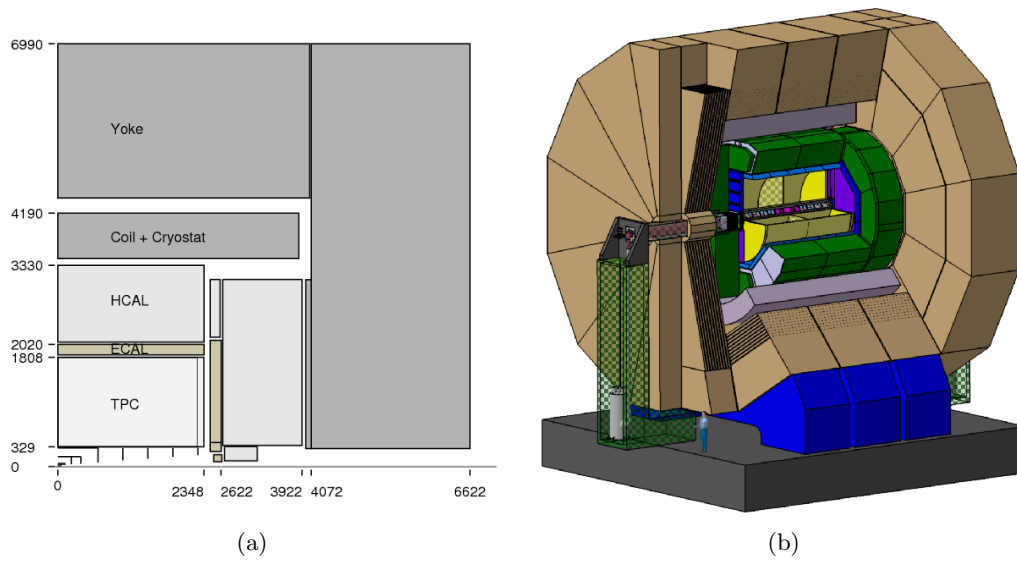
Figure 3.3.: The international large detector concept (ILD). (a) Cross section through one quadrant. (b) Three dimensional detector model. Pictures taken from [18].

Hadronic Calorimeter

The hadronic calorimeter is segmented into 48 layers and uses steel as absorber material [18, 20]. An analogue, a digital and a semi-digital approach for the readout are proposed This thesis focuses on a prototype for the analogue approach. It foresees 3×3 cm^2 scintillator tiles readout via novel miniature photo detectors which are described in detail in chapter 4. The digital and semi-digital approach are based on gaseous detectors and require a calorimeter cell size of 1×1 cm^2.

Muon System

The tracking system and the calorimeters are surrounded by a superconducting coil that creates a magnetic field of 3.5 T [18, 20]. The instrumented iron yoke to return the magnetic flux is used for muon detection and to measure the leakage from the hadronic calorimeter. As readout technology restive plate chambers (RPC) and scintillator strips are evaluated.

3.4. CALICE Research and Development

More than 300 physicists and engineers from over 53 institutes and 16 countries in Europe, Asia, America, and Africa work together in the CALICE[5] collaboration. The goal of the collaboration is the development and comparison of different concepts for calorimeters at a future lepton collider. Various prototypes for ECALs, HCALs and a muon tracker have been built. They were exposed to high energy particles in several test beam campaigns since 2006. In this chapter, the prototypes developed in the CALICE collaboration are briefly introduced.

Electromagnetic Calorimeter Prototypes

Two 30 layer ECAL prototypes using tungsten as absorber have been built by the CALICE collaboration.

The Si-W ECAL is shown in figure 3.4(a). The active front face area is $18 \times 18 \, \text{cm}^2$ and the depth of $20 \, \text{cm}$ corresponds to 24 radiation lengths X_0. It is subdivided into three parts with different sampling structures: the first ten layers have $1.4 \, \text{mm}$ thick absorber plates, followed by ten layers of $2.8 \, \text{mm}$ absorber plates, and the last ten layers of $4.2 \, \text{mm}$ absorber plates. This sampling establishes a high resolution at low energies due to the thin absorber in the first part and a good shower containment at higher energies because of the thicker absorber in the last layers. For the readout of the in total 9720 channels $1 \times 1 \, \text{cm}^2$ silicon PIN diodes are used. The construction of the Si-W ECAL is described in detail in [21].

The ScECAL is depicted in figure 3.4(b). The detector volume of $18 \times 18 \times 22.5 \, \text{cm}^3$ and depth of 21.3 radiation lengths X_0 is comparable to that of the Si-W ECAL. A homogeneous sampling alternating $3 \, \text{mm}$ active layers with $3.5 \, \text{mm}$ tungsten absorber is used. The active layers consist of $4.5 \times 1 \, \text{cm}^2$ scintillator strips readout by Multi Pixel Photon Counters (MPPC)[6] via a wavelength-shifting fibre. In order to achieve a square granularity, the active layers alternate in x- and y-direction. The total number of channels sums up to 2160. More about the ScECAL can be found in [22].

Hadron Calorimeter Prototypes

Besides the analogue HCAL prototype which is the main subject of this thesis and is described in chapter 4, a digital [24] and a semi-digital HCAL concept are studied [25]. In the digital approach, the signal in each calorimeter channel above a certain threshold is counted as a hit without amplitude information. The semi-digital approach has two to three thresholds that can be set giving only very coarse amplitude information. In these concepts a lateral segmentation of $1 \times 1 \, \text{cm}^2$ is required to

---

[5]CALICE - short for Calorimeter for Linear Collider Experiments

[6]MPPC - novel silicon photo detector by Hamamatsu similar to the SiPMs introduced in section 4.2
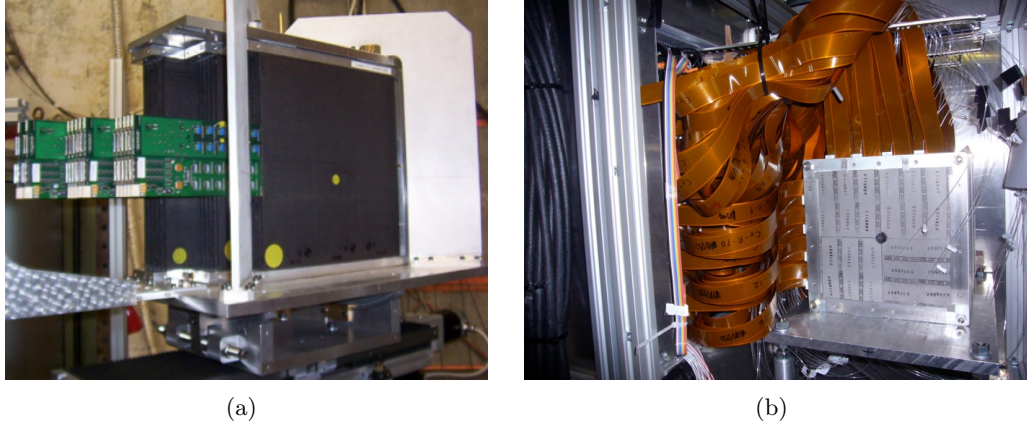
<center>(a)   (b)</center>

Figure 3.4.: Photographs of the silicon (a) and the scintillator (b) ECAL prototypes. Pictures taken from [21] and [23].

reach the required energy resolution. The fine granularity can be realized with different gaseous detector technologies. Prototypes using resistive plate chambers (RPC) [24], gas electron multiplier (GEM) foils [26], and micro mesh gaseous structures (MICROMEGAS) [27] are currently tested.

Tail Catcher and Muon Tracker

The iron yoke to return the magnetic flux is instrumented and used as a muon tracker in the ILD concept. The CALICE collaboration built a prototype of a tail catcher and muon tracker (TCMT) [28]. Figure 3.5 shows a picture of the TCMT in an orange frame on top of its support structure. It is a 16 layer scintillator steel calorimeter realised with the same read out technology as the AHCAL described in chapter 4. However, the TCMT has a different geometry and a much coarser granularity. There are two sampling structures: the first 8 layers consist of 2 cm steel absorber and 0.5 cm scintillator, while the absorber of the last 8 layers is 10 cm. The active layers consist of $100 \times 5\,\text{cm}^2$ scintillator strips with an embedded wavelength shifting fibre in the centre. The orientation of the strips is alternating in horizontal and vertical direction from layer to layer. The TCMT as a depth of 6 interaction lengths λ_{int} and the total number of channels is 320. In the test beam setup, the TCMT is used as an extension of the calorimeter system. Besides tracking muons, it measures the shower energy leaking from the AHCAL. A study on the influence of the magnetic coil size on the energy resolution of the calorimeter system is presented in [28].

Figure 3.5.: Photograph of the CALICE TCMT prototype. Picture taken from [28].

4. The Analogue Hadronic Calorimeter Physics Prototype

The CALICE collaboration built a $1\,\mathrm{m}^3$ analogue hadronic calorimeter (AHCAL) prototype for a possible ILD detector. It is a sandwich calorimeter that consists of steel absorber plates interleaved with 38 highly-segmented active scintillator layers. The scintillator layers are subdivided into small tiles read out individually by embedded Silicon Photomultipliers (SiPM). Custom-designed ASICs[1] amplify and shape the SiPM signals in the front-end part of the data acquisition system. For calibration purposes a versatile LED[2] system has been developed. As a first large scale application of the novel SiPM detectors, the technical goals of the 7608 channel prototype are performance and reliability tests, calibration studies and long term monitoring.

Hadron shower physics at energies in the order of $1 - 100\,\mathrm{GeV}$ can be investigated with an unprecedented level of detail in the $5.3\,\lambda_{\mathrm{int}}$ deep calorimeter and make it is possible to examine the Particle Flow performance with test beam data [29]. The longitudinal segmentation of roughly $1\,X_0$ together with the transverse segmentation of about $1\,\rho_{\mathrm{M}}$ have been chosen in order to be able to resolve the electromagnetic parts in the hadron showers.

This chapter introduces the calorimeter structure, the LED calibration system, the readout chain, and the light detection with SiPMs. A detailed description of the construction and commissioning was published in [30].

4.1. Calorimeter Structure

The AHCAL prototype consists of 30 fine layers in the front and 8 coarse layers in the back. Figure 4.1 shows the layout of a fine AHCAL layer. The core consists of 10×10 small tiles with a surface area of $3 \times 3\,\mathrm{cm}^2$. It is surrounded by three rings of $6 \times 6\,\mathrm{cm}^2$ tiles and closed by one ring of $12 \times 12\,\mathrm{cm}^2$ tiles. For cost reasons the coarse modules have a core of 5×5 tiles with a surface area of $6 \times 6\,\mathrm{cm}^2$. The 216 tiles per fine layer and the 141 tiles per coarse layer sum up to a total of 7608 channels that are individually read out.

The mosaic of scintillator tiles is coated by reflective foil to increase the light collection efficiency. A plastic layer supports the readout cables and light guiding fibres

---

[1]ASIC - Application Specific Integrated Circuit
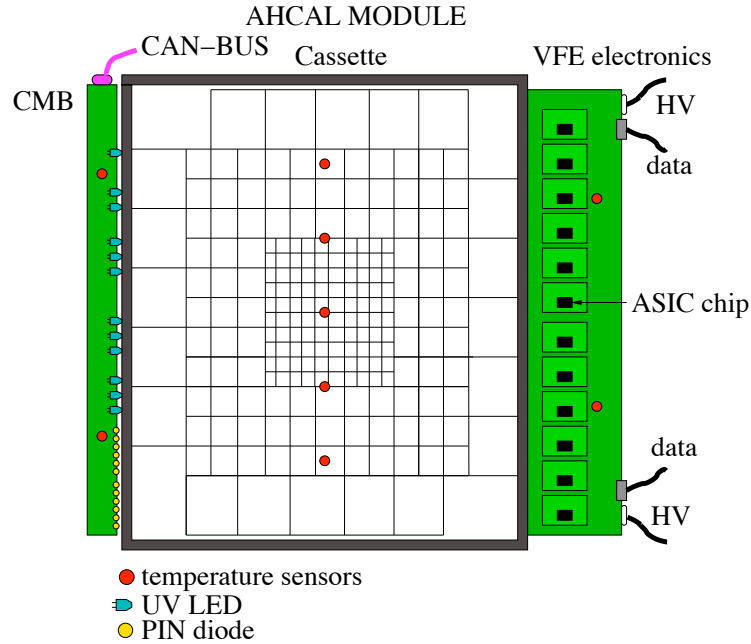[2]LED - light emitting diode

Figure 4.1.: Sketch of one of the finely segmented AHCAL modules. On the left
the Control and Monitoring Board (CMB) is attached. The front-end
electronics board used for the readout is connected on the right. Picture
from [30].

of the LED system. Stainless steel cassettes house the scintillator layers, the cables, the fibres and the support structure; together they are referred to as AHCAL modules. The modules are inserted into gaps between the absorber steel plates. For the correct detector modelling in the Monte Carlo simulation, the AHCAL material composition is important. This is discussed in chapter 7.

The AHCAL prototype discussed in this thesis is not scalable to a full ILD detector. As mentioned above, it is a feasibility study for the SiPM readout of a highly granular calorimeter that allows studies on hadron shower physics which are important for the Particle Flow approach. Therefore it is also called AHCAL *physics prototype*. A *technical prototype* that fulfils the constraints of the ILD design currently is constructed and tested [31].

Single Cell Readout

Figure 4.2 shows a $3 \times 3\,cm^2$ scintillator tile. All scintillator tiles have a thickness of $5\,mm$ to ensure a sufficient amount of light produced by muons used for the MIP calibration. The tile is made of p-terphenyle[3] plus POPOP[4] dissolved in polystyrene

---

[3]p-terphenyle: para 1,4-Diphenylbenzene
[4]POPOP: 1,4-bis(5-phenyloxazol-2-yl)

(BASF130). In order to reduce the light crosstalk between the scintillator tiles, the edges are chemically matted. This results in a white surface which serves a diffuse reflector. In the upper left corner a SiPM is mounted. The bended wavelength-shifting fibre (Kuraray Y11 WLS) collects the light produced in the tile and guides it to the SiPM. A mirror is placed on the other end of the fibre. The reflection of the light increases the amount of light arriving the SiPM surface.
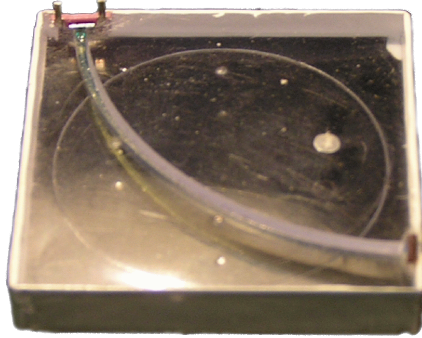

Figure 4.2.: Photograph of a single $3 \times 3 \, \text{cm}^2$ cell from the core of the fine AHCAL layers [32].

4.2. Silicon Photomultiplier

The traditional light detector used in high gain, fast timing, and low noise applications is the photomultiplier tube (or photomultiplier for short). Photoelectrons created by light hitting the photocathode inside a vacuum tube are multiplied in a cascade of acceleration and secondary electron generation steps. Drawbacks of the photomultiplier which is widely used in physical experiments and medial imaging are its bulky shape, disturbance by magnetic fields, and the high operation voltage ($\sim 2 \, \text{kV}$).

In the last years, more and more semiconductor based photo sensors emerged as competitive alternatives for photomultipliers. A relatively novel type of photo detector is the Silicon Photomultiplier (SiPM). The SiPM is an array of avalanche photodiode (APD) pixels on a common silicon substrate operated in Geiger mode. While the single pixels are digital devices, their parallel connection results in an analogue signal proportional to the amount of photons arriving at the SiPM surface. Their high gain (comparable to classical photomultipliers $\sim 10^6$), the small size ($\sim 1 \, \text{mm}^2$ surface), the low bias voltage ($\sim 40 - 80 \, \text{V}$), the low cost, and their insensitivity to magnetic fields (up to $5 \, \text{T}$, [33]) along with a fast timing make them very attractive for applications in detectors in high energy physics, e.g. the ILD calorimeters.

The SiPMs used in the AHCAL were built by MEPHI[5] and the Pulsar Enterprise,

---

[5]Moscow Engineering and Physics Institute

Moscow and have been developed in cooperation with DESY. Lately, many devices similar to the SiPM have become commercially available by Hamamatsu (MPPC), SensL, Photonique, Voxtel, STMicroelectronics, and others. Throughout this thesis, the class of multi pixel Geiger mode avalanche photodiodes will be referred to as SiPM. In the following the working principle, common to all of them, is introduced and the most important characteristics are discussed. More detailed information on the specific SiPM devices applied in the AHCAL can be found in [34] and the references there in.

Working Principle

The AHCAL SiPMs have a photosensitive area of $1 \times 1\,\mathrm{mm}^2$ and consist of 1156 pixels connected in parallel, each $32 \times 32\,\mathrm{\mu m}^2$. Figure 4.3 shows a single pixel in the schematic cross section of a SiPM. The SiPM is operated with a reverse bias voltage above the breakdown voltage. Between the n^+ and p^+ layers forms a high field depletion region ($\sim 105\,\mathrm{V/cm}$). Between the few µm thick p^--doped layer and the low resistive p^+-doped substrate a drift region is created. An electron produced in this region will drift to the high field area and can trigger an avalanche there. A silicon resistor on top connects the n^+ region to the bias terminal and quenches the avalanche. The pixel is surrounded by n^--doped silicon guard rings in order to reduce the electric field on its boarder. This decreases the number of unwanted avalanche breakdowns close to the surface and thus lowers the SiPM dark currents.
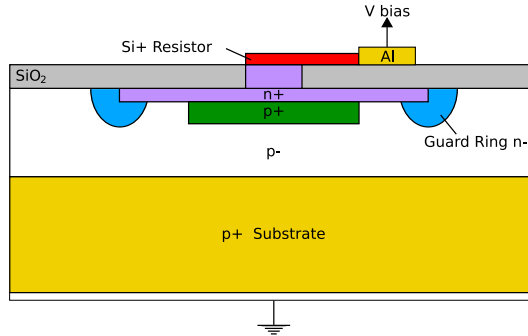

Figure 4.3.: Cross section of a SiPM showing a single pixel [35].

Gain

After the breakdown is triggered, the pixel capacitance C_{pix} discharges from the bias voltage V_{bias} to the break down voltage V_{bd} releasing the charge $Q = C_{\mathrm{pix}} \cdot (V_{\mathrm{bias}} - V_{\mathrm{bd}})$. The gain of the SiPM is the ratio between the released charge Q and the charge of the photo-electron e that triggered the avalanche breakdown:

$$G = \frac{Q}{e} = \frac{C_{\mathrm{pix}}}{e} \cdot (V_{\mathrm{bias}} - V_{\mathrm{bd}}) \tag{4.1}$$

Photon Detection Efficiency

The photon detection efficiency (PDE) is the ratio between the number of detected photons and the number of photons arriving at the SiPM surface. It can be described as:

$$PDE = (1 - R) \cdot \epsilon_{\text{geo}} \cdot \epsilon_{\text{av}} \cdot QE, \tag{4.2}$$

where R is the reflectivity of the surface and ϵ_{geo} the photo-sensitive fraction of the surface area. The avalanche breakdown probability ϵ_{av} is dependent on the over voltage. The quantum efficiency QE for the creation of an electron-hole pair depends on the wavelength of the incident photons and the width of the depletion region.

Dark Rate

As all semiconductor devices, the SiPM is subject to thermal noise which scales with bias voltage and temperature. The thermal noise generates random SiPM signals by initiating avalanche breakdowns independent of any light incidence with a typical *dark rate* of 1-3 MHz for the AHCAL SiPMs at room temperature.

Dynamical Range

The SiPM signal is the sum of the single pixels connected in parallel. The dynamical range of the SiPM therefore depends on the number of pixels. At low light intensities, the number of photons N_γ hitting the surface is small compared to the total number of SiPM pixels N_{pix}. The probability that multiple photons hit the same pixel is negligible and the SiPM signal is proportional to the light intensity. However, at higher light intensities this leads to saturation effects which need to be corrected for (cf. chapter 6.1).

Optical Crosstalk

In the avalanche process photons are generated inside the SiPM pixels which can reach neighbouring pixels and trigger avalanches there. This optical crosstalk depends on the gain and the pixel geometry and can be reduced using optical barriers in the production.

Pixel Dead Time

After an avalanche the SiPM pixel has to recharge until the field in the depletion region is high enough for the next breakdown. This *dead time* is dependent on the pixel capacitance C_{pix} and resistance R_{pix}. Depending on the dead time and the duration of illumination, a pixel can fire more than once during a measurement. This can lead to an increase of the effective number of pixels (cf. chapter 6.1).

4.3. Readout Electronics

Figure 4.4 shows a schematic layout of the AHCAL readout system. The analogue signal from the single SiPMs is guided via coaxial cables to the front-end electronics base boards (attached to the AHCAL modules on the right in figure 4.1). The SiPM signal is amplified and shaped by custom made ASICs on mezzanine boards sitting on the base boards. The base boards are read out via the VME[6] CALICE readout cards (CRC) where the analogue signals are digitized with 16-Bit ADCs[7]. The VME system is connected via an optical link to a standard Linux PC which stores the data on hard disk drives. In the combined test beam operation the ECAL, the AHCAL and the TCMT share the back-end data acquisition via the CRCs, while the front-end electronics is adapted to the individual detectors. The amount of data recorded during a test beam period are too large to be stored on the readout computer. They are transported via the internet to computing centres at DESY and IPNL[8].
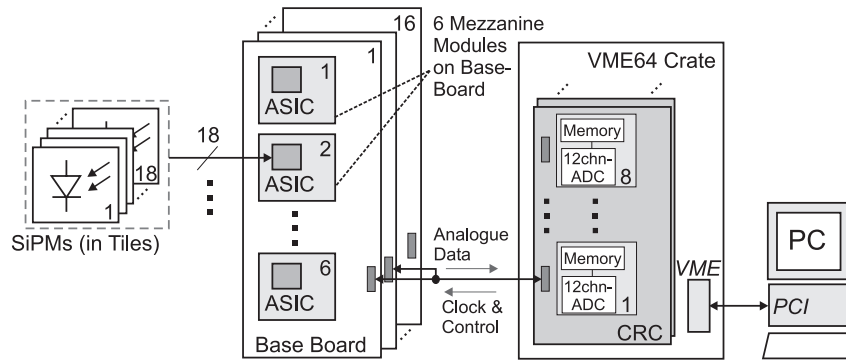

Figure 4.4.: Schematic layout of the AHCAL readout system [30].

ASIC

For the AHCAL a dedicated ASIC has been developed [36] which reads out 18 SiPMs at a time and gives a multiplexed output. Figure 4.5 shows a block diagram of the ASIC chip. The 8-bit DAC[9] allows to modify the single SiPM bias voltages in the range $0 - 5$ V. The amplification can be adjusted via four capacitors in the feedback loop of the variable gain charge preamplifier. A variable CR-RC^2 shaper allows for flexible adjustment of the signal delay and bandwidth.

During the test beam data acquisition the ASIC is operated in two modes. For the gain determination it is operated in the calibration mode for which high electronic amplification and a shaping time of 50 ns is selected to achieve the best possible

---

[6]VME - Versa Module Eurocard
[7]ADC - Analogue to Digital Converter
[8]Institut de Physique Nuclaire de Lyon
[9]DAC - Digital to Analogue Converter

signal-to-noise ratio. The shower data taking as well as the muon calibration are done in the physics mode of the chip. To have an optimal dynamic range, the electronic amplification is smaller by a factor 10 in this mode. A shaping time of 200 ns is used in the physics mode due to latency of the trigger signal. A detailed discussion of the characteristics and the commission of the ASICS and AHCAL readout system can be found in [37].
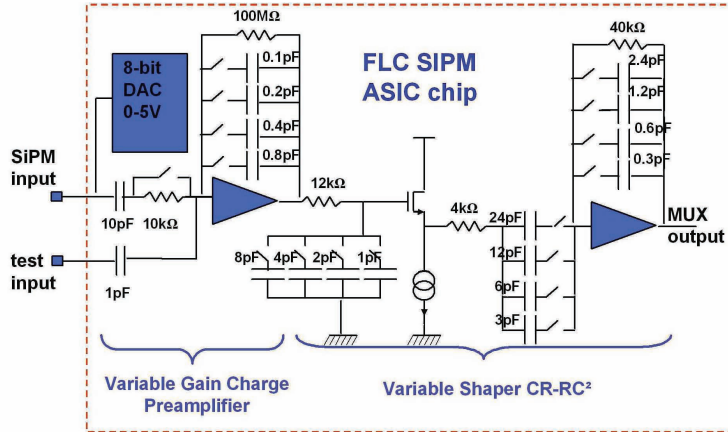

Figure 4.5.: Block diagram of the AHCAL ASIC chip [30].

4.4. LED System

A versatile LED light distribution system was developed to monitor the voltage and temperature dependent signals of the 7608 AHCAL SiPMs. To each AHCAL module a calibration and monitoring board (CMB) is attached from the side (visible on the left in figure 4.1). Each CMB holds 12 UV LEDs and 12 PIN photodiodes. One LED illuminates 18 AHCAL tiles. The light is guided from the LED to the tiles via clear light guide fibres. The purpose of the PIN diodes is to monitor the stability of the LED light.

The CMBs allow for monitoring the performance and long-term stability of the signal from calorimeter cells. It is capable to deliver short ($\sim 10\,\text{ns}$) and low intensity light pulses in a way that only few photons reach the SiPM surface. The single pixel spectra recorded with the low intensity light are necessary for the gain calibration of the SiPMs. It is also possible to shoot high intensity light into the tiles up to full SiPM saturation. This allows for studying the non-linear response of the SiPMs built into the calorimeter. The LED system is also necessary to obtain the inter-calibration factor between the two ASIC modes. The use of the LED light in the AHCAL calibration chain is explained in chapter 6.1. In addition, also the readout of the temperature sensors inside the modules is integrated into the CMBs. More

information about the CMBs and can be found in [38, 30].

5. The CALICE Test Beam Program

In 2006 and 2007, the AHCAL was exposed to particle beams in the range from 8 GeV to 180 GeV. The data acquisition took place in a combined setup with the Si-W ECAL and the TCMT at the SPS H6 test beam line at CERN. After the successful completion of this test beam program, the detectors were moved to Fermilab in spring 2008 to extend the range of particle energies down to 1 GeV. In autumn 2008, the new Scintillator-W ECAL prototype replaced the Si-W ECAL and was operated together with the AHCAL and the TCMT prototypes until summer 2009.

The work for this thesis comprises the commissioning of the AHCAL in summer 2007, the assembly of the complete setup including the trigger system, the drift chambers for beam tracking and the readout electronics in 2008 as well as the operation and maintenance of the detectors throughout the data taking at Fermilab.

This chapter describes the test beam particle generation and the experimental setups at CERN and at Fermilab.

5.1. The Test Beam Program at CERN

After the first combined operation of the partially equipped AHCAL, Si-W ECAL and TCMT in 2006 at CERN [39, 40], the detectors returned to the SPS H6 test beam facility in 2007. For the first time, the AHCAL was fully equipped with 38 active layers and mounted on a moveable stage together with the Si-W ECAL and the VME readout electronics. The photo in figure 5.1 shows the calorimeters in the test beam area.

Particle Generation at the SPS H6 Beam Line

The Super Proton Synchrotron (SPS) is a particle accelerator in the accelerator complex of CERN, measuring 7 km in circumference. The SPS provides beam to the LHC, the COMPASS experiment, the CNGS project and test beam experiments. In the SPS protons, extracted from the Proton Synchrotron (PS), are accelerated up to 450 GeV.

The particles for the H6 test beam line are generated at the T4 Beryllium target station which is sketched in figure 5.2. The protons originating from the SPS are shot onto the target where they interact with the Beryllium nuclei and create secondary particles (mostly pions) with a wide momentum spectrum. The momenta of the
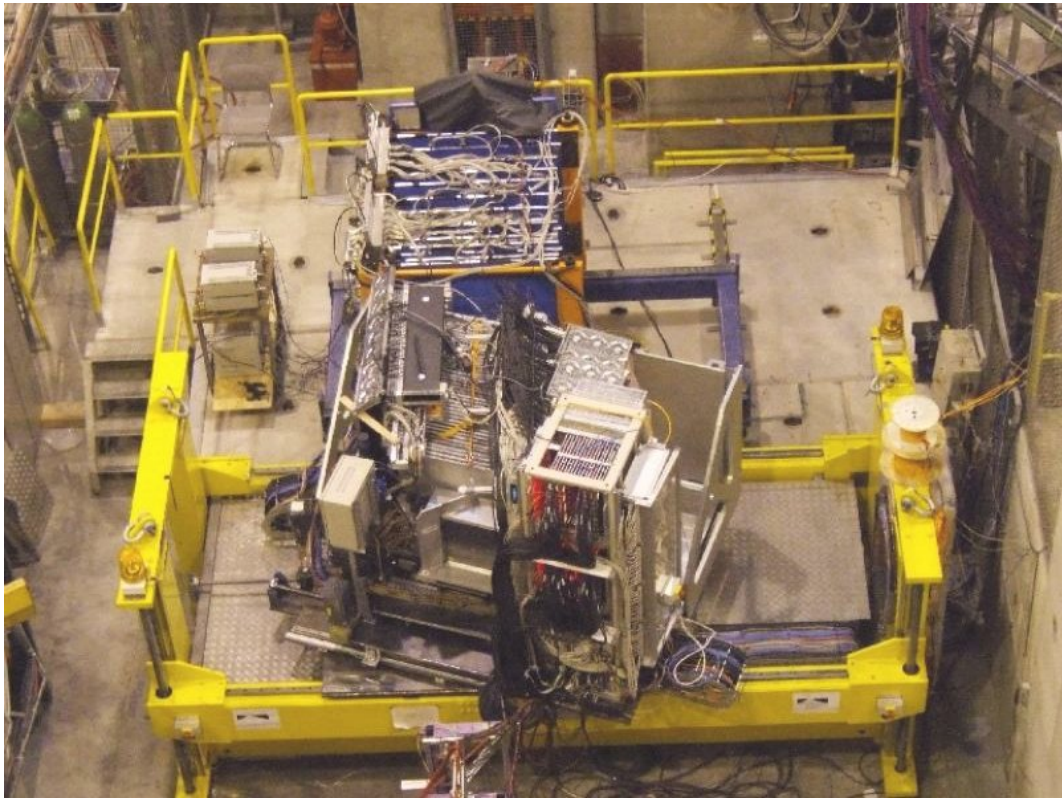
Figure 5.1.: Photograph of the CALICE calorimeters and the moveable stage installed at the CERN test beam site in 2007. The beam is coming from below in the picture. The Si-W ECAL and the AHCAL on the stage are rotated by 30°. The TCMT is place behind the stage.
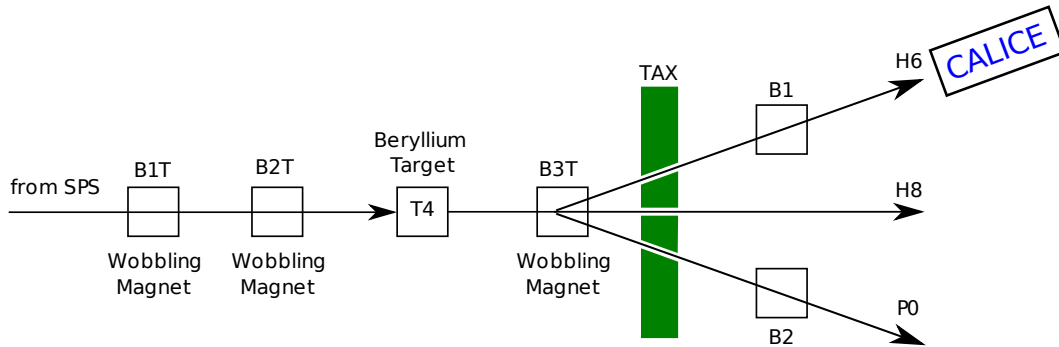
Figure 5.2.: Beam generation for the beam lines P0, H8 and H6.

secondary particles for the three beam lines H6, H8 and P0 are selected with the magnets B1T, B2T and B3T. The TAX blocks limit the beam angle and therefore can control the particle momentum. In addition, they serve as beam dumps. The septum magnets B1 and B2 allow for the acceptance of particles arriving at the H6 and P0 beam lines with a skew or a non-zero angle which is not possible for the H8 beam line.

There are various additional targets available to generate tertiary beams. The electron content of the beam can be increased using a lead target in combination with a spectrometer magnet that selects electrons which loose more energy in lead than pions. The same can be done to increase the positron content. A polyethylene target can be used to lower the pion momentum. After the last target, the charge and momentum selection of the beam is done by a spectrometer magnet. At the H6 beam line a secondary beam is available from $30 - 205$ GeV which can be delivered directly to the experiment. Tertiary beams with energies down to 5 GeV can be obtained. A more detailed description of the test beam facility and the particle generation can be found in [41, 39, 42].

Experimental Setup

The CALICE test beam setup is sketched in figure 5.3. The beam enters from the left. The arrangement of the three calorimeters corresponds to their order in a typical high energy physics experiment. The three calorimeters were ordered as in the cross section through a typical high energy physics detector system: the Si-W ECAL is placed most upstream, followed by the AHCAL and the TCMT in the back. Besides the calorimeters, the setup includes several scintillator counters, drift chambers and a Čerenkov counter.

Čerenkov Counter

The Čerenkov counter consists of an 11 m long Helium vessel and a photo detector inside accepting light emitted under a certain angle. It is placed roughly 30 m upstream from of the calorimeters. Charged particles traversing the volume with a velocity faster then the speed of light in the gas emit Čerenkov light. The angle under which the light is emitted depends on the particle velocity and the refractive index of the gas. The refractive index is determined by the pressure of the gas in the vessel. All particles arrive at the Čerenkov counter with equal momentum. The gas pressure is tuned such that only particles of a certain mass generate a signal. This is used to distinguish particles by their masses. The Čerenkov information on the particle ID is not used in the trigger decision during the data acquisition. It is recorded in the data and can by used in the offline analysis.
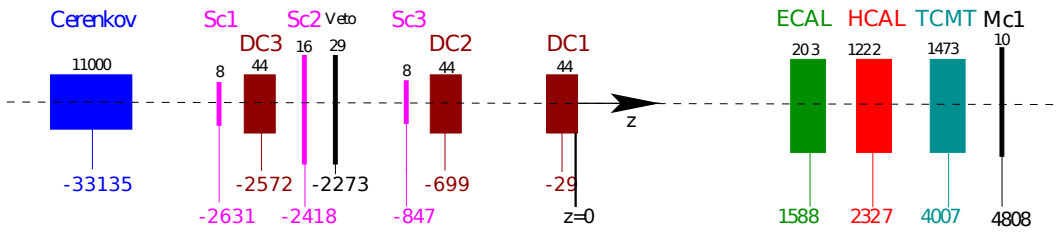

Figure 5.3.: Experimental Setup during the CERN data acquisition in 2007. The beam is entering from left.

Trigger System

The trigger for the experiment is provided by a coincident signal from two 10×10 cm^2 plastic scintillator plates (Sc1 and Sc3), read out by fast photomultiplier tubes. They are positioned centrally on the beam line at a distance of roughly 1.8 m from each other, which limits the acceptance angle for incoming particles.

The 20×20 cm^2 multiplicity scintillator counter (Sc2) is read out by two photomultiplier tubes. For one photomultiplier the signal is discriminated and can be used as digital information in the trigger decision, for the other one the analogue signal is sampled with the same readout electronics as used for the AHCAL. The analogue information is used to tag events where the energy deposited from the incoming beam on the counter is larger than the average signal of one minimum ionizing particle. Events with a signal amplitude in the multiplicity counter larger than twice the average signal of a minimum ionizing particle can be checked on an event display and they confirm the presence of more than one incoming track in the calorimeter system. Such events can be generated from early interaction of the primary beam in air or on the material in the beam line before the trigger system.

The purpose of the 1×1 m ^{2} scintillator plate (labelled Veto) with a central opening

of $20 \times 20 \, \text{cm}^2$ is to detect a possible beam halo.

Muons are tagged by a $1 \times 1 \, \text{m}^2$ scintillator wall (Mc1) in the rear of the detectors. Another muon wall is placed in front of the calorimeters and used in coincidence with Mc1 to enable the acceptance of muon events over the full calorimeter area during the recording of calibration events.

Particle Tracking

The particle trajectories are measured by the three delay wire chambers (DWC) DC1 − DC3. Each consists of two layers with 128 signal wires on high voltage in a gas volume. The working principle is described in [43]. Their signals are readout with a time-to-digital converter (TDC). From the signal arrival times the beam position can be determined with a spatial resolution of $200 \, \mu\text{m}$ in x and y. The centre of the last wire chamber's DC3 exit window defines the origin $(x, y, z) = (0, 0, 0)$ of the CALICE test beam coordinate system.

5.2. The Test Beam Program at Fermilab

After the successful data acquisition at CERN, the CALICE collaboration moved their detectors to the Fermilab Test Beam Facility (FTBF)[1] at the Fermi National Accelerator Laboratory (FNAL) located in Batavia, Illinois. The goal of the Fermilab test beam measurements was to expose the calorimeters to particles with low energies down to 1 GeV and to extend the angular and position scans started at CERN using the moveable stage. In the course of the data collection at FNAL, two different setup were assembled and commissioned: from mid of April till end of July 2008, data was recorded in a combined setup with the Si-W ECAL. From mid of August 2008 till end of May 2009, the ScECAL replaced the Si-W ECAL.

Beam Generation at the Fermilab Test Beam Facility

Figure 5.4 sketches the particle beam generation for the FTBF at the Fermilab accelerator complex. Negative $750 \, \text{keV}$ hydrogen ions (H$^-$) are fed into a linear accelerator (Linac). After leaving the Linac, the electrons are stripped off the H$^-$ ions. The remaining $400 \, \text{MeV}$ protons are accelerated in two steps: the Booster brings them to $8 \, \text{GeV}$ and the Main Injector to $120 \, \text{GeV}$. Afterwards, the particles are either filled into the Tevatron or used for the test beam facility. The FTBF consists of two beam lines (MTest and MCenter). The CALICE calorimeters were installed at the MT6 site at the end of the MTest line.

The instrumentation at the end of MTest beam line is sketched in the bottom of figure 5.4. Secondary particles for the MT6 test beam are created in a $30 \, \text{cm}$ Aluminium

---

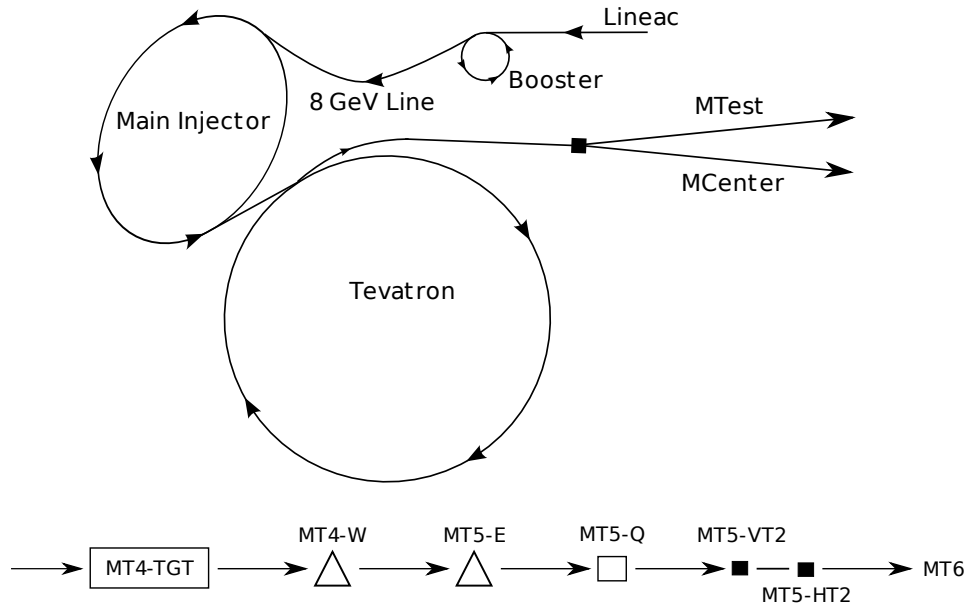[1]FTBF - until recently the known as Meson Test Beam Facility (MTBF)

Figure 5.4.: Sketch of the Fermilab accelerator complex. The CALICE test beam setup was installed at the MTest beam line. Below, a simplified picture of the end of the MTest beam line is shown.

target MT4-TGT. Their momentum is selected via two sets of dipole magnets MT4-W and MT5-E. The beam is focused by the MT5-Q magnets and the beam position is adjusted by trimming magnets, MT5-VT2 and MT5-HT2. For test beam experiments, 120 GeV protons at rates of $1-300$ kHz as well as pions, muons and electrons down to 1 GeV are available. However, especially at lower energies, the beam line instrumentation is not sufficient to generate a pure beam of single particle species. A mixed beam of secondary particles from the inelastic interaction of the protons in the target is delivered to the test beam experiments. The particle type can be tagged with a differential Čerenkov counter described below.

Experimental Setup

Figure 5.5 shows the CALICE test beam setup from April 2008 which was used in the combined data taking with the Si-W ECAL. The same setup was reused in the second data taking period for which the Si-W ECAL was replaced by the ScECAL.

Trigger System

The beam trigger was provided by the two 10×10 cm plastic scintillator counters with fast photomultiplier readout (T10×10A and T10×10B) that have already been in use during the CERN test beam data taking. They were placed at a distance of roughly

CALICE TESTBEAM 2008 FNAL
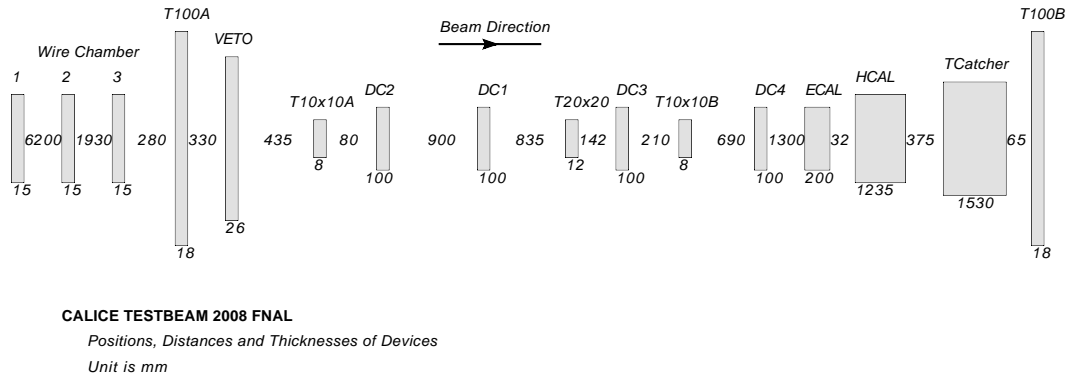*Positions, Distances and Thicknesses of Devices*
Unit is mm

Figure 5.5.: Sketch of the CALICE setup in April 2008

2.5 m apart from each other. The two muon walls (T100A and T100B) are used in coincidence during the muon calibration. They are $1 \times 1\,\mathrm{m}^2$ scintillator plates read out by photomultiplier tubes. After the recording of the muon calibration, T100A is removed to minimize the material in front of the detectors in the beam line. As in the CERN test beam setup, the capability to distinguish events with more than one particle impinging on the calorimeter system is provided by a $20 \times 20\,\mathrm{cm}^2$ scintillator counter (T20 $\times$ 20) which can also be used in the trigger decision. The $1 \times 1\,\mathrm{m}^2$ beam halo detector (VETO) is the same as introduced in section 5.1.

The Differential Čerenkov Detector

The differential Čerenkov detector sketched in figure 5.6(a) and depicted in the photo in figure 5.6(b) is part of the FTBF beam line instrumentation. The volume is filled
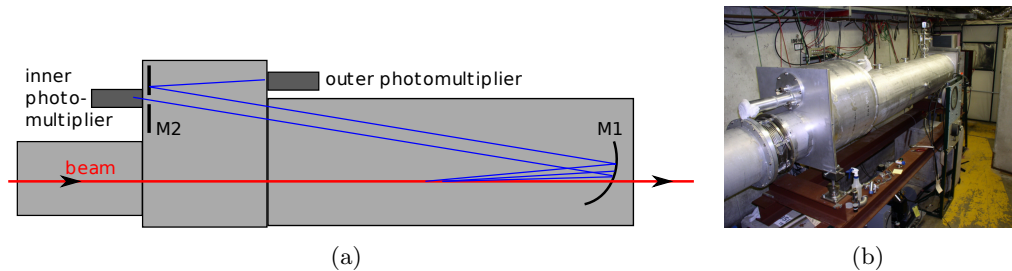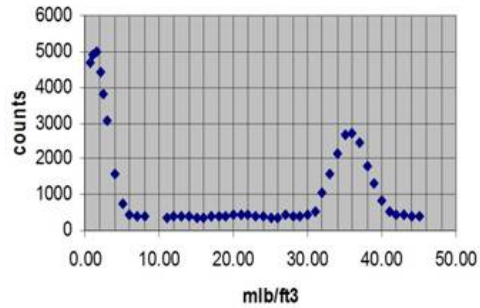

Figure 5.6.: Differential Čerenkov counter as part of the MTest beam line at the Fermilab Test Beam Facility.

with nitrogen gas with an adjustable pressure. Čerenkov light emitted by the beam particles in the gas strikes the objective mirror M1 and is focused to a ring image of radius equal to the Čerenkov angle times the focal length of 2.54 m. The focal plane mirror M2 has an opening in its centre that allows light at angles up to a certain limit

to pass through to the inner photomultiplier tube. Light at larger angles is reflected and collected by the outer photomultiplier. The gas pressure can be adjusted in a way that only particles of a certain velocity emit Čerenkov light under an angle at which it reaches the inner photomultiplier tube. For known beam momentum, this allows for tagging particles of a certain mass. In the differential operation mode, the signal from the outer photomultiplier is placed in anti-coincidence with the inner one. This makes it possible to distinguish more clearly minority particles in the beam. Figure 5.7(a) shows the number of events generating a signal in the differential Čerenkov detector as a function of the gas density for a 8 GeV mixed beam as an example. The right peak is from pions and the one on the left originates from electrons in the beam. Using this density information the pressure in the gas vessel can be adjusted such that the desired particle type is detected by the Čerenkov. More details on the Čerenkov detector can be found in [44].

(a)

Figure 5.7.: Number of events generating a signal in the differential Čerenkov counter as function of the gas density at a 8 GeV mixed beam. Plot taken from [44].

Čerenkov signal in the Trigger Decision

In the former setups at CERN, the Čerenkov information was only recorded and used for the analysis after the data acquisition to purify the data sample. As part of the work for this thesis at Fermilab, the Čerenkov detector was integrated into the trigger decision. The aim was to enhance the low energy pion content and to reject electrons in the recorded events in order to collect as much pion statistics as possible at the given data rates in the limited beam time. Special air core cables were used to route the signals from the Čerenkov counter to the readout electronics as fast as possible. Nevertheless, it was necessary to delay the signal from the two 10×10 scintillator counters which generate the beam trigger by $\sim 66\,\text{ns}$. Figure 5.8(a) shows a simplified sketch of the trigger logic. The data acquisition software had to be extended to integrate the Čerenkov signal into the trigger decision. In order to accept only particles that generate a signal exclusively in the inner and not

in the outer photomultiplier, the Čerenkov pulse has to enclose the beam trigger pulses by few nanoseconds because of the limitations of the programmable trigger logic. The timing was tuned with beam signal using an oscilloscope installed inside the radiation area where no access is possible during the data taking. The picture shown in figure 5.8(b) is a screenshot from the oscilloscope operated in remote control via network access. The oscilloscope was triggered by the purple pulse from T10×10B. The other pulses are from the T10×10A (yellow) and the outer Čerenkov photomultiplier (blue). From the baseline of the blue signal one can see that the veto from the Čerenkov is off for a fraction of the events.
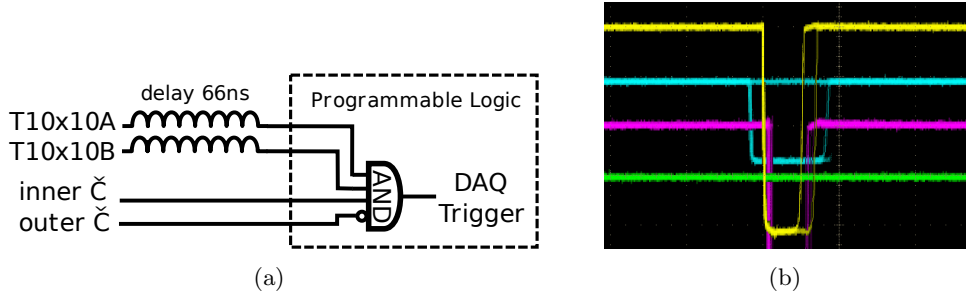

(a)   (b)

Figure 5.8.: Integration of the Čerenkov information into the trigger decision. (a) Simplified sketch of the trigger logic. (b) Screen shot from the oscilloscope showing the NIM pulses from the two 10cm scintillator counter in yellow and purple (20 ns) and the signal from the Čerenkov in blue.

Figure 5.9(a) shows the distribution of the energy deposited in the AHCAL in a mixed beam of 10 GeV positive particles (open histogram) containing mainly positrons. The filled histogram overlaid in the bottom is the energy deposited by protons in the beam which have been separated using the Čerenkov information in the offline analysis. The smaller peak on the very left are muons in the data sample. In figure 5.9(b) three different energy sum distributions are shown. The data have been acquired in three separate runs with mixed beam at 10 GeV using the signal from the Čerenkov detector in the trigger decision. The histograms are normalized to their number of entries. The peak in the blue histogram on the right originates from electrons. They have been selected by setting the gas pressure[2] to 20 psia and only accepting events with a signal in the outer Čerenkov photomultiplier. The entries in the green histogram is the energy deposited by 10 GeV pions which was recorded at a gas pressure of 5.7 psia and with the requirement of a signal from the inner Čerenkov photomultiplier in the trigger decision. The energy from protons is shown on the left in red. The proton run was acquired with the gas pressure set to 20 psia and rejecting all events that produce any signal in the inner or the outer Čerenkov photomultiplier tubes.

---

[2]psia is the unit used for the gas system at FTBF and stands for pounds-force per square inch absolute, i.e. gauge pressure plus local atmospheric pressure

The ongoing analysis of the data measured at Fermilab shows that the pion content in events recorded in a run with mixed beam at $10\,\mathrm{GeV}$ was successfully increased from $\sim 50\,\%$ without using the Čerenkov to $\sim 90\%$ requiring a pion signature in the trigger [45].

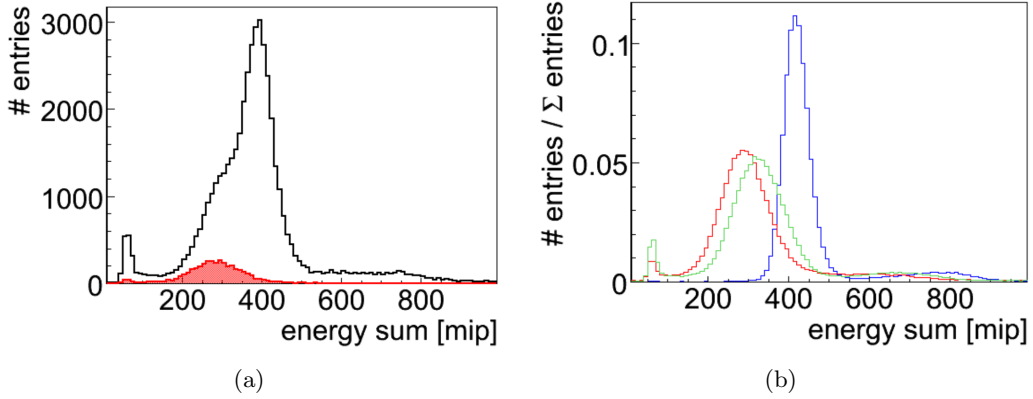(a)   (b)

Figure 5.9.: Distribution of the energy deposited in the AHCAL measured with a $10\,\mathrm{GeV}$ mixed beam at FTBF: (a) Positive $10\,\mathrm{GeV}$ particles (open histogram) without the Čerenkov information in the trigger decision. Protons have been selected using the Čerenkov information in the offline analysis (overlaid filled histogram). (b) Three different runs acquired using the Čerenkov signature in the trigger decision to select electrons (blue), pions (green) and protons (red). The small peak on the very left in (a) and (b) originates from muons in the beam. Plots taken from [45].

The Drift Chambers

The three wire chambers on the very left in figure 5.5 are part of the test beam equipment at FTBF and have not been integrated into the read out chain. They were used as monitors for the beam position and spread during the data acquisition.

During the FNAL test beam program, four drift chambers (DC1−DC4) have been used to record the beam position which where already applied in the data acquisition of both the Si-W ECAL [46] and ScECAL [47] with electron beams at DESY. At the FTBF, the drift chambers were operated with a gas mixture of $50\,\%$ argon and $50\,\%$ ethane.

Collected Data

The aim of the test beam program in 2008 and 2009 at the FTBF was the acquisition of low-energy pion data. Since at low energies most of the pions start to shower

already in the ECAL, it was removed for dedicated AHCAL only data acquisition runs. Figure 5.10 shows the energy deposited by pions in the energy range $1-20\,\mathrm{GeV}$ in the AHCAL without an ECAL in front from an ongoing study on the Fermilab data [45]. These data will be used to investigate the linearity of the AHCAL and to study the performance of Monte Carlo simulations at low energies.
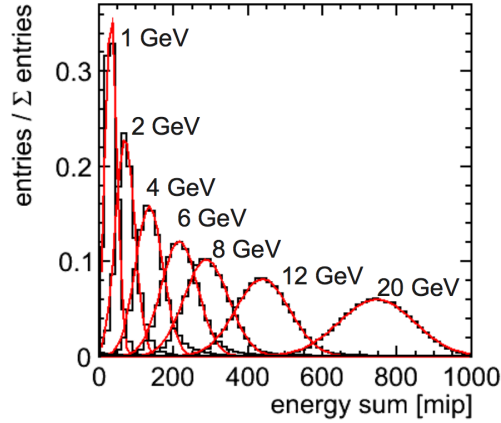

Figure 5.10.: Deposited energy in the AHCAL by pions in the energy range $1-20\,\mathrm{GeV}$ acquired during the Fermilab test beam program in a dedicated configuration without an ECAL in front [45].

Measurement of the Beam Composition

Figure 5.11 shows the beam composition measured during the data acquisition in the combined CALICE setup with the ScECAL in September 2008 [48] using preliminary detector calibrations. Only the T10×10A and T10×10B counter and no information from the Čerenkov detector have been used in the trigger decision. The plot shows the relative number of events as a function of the beam energies categorized into four types:

- Muons are identified by a low energy deposition in the ScECAL and the AHCAL.
- Electrons deposit a large amount of energy in the ScECAL and only noise signals in the AHCAL.
- Two-Particles events are events with an energy deposition in the detectors which is too high for one particle at the given beam energy.
- Pions are identified in events in which no electrons, no muon and no two-particle signature is found.

One can see that at energies above $12\,\mathrm{GeV}$ pions dominate in the mixed beam while at lower energies below most of the particles in the beam are electrons. At lower energies the muon contents increases. The largest fraction of double particle

events of 15 % is observed at 3 GeV. The analysis of the beam composition is an early study done during the ongoing data acquisition without a serious estimation of the uncertainty. Especially at energies below 3 GeV it is very hard to distinguish muons and pions. Nevertheless, this rough estimate of beam composition shows the capabilities of the interplay between the AHCAL and the ScECAL which has been integrated into the combined readout in the framework of this thesis.
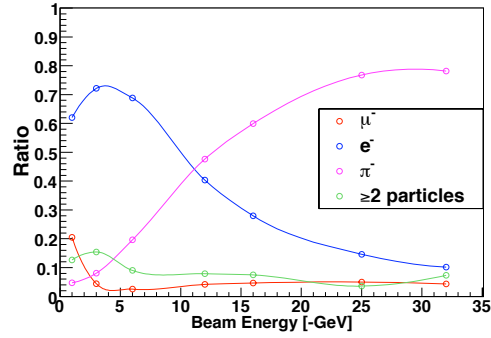

Figure 5.11.: Composition of the beam at MT6 measured with the CALICE calorimeters in 2008. Picture taken from [44].

6. Calibration

The AHCAL is a device built to measure the energy of subatomic particles in the range of several GeV. In contrast, the signals produced in the single calorimeter cells are in the order of some pC. The purpose of the calibration is to establish a relation between the cell signals and the energy of the particle to be measured. For an ideal calorimeter the relation between the particle energy and the obtained signal is linear and independent of the particle type over its full measuring range. Real calorimeters suffer from imperfect readout mechanisms and a response dependent on the physics taking place at different energies for several particle species.

It is a non-trivial task to calibrate a multi-million channel calorimeter as planned for the ILC. The calibration of the 7608 channel AHCAL is already challenging. It is necessary to establish a calibration procedure that compensates detector effects such as non-linearities and production tolerances as much as possible in the aimed energy range. Section 6.1 introduces the calibration procedure developed for the AHCAL. The calibration constants obtained during the test beam periods are presented in 6.2. The response of the Silicon Photomultipliers used for the AHCAL signal readout is temperature dependent. Fluctuations in the ambient temperature during data acquisition and calibration thus have to be corrected for. In section 6.3 the temperature correction established in the framework of this thesis is described. The temperature correction is validated in section 6.4.

6.1. The AHCAL Calibration Chain

The AHCAL calibration chain relates the energy E of the incident particles in GeV to the sum of the visible energy E_i in the single calorimeter cells:

$$E \text{ [GeV]} = \sum_i E_i \text{ [MIP]} \cdot \frac{1}{w} \text{ [GeV/MIP]} \qquad (6.1)$$

The common scaling factor w is obtained using particle showers from the test beam data taking. The visible energy E_i for cell i in units of minimum ionizing particles (MIP) is derived from the raw cell signal A_i measured in ADC channels, which has to be pedestal subtracted, equalized and corrected for non-linearity:

$$E_i \text{ [MIP]} = \frac{A_i \text{ [ADC]} - P_i \text{ [ADC]}}{M_i \text{ [ADC]}} \cdot f^{-1} \left(A_i \text{ [pix]} \right). \qquad (6.2)$$

The pedestal P_i, the equalization constant M_i and the saturation correction f^{-1} (relying on the number of SiPM pixels fired) are determined for each single cell which is explained in the following.

Pedestal Subtraction

Even if no SiPM pixel is firing, the signal read out with the ASIC always fluctuates around a non-zero level. This noise signal is also called pedestal level and is measured frequently during the data acquisition in randomly triggered events without LED light. The left peak in figure 6.1 shows a typical noise distribution in a single calorimeter cell. In the following the mean value of the noise distribution for a single channel is referred to as pedestal P_i. To account for shifts of the noise level, the pedestal is subtracted from the single cell signals for each beam event.

Cell Equalization

To equalize the calorimeter cells, it is necessary to measure their response to a standard signal. The energy deposition by a particle in a physics process constant over a large energy range can be used for this purpose. For the calibration, muons traversing the AHCAL are used as approximation for minimum ionizing particles. The calorimeter is exposed to a broad beam of muons in dedicated calibration runs. Figure 6.1 shows a typical spectrum of muon signals in a single calorimeter cell in units of ADC counts. The convolution of a Gaussian distribution with a Landau distribution is fitted to the muon signal on the right. The most probable value of this distribution is obtained for each single calorimeter cell and referred to as MIP calibration constant M_i.
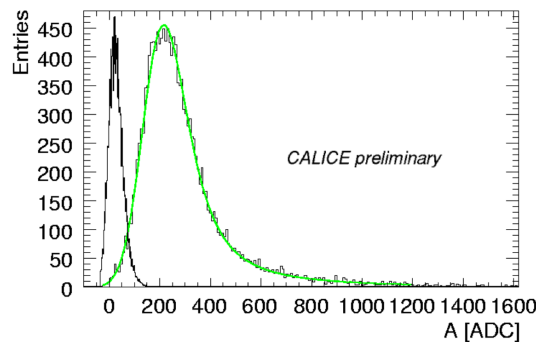

Figure 6.1.: Typical response of a single calorimeter cell to muons (right peak) [49]. The left peak shows the pedestal determined in a separate measurement for the same channel.

Non-linearity Correction

The response of a SiPM is shown in figure 6.2(a). The observed non-linear behaviour is due to the limited number of SiPM pixels and the finite pixel recovery time.

For N_γ photons arriving at the surface of a SiPM with a total number of pixels N_{tot} the average number of pixels fired can be approximated by

$$N_{pix} = N_{tot} \cdot \left(1 - e^{-N_\gamma/N_{tot}}\right).$$ (6.3)

For real SiPMs with possible dead pixels or the surface only partially illuminated, the total number of pixels N_{tot} has to be replaced by the average effective number of pixels N_{eff}. The effective number of pixels N_{eff} does not necessarily have to be smaller than N_{tot}. Pixels with a small recovery time can fire more than once during the signal sampling time, which can lead to an increase of the average effective number of pixels. A real SiPM gives a signal proportional to N_γ, but is attenuated by the factor

$$f\left(N_{pix}\right) = \frac{N_{pix}}{N_\gamma} = \frac{N_{eff}}{N_\gamma} \cdot \left(1 - e^{-N_\gamma/N_{eff}}\right).$$ (6.4)

The response curve of every bare AHCAL SiPM has been measured before the integration into a scintillator tile [32].

Solving equation 6.3 for N_γ and replacing N_{tot} by N_{eff} results in

$$N_\gamma = -N_{eff} \cdot \log\left(1 - \frac{N_{pix}}{N_{eff}}\right).$$ (6.5)

This way a function to correct for the saturation behaviour can be constructed:

$$f^{-1}\left(N_{pix}\right) = \frac{N_\gamma}{N_{pix}} = -\frac{N_{eff}}{N_{pix}} \cdot \log\left(1 - \frac{N_{pix}}{N_{eff}}\right).$$ (6.6)

In the AHCAL reconstruction chain, the signal of every SiPM is corrected for the saturation behaviour by multiplication with an individual correction function $f^{-1}\left(N_{pix}\right)$. An example for a correction function is shown in figure 6.2(b).

Gain Determination

To correct for the saturation behaviour, it is necessary to determine the number of pixels fired from the SiPM signal. Since the pixels are are connected in parallel, the measured SiPM response is the sum of the single pixel signals. In the calibration mode of the AHCAL readout ASIC it is possible to resolve SiPM signal spectra with a high resolution. Figure 6.3 shows the spectrum of a single channel illuminated with very low light intensities by the CMB. The peaks for different numbers of pixel firing at a time can be clearly distinguished. The first peak on the very left is the pedestal peak with no pixel firing. The peak next to it is from one pixel firing at a
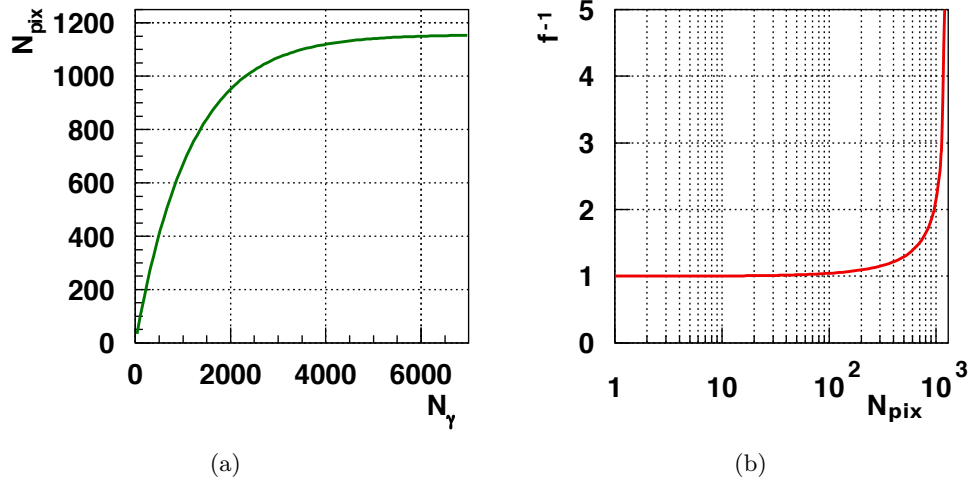
(a)　　　　　　　　　　(b)

Figure 6.2.: (a) Saturation curve of an (ideal) Silicon Photomultiplier. (b) Inverted
saturation function $f^{-1}(N_{\mathrm{pix}})$ used for correction. Plots are from [50].

time. The third pixel from the left is from two pixels firing at a time and so on. The
distance between the peaks is extracted by fitting a multi-Gaussian to the spectrum.
The exact fitting procedure is described in detail in [37]. In the following the peak
distance for a single calorimeter cell in units of ADC channels will be referred to as
gain G_i.

The number of pixels fired A_i [pix] is calculated from the SiPM signal A_i [ADC]:

$$A_i \text{ [pix]} = \frac{A_i \text{ [ADC]} - P_i \text{ [ADC]}}{G_i \text{ [ADC]}} \cdot I_i \qquad (6.7)$$

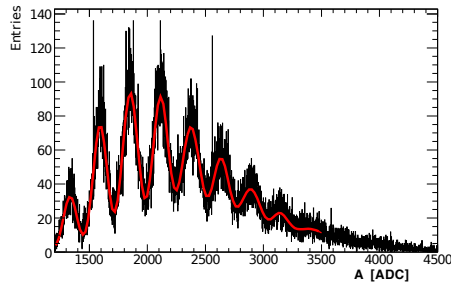The inter-calibration factor I_i is described in the following.

Figure 6.3.: Single pixel spectrum of a single calorimeter cell obtained in a special
LED run [37]. A multi Gaussian is fitted to determine the SiPM gain.

Inter-Calibration

For the gain calibration the AHCAL readout ASICs are operated in a special calibration mode with a higher amplification and shorter shaping time compared to the physics mode used for the test beam data acquisition. Therefore it is necessary to apply the inter-calibration factor I_i in equation 6.7.

Ideally, the inter-calibration factor should be a constant factor between the two readout modes of the ASIC, but it turns out to depend on the different types of SiPMs built into the AHCAL. The different signal shapes of the single SiPMs in combination with the two different shaping times in calibration and physics mode result in channel dependent inter-calibration factors I_i.

The factor I_i is measured for each single channel using the LED system. For both modes the same light intensity is injected into the scintillator tiles. This is done for several light intensities in the linear range of the readout system. The ratio between the slopes of the linear responses in calibration and in physics mode is the inter-calibration factor I_i.

Light Yield

The light yield of one AHCAL cell is defined as its response to a MIP in units of pixels fired:

$$LY_i \ [\text{pix/MIP}] = \frac{M_i \ [\text{ADC}]}{G_i \ [\text{ADC}]} \cdot I_i. \tag{6.8}$$

It is necessary to apply the inter-calibration constant I_i, since the MIP and gain calibration factors are obtained in different modes of the readout ASIC. The design goal is 15 pixels per MIP, compromising between the size of the available dynamical range and a reasonable signal-to-noise ratio.

6.2. Test Beam Calibration

This section gives an overview of the calibrations acquired during the test beam data taking at CERN and FNAL.

Gain and Inter-Calibration

During the test beam data acquisition special LED calibration runs for the gain and inter-calibration are performed about every eight hours. The acquisition of the LED runs takes about one hour. The gain and inter-calibration constants have been obtained according to the procedures described in section 6.1.

Figure 6.4(a) shows the distribution of all SiPM gain calibration constants G_i obtained during the CERN 2007 test beam. The uncertainty of the gain determination

is about 2% for a single channel [50]. The spread (RMS) of 24% in the gain distribution is due to production variations in the AHCAL SiPM sample. Therefore it is necessary to apply individual gain constants for each single channel. The gain constants averaged per AHCAL layer are shown in figure 6.4(b). The error bars indicate the spread of the single cells per module.
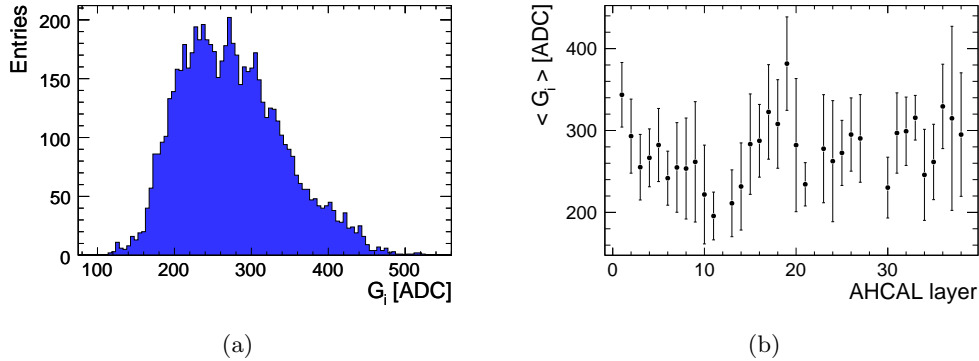

(a)   (b)

Figure 6.4.: (a) Distribution of the gain calibration constants for all AHCAL channels. (b) Average gain calibration constant per layer.

The distribution of the inter-calibration constants acquired during the CERN 2007 data taking is shown in figure 6.5(a). The uncertainty on the inter-calibration coefficient for a single calorimeter channel is better than 1% [50]. While the majority of the inter-calibration constants is around 11.5 ± 0.6, there are groups of channels with lower values. As mentioned in section 6.1, the reason for this are different signal shapes for part of the SiPMs in combination with the different timing in the calibration and the physics mode of the readout ASIC. Figure 6.5 shows the inter-calibration values averaged per AHCAL module as a function of the layer number with the RMS of the distribution as error bars.

The gain and inter-calibration efficiency is defined as the number of channels for which the respective calibration can be obtained successfully divided by the total number of working channels. About 2% of the channels are considered inactive due to initially bad soldered SiPMs or subsequently broken connections. The inactive channels together with the few channels connected to a broken LED (0.11%) are excluded in the efficiency calculation. During the 2007 test beam period at CERN the LED system of the AHCAL layers 12, 22, 28 and 29 did not work properly - they are missing in figures 6.4 and 6.5. No reliable gain and inter-calibration could be obtained at that time. In the efficiency calculation for CERN the layers are therefore excluded. They could be recovered after the data acquisition in the laboratory at DESY (described in section 6.5) and are included in the efficiency calculation for the FNAL test beam period.

The efficiency of the extraction of the gain (a) and inter-calibration (b) constants
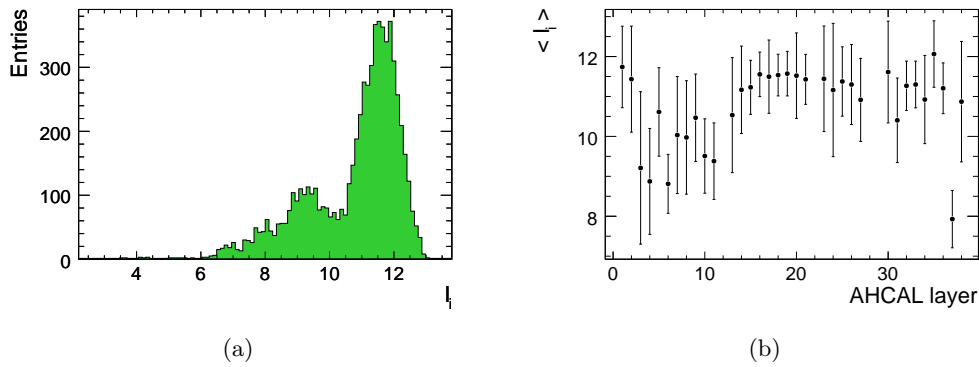
(a) (b)

Figure 6.5.: (a) Distribution of the inter-calibration constants for all AHCAL channels. (b) Average inter-calibration constant per layer.

is shown in figure 6.6 for the test beam periods at CERN (filled circles) and FNAL (open triangles). After initial problems during the system commissioning in 2007 at CERN could be solved, a gain calibration efficiency of about 95% has been achieved. After the transportation to the FNAL test beam site the gain efficiency remained stable throughout the data taking there. The problems during the CERN commission are also visible in the inter-calibration efficiency. At FNAL the system worked much more reliable and a high inter-calibration efficiency was achieved. In total an efficiency of more than 99% is reached combining several runs for both, the gain and inter-calibration constants.
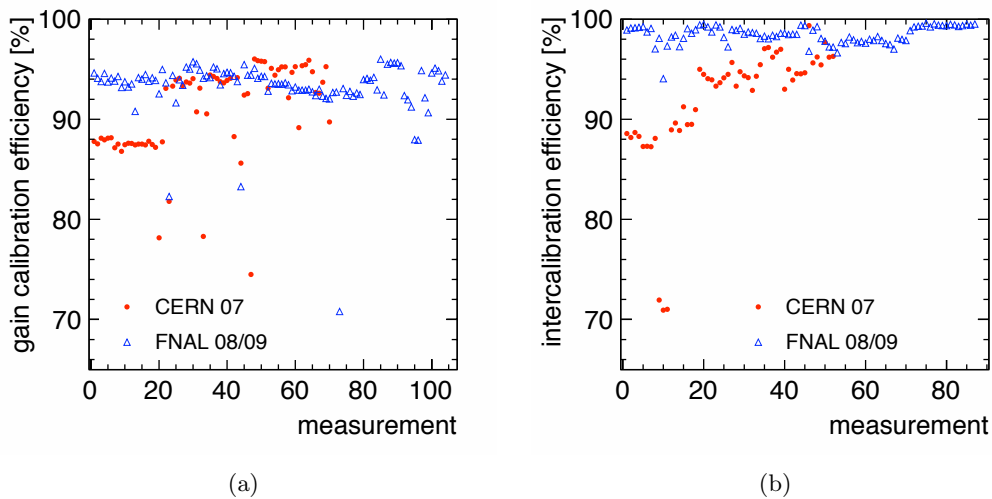

(a) (b)

Figure 6.6.: Gain (a) and inter-calibration (b) efficiency for the data taking periods at CERN and FNAL. The plots are from [50].

MIP Calibration

To obtain the constants M_i needed for the cell equalization, the AHCAL is exposed to muon beams with a broad distribution over its entire surface. The muons are assumed to generate MIP-equivalent responses in the single calorimeter cells. A minimum of 1500 events per cell are needed to obtain a stable fit to the most probable value of the Landau distributed muon spectrum. A full MIP calibration of the whole detector takes about 12 hours, since the data acquisition rate is limited to 100 Hz by the readout electronics and the beam is not uniformly distributed over the AHCAL surface. The muons are selected by detecting their tracks left in the AHCAL. The exact selection criteria and the fitting procedure applied are described in [51]. The uncertainty on the most probable value obtained from the fits is below 2% for each AHCAL channel.

Figure 6.7(a) shows the distribution of the equalization constants M_i for all channels of the AHCAL with a mean value of $< M_i > = 352\,[\mathrm{ADC}]$. The relative large spread (RMS) of approximately 34% around the mean value is due to the combination of production variations in the SiPM sample (already visible in the gain measurements above) and differences in the tile uniformity and the light coupling. Figure 6.7(b) shows the MIP constants M_i averaged per AHCAL layer. The error bars show the spread of the single cell constants within one layer.
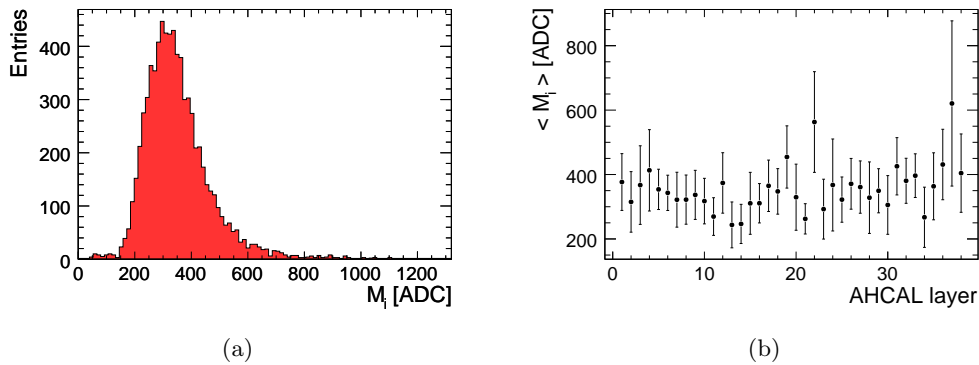

(a)   (b)

Figure 6.7.: (a) Distribution of the MIP calibration constants for all AHCAL chan-
nels. (b) MIP calibration constants averaged over single AHCAL layers.

To calculate the MIP detection efficiency, muon tracks strictly perpendicular to the AHCAL front face have been selected. For each cell the detection efficiency is defined as the number of times the cell response is above the 0.5 MIP noise threshold divided by the number of times it was passed by a muon. Figure 6.8 shows the MIP detection efficiency averaged over all cells per AHCAL module. The errors bars indicate the spread (RMS) over all cells in one module. For the 2007 CERN test beam period the average MIP detection efficiency is 93% (circles). During the FNAL test beam period (triangles), an efficiency of 94 % is observed.
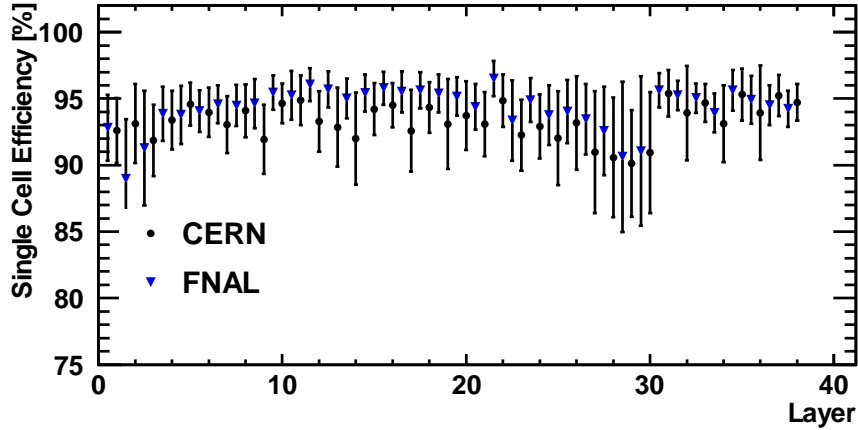
Figure 6.8.: The MIP detection efficiency during the test beam at CERN (circles) and at FNAL (triangles) as a function of the layer number [51].

Saturation correction

The saturation behaviour for all SiPMs has been measured on a test bench before the integration the AHCAL [32]. The full surface of the sensor was illuminated. In the tiles built into the AHCAL however, the light is guided via a wavelength-shifting fibre to the SiPMs. The aperture of the fibre is circular, while the SiPM sensitive surface is quadratic. Only part of the SiPM pixels are illuminated consequently which leads to a decrease of the effective number of pixels.

Therefore, the saturation measurements have been repeated in the commissioned AHCAL. Figure 6.9(b) shows the distribution of the ratio between the effective pixel number for the mounted N_{eff}(mounted) and the bare SiPMs N_{eff}(bare). The mean value of 0.8 is consistent with the ratio $\pi r^2/4r^2 = \pi/4 \approx 0.8$ between the area of a circle with radius r and a square with side length $2r$. The tail to smaller values can be attributed to misplaced wavelength-shifting fibres relative to the SiPM surface (cf. figure 6.9(a)). The effective number of pixels could be determined for only 73% of all AHCAL SiPMs with an uncertainty of less than 3% [50, 32]. For this reason the curves measured for the bare SiPMs are corrected with the average of 0.8 in stead of using individual factors in the calibration chain.

6.3. Temperature Correction Procedure

The gain and the photon detection efficiency of the SiPM both depend on the applied over voltage $\Delta V = V_{bias} - V_{bd}$. The breakdown temperature dependent voltage $V_{bd}(T)$ is a semiconductor property. This results in a temperature dependent gain and response, typically in the order of a few percent. Therefore, a set of calibration constants is only valid for the temperature at which it has been obtained.

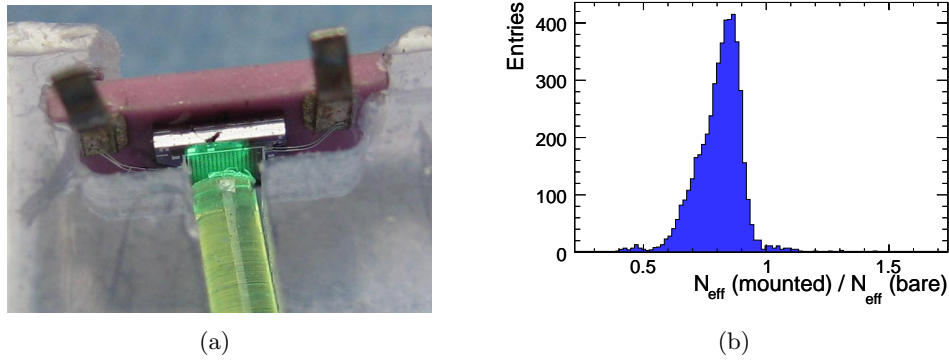(a)   (b)

Figure 6.9.: (a) The photo shows a misplaced wavelength-shifting fibre guiding light
to a SiPM mounted in an AHCAL scintillator tile. Picture taken by M.
Reinecke. (b) Ratio between the total number of effective SiPM pixels
obtained from measurements with the SiPM mounted in the AHCAL
and from test bench measurements before the mounting.

The work on the correction of the temperature correction was done in close coop-
eration of several people and part of it is also documented in two diploma theses
[32, 71] and two papers [52, 53].

In figure 6.10(a) the average temperature per AHCAL layer during the MIP cali-
bration (squares) and the acquisition of positron data (triangles) are shown. One
can clearly see an offset of $\approx 2.5\,°\mathrm{C}$ in each layer between the temperature during
the calibration and the positron run. In addition, the shapes of the profiles differ
slightly. The average temperature measured inside the calorimeter during the CERN
2007 data taking is displayed in figure 6.10(b). Day-night shifts in the temperature
of roughly $0.5\,°\mathrm{C}$ are visible. Over the full data acquisition period temperature vari-
ations of up to to $3\,°\mathrm{C}$ inside the AHCAL were observed, which corresponds to a
change of $\sim 10\,\%$ in the response of the SiPMs.

Even though the gain constants are obtained roughly every eight hours, a high gain
calibration efficiency is only achieved by combining several runs acquired at different
temperatures as mentioned before in section 6.2. Furthermore, the missing LED
calibrations for four AHCAL layers mentioned in section 6.2 have been recovered
months later in a laboratory setup with completely different ambient conditions.

The final calorimeters that will be operated at a collider like the ILC will have to
be calibrated before their installation at the experimental site. Due to the large
number of channels planned for the particle flow detectors, a test beam calibration
of each individual calorimeter cell is hardly possible. For the large detectors, not
only temperature variations but also changes of the bias voltage V_{bias} due to ageing
effects in the power supplies might occur.

To be able to apply calibration coefficients to data obtained at a different time and

under other ambient conditions, it is necessary to correct for temperature effects. The temperature dependencies of the gain and response of the AHCAL SiPMs have been determined and are stored in a calibration data base. In the framework of this thesis a method to transport the MIP and gain calibrations to any temperature has been developed and implemented in software.
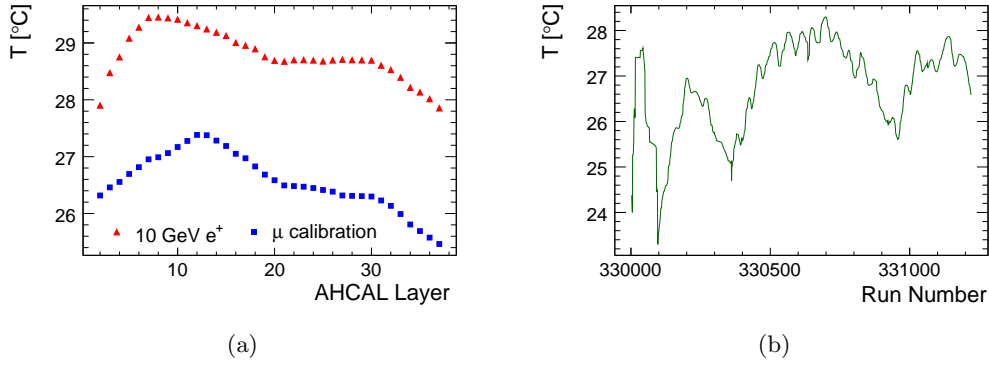

(a)

(b)

Figure 6.10.: (a) Temperature as a function of the AHCAL layer number during a muon calibration run and during the acquisition of positron data. (b) Average AHCAL temperature throughout the data taking at CERN in 2007.

Temperature Measurement

The temperature inside the AHCAL prototype is monitored using five temperature sensors built into the modules. They are shown as red filled circles in figure 4.1. For the time being, the temperature of the sensor closest to a cell inside an AHCAL layer is used. This introduces an additional uncertainty on the temperature measurement depending on the distance to the sensor used. In the future more sophisticated extrapolations of the temperature might be considered.

Gain Temperature Dependence

For each channel of the AHCAL the gain was determined at different temperatures according to the procedure described in chapter 6.1. The gain for a single calorimeter channel as a function of temperature is shown in figure 6.11(a). A linear gain temperature dependence is observed. The function $G(T) = \frac{dG}{dT} \cdot (T - T_0) + G_0$ is fitted to the data. In order to get reliable fit results, only channels with gain data at temperatures varying in a range of at least $2\,°\mathrm{C}$ are taken into account. The fit is regarded as successful if the ratio between the χ^2 and the degrees of freedom (DOF) is $\chi^2/\mathrm{DOF} < 20$. These requirements were fulfilled for 90% of all channels [32]. The
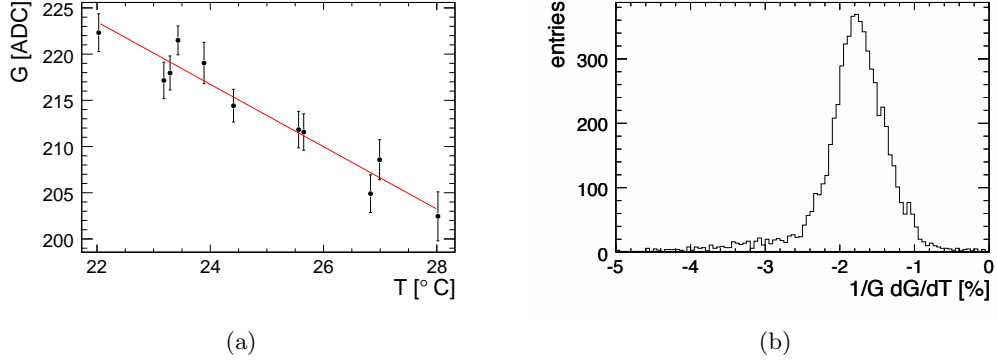
Figure 6.11.: (a) Gain temperature dependence for a single AHCAL SiPM.
(b) Distribution of the relative gain temperature dependence $\frac{1}{G_0}\frac{dG}{dT}$ for all AHCAL channels.

distribution of the relative slopes $\frac{1}{G_0}\frac{dG}{dT}$ is shown in figure 6.11(b) for $G_0 = G(27°\text{C})$. It has a mean of $-1.7\,\%\,\text{K}^{-1}$ and a spread of $0.3\,\%\,\text{K}^{-1}$.

MIP Temperature Dependence

The temperature dependence of the response to muons is obtained from the MIP calibration constants M_i determined at different temperatures for each SiPM. Figure 6.12(a) shows the change of the SiPM response for a single AHCAL channel. The SiPM response is proportional to the gain and the photon detection efficiency. For this reason, the temperature dependence of the response to muons is expected to be quadratically. However in the temperature range investigated, a linear dependence is a good approximation. As for the gain, a first order polynomial $M(T) = \frac{dM}{dT}\cdot(T - T_0) + M_0$ is fitted to the data. The distribution of the relative response temperature dependence with a mean value of -3.7% K^{-1} is plotted in figure 6.12(b). The spread is 1.1% K^{-1}. The MIP temperature dependency was measured successfully for 93% of all AHCAL channels [54].

Application

For each AHCAL channel the parameters $(G_0, T_0^G, \frac{dG}{dT})$ and $(M_0, T_0^M, \frac{dM}{dT})$ are stored in a condition database. With this information it is possible to transport the calibration constants obtained at a temperature T_0 to any other temperature T:

$$G(T) = \frac{dG}{dT}\cdot(T - T_0^G) + G_0 \tag{6.9}$$

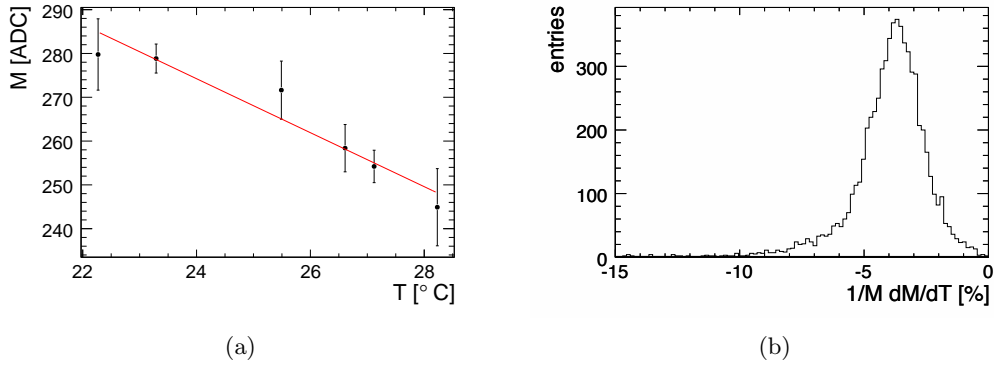$$M(T) = \frac{dM}{dT}\cdot(T - T_0^M) + M_0 \tag{6.10}$$

(a) (b)

Figure 6.12.: (a) Temperature dependence of the response to muons for a single AHCAL SiPM. (b) Distribution of the relative temperature dependence $\frac{1}{M_0}\frac{dM}{dT}$ of the SiPM response to muons for all AHCAL channels.

For the MIP constants this is only correct as long as the linear approximation is valid. Figure 6.13 shows the relative difference of two separate measurements at different temperatures of the gain (a) and the MIP coefficients (b) before transportation to the same temperature (open histograms) and after transportation (filled histograms). The mean value of the distributions in both cases is in the order of $7 - 10\,\%$ percent before the transportation. The temperature transportation minimizes the mean relative differences while there is no significant influence on width of the distributions.
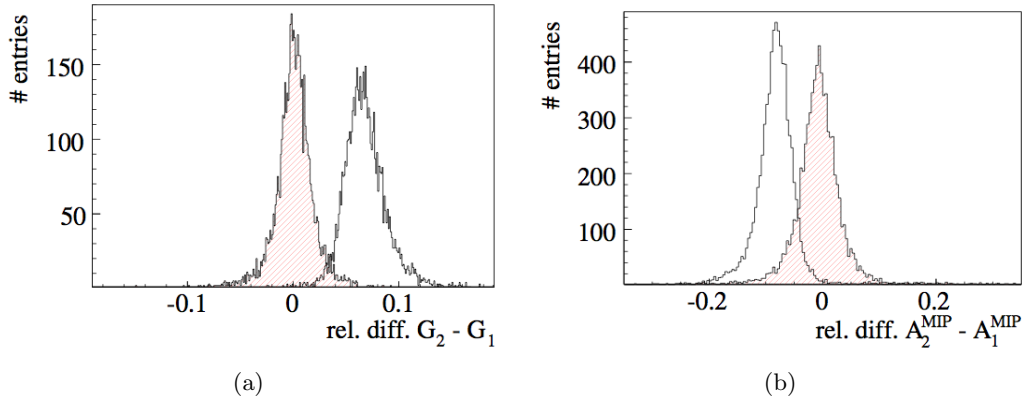

(a) (b)

Figure 6.13.: Relative difference between two measurements of the gain (a) and the MIP coefficients (b) at different temperatures with (filled histogram) and without (open histogram) temperature correction. Plots taken from [32].

The temperature correction is used in the reconstruction of the data to account

for the temperature differences between the calibration and data acquisition runs. In the calibration for each event in a data run, the calibration constants G_0 and M_0 for the single channels are transferred to the temperature T of the calorimeter cell during the data acquisition. The transferred constants are then used in the calibration chain explained in section 6.1.

6.4. Validation of the Temperature Correction

A set of positron runs has been selected to prove the correction for the temperature dependence of the AHCAL response implemented in the framework of this thesis. They have been recorded at beam energies ranging from 10 to 50 GeV without the ECAL in front of the AHCAL at CERN in 2007. The electromagnetic response of the AHCAL is studied in [50] with a similar data set and the temperature correction applied. The purpose of this analysis is to cross-check temperature correction procedure and to investigate the effect of applying individual correction factors for single channels. The data presented here have been reconstructed using the same event selection and calibration factors as in [50]. Also, the same systematic uncertainty as described in this paper is assumed.

Three different calibration scenarios have been compared:

- no temperature correction at all,
- average correction: using the mean values of the distributions of the relative temperature dependence slopes for the gain calibration $\frac{1}{G}\frac{dG}{dT} = -1.7\,\%\,K^{-1}$ and the MIP calibration $\frac{1}{M}\frac{dM}{dT} = -3.7\,\%\,K^{-1}$,
- single cell correction: using the measured temperature dependencies for each individual calorimeter cell.

Figure 6.14 shows the energy sum spectra for the chosen runs. For the histograms in the upper half the reconstruction was performed with the average temperature correction, for the lower half the reconstruction was done without temperature correction. Considerable differences between the peak positions of the reconstructed energy sum with and without temperature correction at the same beam energy are visible.

A Gaussian distribution was fitted to the energy spectra. Figure 6.15(a) shows the fitted mean values E_{rec} as a function of the beam energy E_{beam} for Monte Carlo simulation compared to data with and without temperature correction. One can see that only after temperature correction the energy scale between Monte Carlo and data matches within the systematic uncertainty. The function $E_{\mathrm{rec}} = E_{\mathrm{beam}}/w$ has been fitted to the data points. The results for the energy scale factor for Monte Carlo $w_{\mathrm{MC}} = (41.9 \pm 0.5)$ MIP / GeV and for data with average temperature correction $w_{\mathrm{avg}} = (42.9 \pm 0.5)$ MIP / GeV are in good agreement, while the scale factor for data without temperature correction $w_{\mathrm{ntc}} = (38.3 \pm 0.5)$ MIP / GeV differs.

The residuals to linearity are shown in figure 6.15(b). The plot suggests a non

non-zero offset for the simulations at zero beam energy. This offset is the combined result of the 0.5 MIP threshold and detector noise. The linearity is not influenced by the temperature correction. The deviation from linearity in data hints at problems with the saturation correction. The response of the AHCAL to positrons and the non-linearity is discussed further in [50].

The temperature correction using the averages and individual values from the distribution of the temperature dependencies shown in figures 6.11(b) and 6.12(b) is compared in figure 6.16. No significant difference in the energy scale (a) and the residuals to linearity (b) is visible. Therefore it is sufficient to use the simpler method of using the average temperature dependencies for the gain and the MIP calibration in the correction procedure.

The resolution of the reconstructed energy is defined as the ratio $\sigma_{\rm rec}/E_{\rm rec}$ between the width and the mean value of the Gaussian distribution fitted to the energy spectra. The influence of the temperature correction on the energy resolution is shown in figure 6.17. There is no considerable impact of the temperature correction on the energy resolution visible. The reason for this is that the variation of the temperature between the single AHCAL layers is rather small compared to the overall temperature difference between calibration and positron data acquisition.

6.5. Recovery of the Missing LED Calibration

As already mentioned in this chapter, the four layers 12, 22, 28 and 29 of the AHCAL could not be calibrated due to problems with the LED system during the test beam data taking at CERN in 2007. While the cell readout itself for these layers was not affected and data including muon runs for the MIP calibration could be recorded, the gain and inter-calibration were missing. The four layers correspond to roughly 11% of the total AHCAL channels. In the following the recovery of the missing calibration is described.

After the detector moved back to DESY, several LEDs as well as one LVDS[1] driver chip in an electronics board had to be replaced. All LEDs for the modules of the affected AHCAL layers had to be manually retuned to be able to measure the single pixel SiPM spectra. The setup built to operate the modules in the laboratory is shown in figure 6.18. The modules sit on a wooden support structure. The LED system is attached on the left and the very front-end electronics on the right. The blue rack in the background houses the power supply and the VME readout system.

The LED system of the AHCAL layer 20 was working without problems during the test beam period. The module for this layer was setup in addition in the laboratory to allow for a comparison with the calibration values obtained at CERN. Figure 6.19(a) shows the gain values for all channels of layer 20 from two measurements. One was obtained during the CERN test beam period (black) and the other one was

---

[1]LVDS - Low Voltage Differential Signal

measured afterwards in the laboratory at DESY (red). The constant shift between the two set of gain values is due to the different ambient temperatures during the measurements. Using the temperature correction, the DESY gain values could be transported to the CERN temperatures. The histogram in figure 6.19(b) shows the relative difference between the two measurements with and without temperature correction. Before the correction the mean value of the distribution was $11.5\,\%$ with an RMS of $2.1\,\%$. After the correction the mean value is $0.2\,\%$ and the RMS has a slightly larger value of $2.8\,\%$ due to uncertainty in the determination of dG/dT. This shows that calibration constants obtained in another setup at a different ambient temperature can be transported to the conditions during the test beam data taking several months before using the technique developed in this work.

After the repair and adjustment of the LED system of the modules 12, 22, 28, and 29, the missing calibrations have been determined in the laboratory setup. The SiPM gain constants, their temperature dependency and the inter-calibration coefficients have been measured. Figure 6.20(a) shows the gain constant for the recovered AHCAL layers (red) and the full gain calibration set (blue). Figure 6.20(b) shows the light yield calculated using the gain, the MIP and inter-calibration factor (cf. equation 6.8) for the recovered layers (red) and all AHCAL channels (blue). All gain values used in figure 6.5 have been transported to the average temperature of $T = 27\,^{\circ}\mathrm{C}$.

The recovered calibration values are stored together with the temperature at which they have been obtained in the conditions database. The developed temperature correction procedure transports the calibration factors to the temperature of the data they are applied to. This way data recorded with the problematic layers during the CERN test beam 2007 can be used in the official reconstruction.
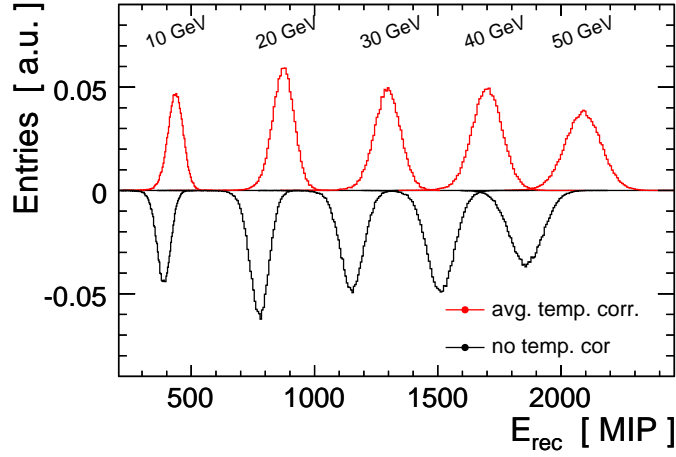
Figure 6.14.: Energy sum spectra for the seven runs chosen for the validation. The upper half shows the reconstruction with the average temperature correction, the lower half the reconstruction without.
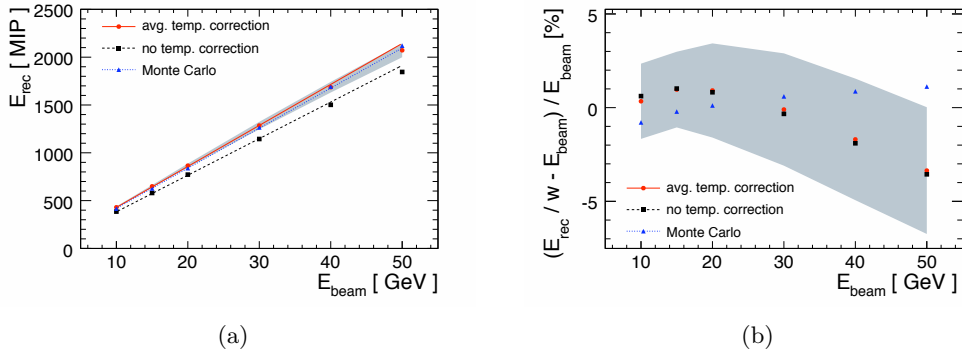

Figure 6.15.: Comparison of the energy scale (a) and the residuals to linearity (b) between simulation and data with and without temperature correction of the calibration constants. The grey band indicates the systematic uncertainty.
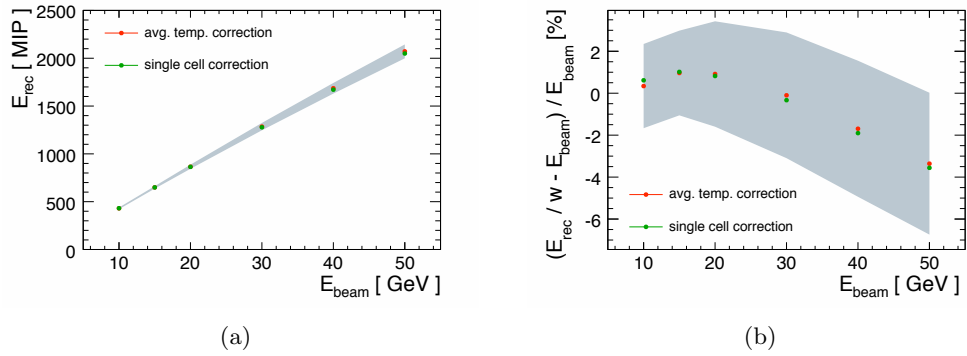
(a)   (b)

Figure 6.16.: Comparison of the energy scale (a) and the residuals to linearity (b) between data with temperature correction using averages and individual values from the distribution of the temperature dependencies. The grey band indicates the systematic uncertainty.
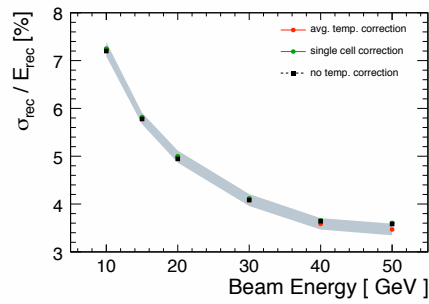

Figure 6.17.: Comparison of the energy resolution for data between the different temperature correction scenarios. The grey band indicates the systematic uncertainty.

Figure 6.18.: Operation of single AHCAL modules in the laboratory at DESY to recover missing LED calibrations.
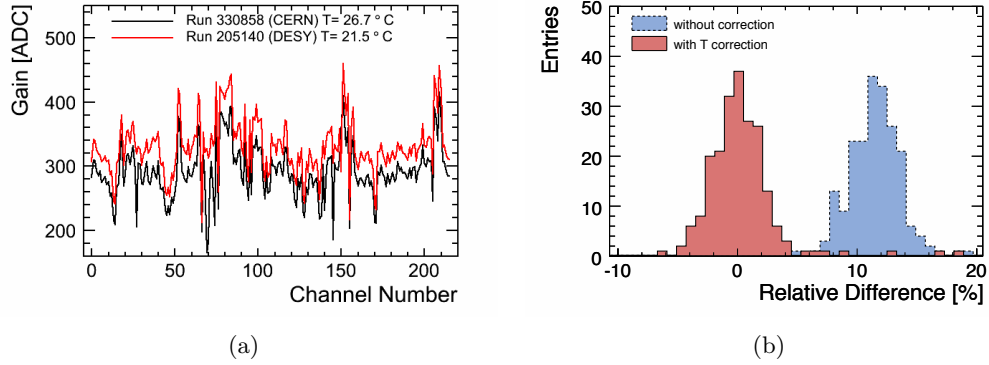
(a)

(b)

Figure 6.19.: (a) Gain for all channels in layer 20 determined during the CERN test beam period (black) and afterwards in the laboratory at DESY (red). (b) Relative difference between the two measurements.
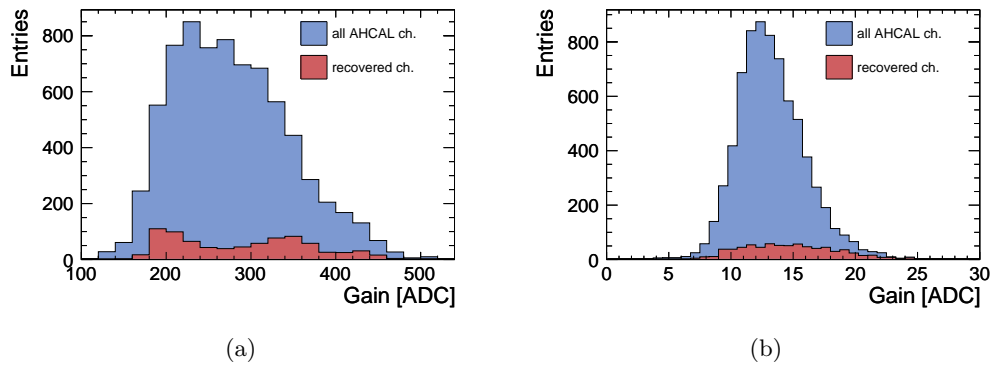

(a)

(b)

Figure 6.20.: Gain constants (a) and the light yield (b) for the recovered layers in red and for the full AHCAL in blue.

71

6. Calibration

7. Monte Carlo Simulation

Simulations are very important for the design of detectors and the data analysis in high energy physics. In particular, realistic predictions of the longitudinal and lateral extension of particle showers in the detectors are necessary to be able to choose the detector sizes, the absorber materials and the technologies to be used for the readout. The ILD concept is based on the Particle Flow Approach. The performance of this sophisticated interplay between software algorithms and high resolution detectors is determined by the correct identification of particle showers. Misidentification of particle showers due to shower overlap leads to a degradation of the achievable energy resolution. Correct simulations of the hadronic shower dimensions are thus of particular importance for the choice of the calorimeter cell size necessary to maximize the particle identification capabilities. The smaller the cell size the higher the number of channels, which has a heavy impact on the cost and the choice of the detector technique.

A large detector with millions of channels can of course not only be built on the assumptions of software simulations. The correct modelling of the detectors and the physical processes has to be proven in test beam experiments. While electromagnetic processes are well understood and can be reliably simulated, hadronic showers are much more complicated as described in chapter 2. Different models describing the passage of hadrons through matter exist and partially make contradictory predictions. In this thesis several models are compared and validated with test beam data.

The simulations have been done with the Geant 4 software toolkit [55]. The modular object-oriented Geant 4 design allows to easily switch between different hadronic models and to compare their predictions. The Geant 4 simulation and the models relevant for this work are introduced in section 7.1.

Besides the physics simulation of the hadronic interactions, the correct modelling of the geometry and the materials used in the detectors is important. The CALICE test beam setup and the detector composition is modelled in the Geant 4 based Mokka application [56] which is described in section 7.2.

In the digitization, the simulated energy deposited in the active detector volumes is transferred to the MIP scale and detector effects such as light cross talk and noise are taken into account. After the digitization steps presented in section 7.3, the simulated events are processed the same way as real data in the reconstruction chain.

7.1. Simulation of Hadronic Interactions

Geant 4 is a software toolkit for the Monte Carlo simulation of the passage of particles through matter. Initially developed for high energy physics applications it nowadays meets a wide variety of requirements from various other fields (e.g. medical and space sciences). By leaving the user the choice of physics processes and models to be applied a large degree of functionality and flexibility is achieved.

Physics Models

The simulation of hadronic interactions is very complicated due to the manifold processes that are possible. None of the existing models describes the passage of hadrons through matter in agreement with experimental data over the full energy range. In Geant 4, coverage of a large particle energy range can be achieved by combining several models valid at different energies. In the following the hadronic models relevant for the investigations presented in this work are introduced.

The String Parton Models simulate the interaction of high energy hadrons (above $3 - 5$ GeV) with a nucleus. Two different string parton models exist: the **Fritiof (FTF)** and the **Quark Gluon String (QGS)** model. They use the same modelling of the nucleons and common code for the string hadronization, but apply model specific string fragmentation functions.

The incident particle may interact with one or several nucleons in the nucleus. The density distribution of the protons and neutrons in the nucleus is modelled using the harmonic oscillator model for light nuclei ($A < 16$) and the Wood-Saxon form for heavier nuclei. The nucleon momentum is randomly chosen between zero and the Fermi momentum. The interactions with the nucleons are then calculated based on the impact parameter, the diffractive and inelastic cross sections and the centre of mass energy.

In the FTF approach the diffractive scattering of the primary particle with the nucleons is realized only via momentum exchange. In the QGS model the hadron-nucleon interaction is mediated via Pomerons. For each of the two scattered hadrons a string is formed, described by its four momentum and two quarks at its ends.

The excited string is stretched due to the motion of its constituents and splits into hadrons and new strings until the energy is too low for further splitting. The longitudinal momentum is split using the Lund or the QGSM fragmentation functions for the FTF and the QGS model, respectively.

The excited nucleus is passed to the models for fragmentation, de-excitation, breakup, etc. A more detailed description of the string parton models can be found in [57, 58].

The Parametrized Models for low **(LEP)** and high **(HEP)** energies have their ori-

gins in the GHEISHA hadronic package [59]. They depend on parametrized fits to measured data and are no detailed hadronic models. Energy and momentum are only conserved on average, but not event by event. These models are outdated but are still commonly used in many Geant 4 physics lists for particles or energy ranges for which no better model exists.

The Cascade Models in Geant 4 are used for the simulation of hadron interactions above a few hundred MeV. Two intra-nuclear cascade models exist: **the Bertini-like (BERT)** cascade, valid up to 10 GeV, and the **Binary cascade (BIC)**, valid up to 3 GeV. In this energy range the deBroglie wavelength of the projectile is comparable (or shorter) to the average distance between the nucleons. The projectile enters the nucleus and reacts with the nucleons. The path length inside the nucleus is calculated based on nucleon densities and parametrized cross-sections.

The BERT model describes the nucleus as spherical shells of constant nucleon density. The nucleons inside a shell are assumed to have a Fermi gas momentum distribution. The results of the single hadron-nucleon interactions are sampled from a set of multi-particle final states. Secondary particles can only be created with energies high enough to occupy a free state according to the Pauli exclusion principle. The secondary particles may in turn interact with the nucleons or are absorbed. The Geant 4 BERT implementation includes the exciton model proposed by Griffin [60]. The collisions in the cascade give rise to excited states, characterized by the number of particles and holes (the excitons). The cascade ends when all particles with high enough energy have escaped the nucleus. The pre-equilibrium model performs evaporation using the exciton configurations. Afterwards the nucleus is de-excited via Fermi-break-up, a simple explosion model, a phenomenological fission model and an evaporation model at equilibrium. More about the BERT model can be found in [61, 58].

In the BIC model the nucleus is a set of discrete nucleons, positioned at sampled locations using the Wood-Saxon distribution for heavier nuclei and the harmonic oscillator shell model for lighter nuclei. The nucleon momenta are selected randomly between zero and the Fermi momentum. In the binary collisions between hadrons and nuclei resonances (e.g. Δ and Λ) are produced. These are subsequently decayed using experimental branching ratios from the Particle Data Group [62]. The production of secondary particles obeys the Pauli exclusion principle. All secondary particles are tracked until they leave the nucleus or the cascade stops. The Binary cascade is over when the average and maximum energy of secondaries is below a threshold. The BIC implementation does not include de-excitation mechanisms. It calculates the excitation energies and hands a configuration of excitons over to the external pre-compound and nuclear de-excitation models. A more detailed description of the BIC model is given in [63, 58].

The Pre-Compound Model describes the nuclear system until it reaches the equilibrium state. In this pre-compound state the number of excitons in the nucleus is above the statistical equilibrium. The pre-compound model provides a smooth transition from the string parton models to the equilibrium de-excitation models and simulates the emission of protons, neutrons, deuterons and alpha particles.

The Chiral Invariant Phase Space (CHIPS) Model describes excited hadronic systems as quasmons, i.e. bubbles of massless quarks (quark-parton plasma). The quark partons are homogeneously distributed over the invariant phase space. The quasmon can be considered as a bubble of the three-dimensional Feynman-Wilson parton gas. The CHIPS model implements a critical temperature, above which the system cannot be heated further. New quark anti-quark pairs are created instead. The quasmons decay via internal quark fusion or by double quark exchange with neighbour quasmons. The generation of the excited nuclear state is implemented for photo-nuclear interactions, nucleon anti-nucleon fusion and pion capture at rest. CHIPS is used widely in combination with other models to describe the photo-nuclear reactions. It can also be used to perform the fragmentation of the excited nucleus simulated with a string model. Recently, CHIPS has been extended and can be used as a stand alone model to simulate interactions of all hadrons over the full energy range. The CHIPS model is described in greater detail in [58, 64, 65, 66].

Physics Lists

In Geant 4, it is the users responsibility to choose which physics processes are simulated and how they are modelled. The several models, valid at certain energy ranges, are included in so called physics lists that are applied in the simulation. Figure 7.1 gives an overview of the physics lists studied and their composition for pions. In chapter 8 the physics lists are tested with showers from pions impinging on the AHCAL. Also in showers initiated by other hadrons, pions are the most frequently produced secondary hadrons. Therefore, the simulation of the pion behaviour has the largest impact on the performance of the physics lists describing the data.

Up two three different hadronic models are combined in one physics list. A smooth transition between the models is realised by switching them randomly in the transition region where their validity in energy overlaps. The probability for the application of a model is varied linearly in the transition region. All studied lists use the same electromagnetic simulation code.

LHEP is a combination of the parametrized models. LEP is applied in the energy range $0 - 50$ GeV. HEP is applied above energies of 25 GeV.

QGS_BIC applies the QGS model at energies above 12 GeV and the BIC cascade below 1.3 GeV. In the transition between 1.2 and 25 GeV the LEP model is used.

QGSP_BERT combines the QGS model with the Pre-Compound model at energies above 12 GeV. The Bertini cascade is used below 9.9 GeV. In the transition between 9.5 and 25 GeV the LEP model is applied. This physics list is used by the LHC experiments.

QGSP_FTFP_BERT is a variant of the QGSP_BERT physics list where the LEP model is replaced by the Fritiof model in the energy range $6 - 25$ GeV. The Bertini model is applied from energies below 8 GeV. The energy range where the QGS model is applied is above 12 GeV.

FTFP_BERT uses the Bertini cascade for energies below 5 GeV. The Fritiof Model is applied above 4 GeV. The Pre-Compound model is used in the pre-equilibrium phase of the nucleus de-excitation.

FTFP_BERT_TRV is a variant of FTFP_BERT in which the transition between the Bertini cascade and the Fritiof model is in the range $6 - 8$ GeV.

FTF_BIC applies the Fritiof model above energies of 4 GeV. For the treatment of secondary particles below 5 GeV the Binary Cascade model is used.

CHIPS is a physics list using the CHIPS model for all hadrons over the full energy range. This extension of the CHIPS model has become available with Geant 4.9.3 and is still subject to changes. In this work the patched version Geant 4.9.3.p01 is used.
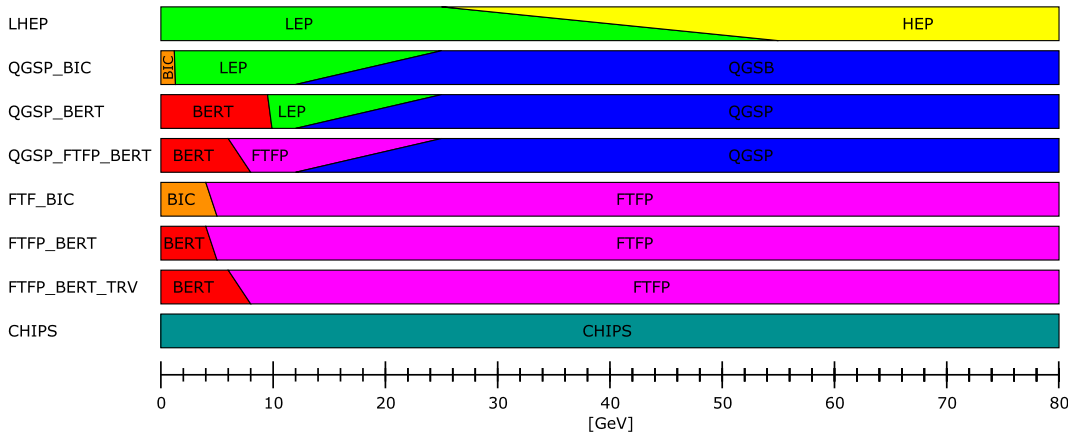

Figure 7.1.: Models applied at different energies in several physics lists for the simulation of pions in Geant 4.9.3.

7.2. Test Beam Simulation

The simulations investigated in this thesis have been done using the Geant 4 based Mokka application (version 7-02). In Mokka several different geometry models are available. Full ILD detector geometries as well as the CALICE test beam setup can

be simulated. For the simulations of the CERN 2007 test beam setup in this study, the model TBhcal07 [67] was used .

Particle Beam and Instrumentation

Figure 5.3 shows the test beam setup and the dimensions used in the simulation. The origin of the coordinate system is at the centre of the exit window of the last drift chamber (DC1). The beam-line geometry is modelled from the Čerenkov entrance window on downstream. All scintillators used for the triggering, drift chambers, vacuum pipes with their beam windows and air volumes are implemented.

The Geant 4 particle gun was placed at $z = 39$ m, in front of the Čerenkov entrance window. The primary particle is simulated with the momenta of the test beam particles. The uncertainty of the test beam particle momentum is taken into account by using a Gaussian smearing of the simulated particle momentum. The primary particles x- and y-direction is also smeared by a Gaussian distribution applying σ_x and σ_y derived from the beam profiles measured with the drift chambers.

Detector Material

The material composition of the ECAL, the AHCAL and the TCMT is modelled in Mokka. For the simulation of data runs without the ECAL in front it can be removed from the beam line. In the following only the AHCAL is geometry is summarized.

The 38 AHCAL layers of 90×90 cm^2 area are modelled as a sandwich structure composed of different materials. Figure 7.2 sketches the composition of a single AHCAL layer (not to scale). The dimensions and the materials simulated are given in table 7.1. The scintillator layer is subdivided into 1×1 cm^2 tiles. In the simulation, only the energy deposited in the single tiles is stored. A detailed description of the AHCAL model in Mokka is given in [67].
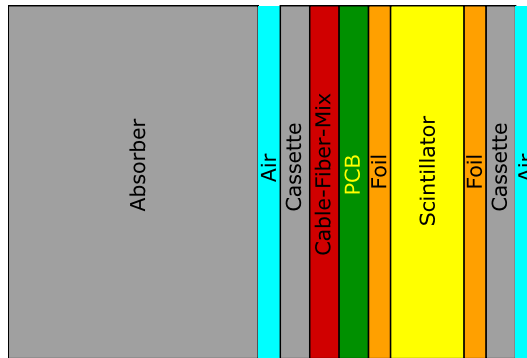

Figure 7.2.: Composition of a single AHCAL layer in the simulation model.

Volume	Material	Thickness [mm]
Absorber	Steel S235JR	17.00
Air	Air	1.25
Cassette	Steel	2.00
Cable-Fibre-Mix	Air,PVC,Polystyrole	1.50
Printed Circuit Board (PCB)	Si,O_2,C,H,Br	1.00
Foil	Polystyrole	0.12
Scintillator	Polystyren	5.00

Table 7.1.: Materials used in the AHCAL simulation model.

Birks Law

Shielding effects in the scintillator material saturate the scintillation process at high ionization densities. This causes a non-linearity of the light yield. Birks Law [68] describes the light yield unit per length dL/dx for high ionization densities dE/dx:

$$\frac{dL}{dx} \propto \frac{dE}{dx} \cdot \frac{1}{1 + kB \cdot \frac{dE}{dx}} \quad .$$ (7.1)

The parameter kB depends on the scintillator material. In the simulations done for this study $kB = 0.007943\,\text{cm/MeV}$ was applied, which is the value measured in [69] for scintillators used in the ZEUS experiment. Currently an improvement of the implementation of Birks law in Geant 4 is ongoing with the goal to include the recently measured kB factor for the AHCAL scintillator material [70].

Time Cut

After getting coincident trigger signals, the read out electronic samples the calorimeter signal in a defined time window. Low energy neutrons created in the hadronic cascade can travel a significant amount of time before they interact in the calorimeter. The signal from the late energy depositions might not or only partially be recorded. A time cut of 150 ns is applied in the simulation to account for this effect.

7.3. Digitization

Geant 4 simulates all the physics processes at the particle level. The output of Mokka is the energy deposited in the active material, i.e. scintillator tiles of $1 \times 1 \times 0.5$ cm^3 volume. To be able to compare Monte Carlo simulations to data, it is necessary to simulate detector effects such as light cross talk, non-uniform detector response and the SiPM non-linearity. In the AHCAL digitization the simulated energy per volume is transferred to ADC counts including all known detector effects and calibration corrections. This way both digitized simulations and data can be processed by the

same reconstruction chain. This method allows to study detector effects in detail and to compare the Monte Carlo models to data using realistically reconstructed physics observables. In the following the single digitization steps are briefly explained. A detailed description of the digitization procedure can also be found in [71].

Ganging

The simulation of the AHCAL is done with a cell size of 1×1 cm^2. In the ganging step the 1×1 cm^2 cells are combined to the 3×3 cm^2, 6×6 cm^2 and 12×12 cm^2 sizes used in the AHCAL prototype.

Light Cross Talk

On the borders of the tiles part of the light is not reflected and leaks to the adjacent tiles. In the digitization, a fraction of the energy deposited in a tile is distributed over its direct neighbours in the same layer to simulate the light leakage. In the version of the digitization software used throughout the analysis presented in this thesis, the light cross talk is simulated assuming that from each 3 cm-long tile edge 2.5 % of the scintillator light leaks homogeneously to the neighbouring tile [50].

Transfer to the MIP Scale

To be able to compare the simulation to data, the simulated energy deposited in the single detector cells has to be converted to the MIP scale used in the detector calibration. For this purpose the passage of muons through the calorimeter is simulated. The most probable value of their energy deposition per cell is fitted and gives the keV-per-MIP factor used for the conversion. The absolute value is dependent on the range cut set in Geant 4 and the simulated detector effects such as Birks law. For the simulations presented in this work a factor of 816 keV per MIP was applied:

$$A_i \, [\text{MIP}] = E_i \, [\text{keV}] \quad / \quad 816 \, \text{keV}, \tag{7.2}$$

where E_i is the simulated energy deposition in a single calorimeter cell i and A_i the simulated signal in units of MIP.

SiPM Non-Linearity

The SiPM non-linearity is simulated and the signal amplitude converted to units of SiPM pixels fired using the MIP, gain, inter-calibration factors, and the saturation curves introduced in chapter 6:

$$A_i \, [\text{pix}] = f \left(A_i \, [\text{MIP}] \quad \cdot \quad \frac{G_i[\text{ADC}]}{M_i[\text{ADC}]} / I_i \right) \; . \tag{7.3}$$

Statistical Fluctuations

The statistical fluctuations due to the limited number of SiPM pixels is simulated by randomly smearing the pixel amplitude with a Poisson distribution:

$$A_i[\text{pix}] \rightarrow A_i'[\text{pix}]. \qquad (7.4)$$

Transfer to the ADC Scale

To treat the simulations in the same way, the cell amplitudes still have to be converted to the ADC scale of the raw data:

$$A_i\ [\text{ADC}] = A_i'\ [\text{pix}] \quad \cdot \quad \frac{G_i[\text{ADC}]}{I_i} \ . \qquad (7.5)$$

Noise

During the data taking the detector noise originating from the SiPMs and the read-out electronics is recorded using a random trigger. In the comparison of Monte Carlo and data, the noise extracted from a data run at a certain beam energy is added to the simulated cell signals at the same beam energy. This way pedestal shifts and noisy cells are also included in the simulation.

7.4. Energy Decomposition

The Mokka software allows to determine the energy deposited by a given particle type in a certain simulated material volume. However, this information is only available in the first stage of the simulation chain, still at the $1{\times}1$ cm^2 tile level, and it is lost in the first step of the digitization, i.e. the ganging. Due to the non-linear detector effects, threshold effects and non-Gaussian calibration smearing, data and simulation comparison can only be performed at the digitized MIP level. In the following, a method developed to retrieve the visible energy deposition by single particles event-by-event after the digitization is briefly described:

- A collection of visible energy is created for each particle type. The collections are filled event-by-event at the $1{\times}1$ cm^2 tile level.
- The $1{\times}1$ cm^2 hits divided in particle-type specific collections are then ganged, and new collections are created containing information at the real size tile level - the same way as for the hits not decomposed by particle type.
- For the merged hits the ratio between energy deposited by a certain particle type and the total energy are calculated. These ratios are used as weights to obtain, after the digitization steps, the fractions of particles of various type.
- The standard AHCAL digitization is applied to all hits, including a threshold cut of 0.5 MIP to reject noise.
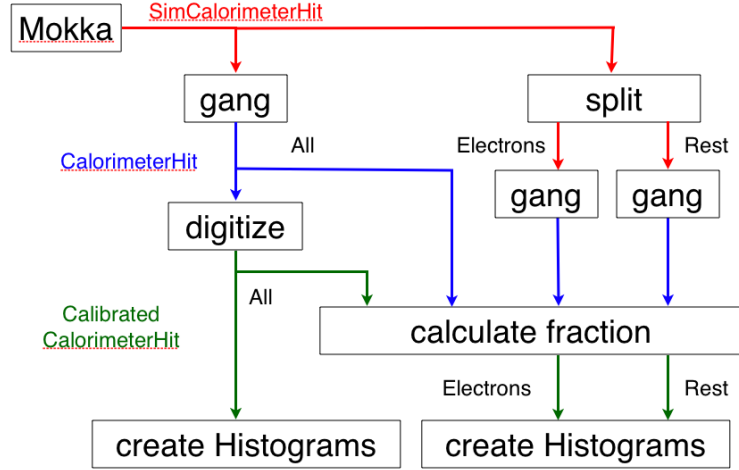
Figure 7.3.: Flow chart of the developed technique to access the energy deposited by single particle types in Mokka. For simplicity the process is only shown for one particle type (Electrons) and all other particles (Rest).

- After digitization the total energy at the MIP scale is multiplied by the weights previously obtained to get the digitized fractional energy of each particle type.

The procedure is visualized in the flow chart in figure 7.3. The result of the visible energy decomposition is shown in figure 7.4 for 80 GeV pions. The filled histogram shows the total energy sum from a simulation with the FTFP_BERT physics list. The other histograms in are the distributions of visible energy deposited by individual particle types, i.e. electrons, positrons, protons, and mesons (pions and kaons). The decomposition technique is realised in a modular way and arbitrary particle types can be specified by their identification code in the Particle Data Group tables [72]. The information can be used to investigate disagreements between data and simulation in the same observables at a deeper level of detail, as it will be shown in the following chapter.
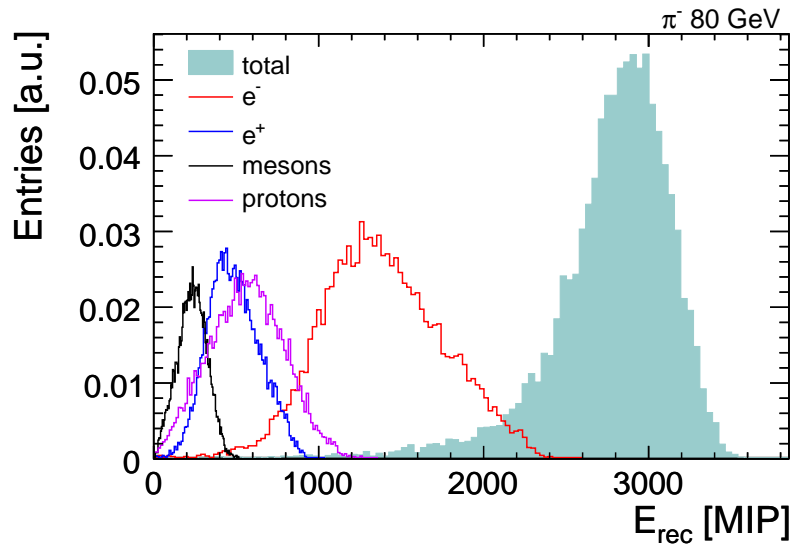
Figure 7.4.: The breakdown of the reconstructed energy in the AHCAL into the contributions from various particle types in the shower for simulated 80 GeV pion showers with the FTFP_BERT physics list: $e^{\pm}$, p, and mesons ($\pi^{\pm}$ and $K^{\pm}$).

8. Hadron Shower Analysis

The analysis presented in this chapter is based on data acquired during the test beam at the CERN SPS site. The results are published as preliminary in a CALICE analysis note [73]. The setup and the beam line instrumentation is described in chapter 5.1. Hadronic showers caused by negative pions in the energy range from 8 to 80 GeV are studied. Runs with the Si-W ECAL in front of the AHCAL and the beam impact direction perpendicular to the detector front (rotation angle $\theta = 0°$) have been chosen. The very high granularity of the AHCAL allows detailed studies of hadron showers at an unprecedented level of precision.

It was already mentioned before in this thesis that Monte Carlo simulations are an essential tool in the detector development. Diverse models for the simulation of hadronic showers are available and predict partially contradictory results. This motivates the comparison of different Monte Carlo simulations to the measured data from real particles at the test beam presented throughout this chapter. The simulations have been done with the Geant 4[1] based Mokka[2] application and are described in detail in chapter 7. Up to now, no model exists that reproduces the experimental results over the full energy range. In order to cover energies of particles shower taking place in detectors at collider experiments, several models are combined together in physics lists. Eight physics lists have been picked for this analysis and are evaluated along a number of variables.

When investigating the impact of the single models in the simulations, one has to keep in mind that the energy ranges in which they are applied. The full particle energy is only available in the very first hard interaction. These energy ranges are listed in figure 7.1 for pions. Not only pions are created as secondary particles, however they dominate the shower development as they are created most frequently. Due to the lower energies of the secondary particles created in the shower process, the low energy models also contribute at the highest beam energy studied in this chapter.

For example, the results for 80 GeV pion showers simulated with the QGSP_BERT physics list are dominated by the QGSP model, but also driven by the LEP and the Bertini models. The measurements at beam energies below 25 GeV are of particular interest, since it is possible to study the influence of the low and medium energy models and compare them to data. In case of QGSP_BERT, the QGS model is not used at energies below 12 GeV, therefore one can test the interplay of the LEP

---

[1] All simulations have been done with Geant version 4.9.3 (if not stated differently).
[2] Mokka version 7-02

and the BERT model. With the 8 GeV measurements, the performance of the Bertini model can be checked since it is the only model applied at this energy in QGSP_BERT.

8.1. The First Hadronic Interaction

According to equation 2.10, the probability for a primary hadron to travel the distance z inside the calorimeter before the first hadronic interaction is $P(z) = \exp(-z/\lambda_{\text{eff}})$, where λ_{eff} is the effective nuclear interaction length of the AHCAL material composition (cf. equation 2.11). The position inside the AHCAL where hadronic showers start to develop fluctuates because of the statistical nature, which has an impact on the energy resolution. Showers starting deep in the calorimeter have a high probability to leak outside and deposit less energy in the active material. Also longitudinal shower profiles along the axis of impact are smeared due to this fluctuation. Exploiting the fine longitudinal segmentation of the AHCAL, it is possible to determine the position of the first hadronic interaction and to correct the measurements accordingly.

Detection Method

The event display in figure 8.1(a) shows the energy deposition of a single 18 GeV pion. It enters from the left and leaves a track in the calorimeter similar to a minimum ionizing particle. The first hadronic interaction takes place in layer 15 where secondary particles are created and a shower starts to develop. The energy deposition increases after this point.

A simple algorithm based on sum of energy per calorimeter layer has been initially developed by M. Chadeeva [74]. The layer closest to the first hadronic interaction is found using the accumulated average energy deposited:

$$A_i = \sum_{k=0}^{i} E_k/(i+1), \tag{8.1}$$

with E_k being the energy deposited in layer k of the AHCAL (layer 0 is the first from the calorimeter front).

The layer i where an hadronic shower starts is defined as the first layer for which any of the following two criteria is fulfilled:

- $(A_i + A_{i+1}) > A_{\text{thr}}$ and $(N_i^{\text{hit}} + N_{i+1}^{\text{hit}}) > N_{\text{thr}}$,
- $E_{i+1} > E_{\text{thr}}$,

where N_i^{hit} is the number of calorimeter cells above the 0.5 MIP threshold in layer i. In the latest official version of the algorithm the threshold parameters were fixed to $A_{\text{thr}} = 6.5$ MIP, $N_{\text{thr}} = 8$ and $E_{\text{thr}} = 25$ MIP.

Figure 8.1 shows the average values of $(A_i + A_{i+1})$, $\left(N_i^{\text{hit}} + N_{i+1}^{\text{hit}}\right)$, and E_i as a function of the layer number relative to the first hadronic interaction for simulated 18 GeV pion showers. The information on the true layer closest to the first hadronic interaction is available in the simulation and defines the zero point of the x-axis. One can clearly see that on average all three values exceed the thresholds indicated by the dashed line at the position in the calorimeter where the shower starts. However, these are average values with large event to event fluctuations, which is the reason for combining the two requirements on $(A_i + A_{i+1})$, and $\left(N_i^{\text{hit}} + N_{i+1}^{\text{hit}}\right)$ and the additional criterion with the energy per layer E_{i+1}.
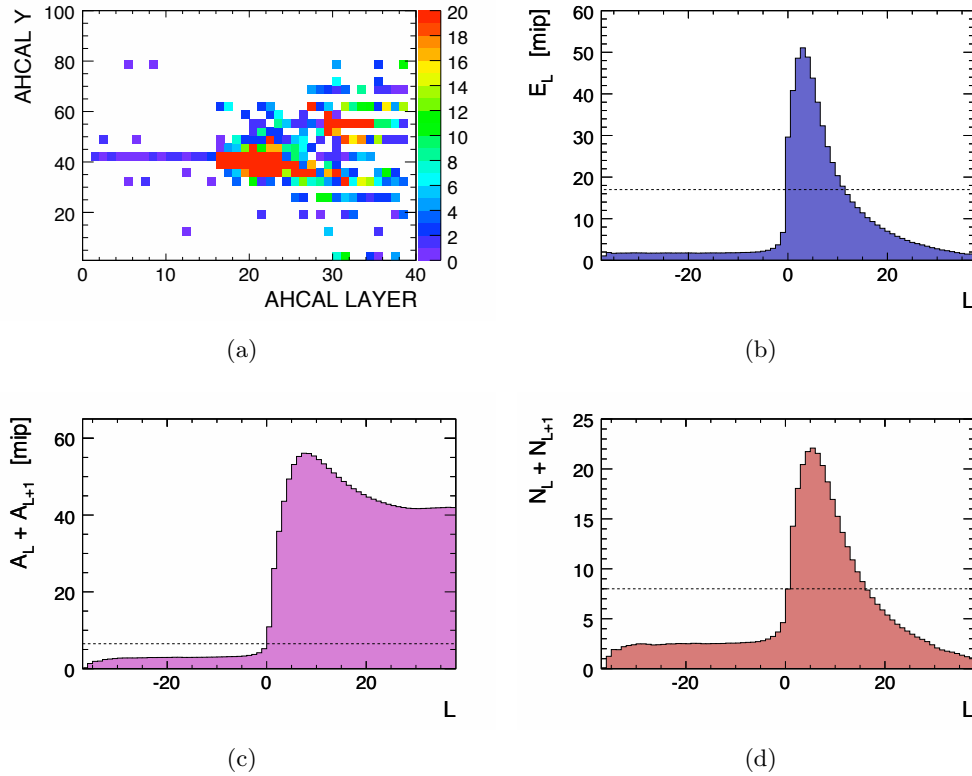

(a)

(b)

(c)

(d)

Figure 8.1.: (a) Event display of a 18 GeV pion starting to shower in layer 15. Average energy deposition (b), the accumulated average energy (c), and the number of hits in two adjacent layers (d) for 18 GeV pion showers as a function of the AHCAL layer relative to the first hard interaction.

Performance of the Algorithm

In order to evaluate systematic effects due to the algorithm, the found layer of the first interaction is compared with the true one, defined as the layer where the first hadronic interaction of the primary particle travelling through the calorimeters

takes place in the simulation. If this is either inside an active AHCAL layer or in the absorber plate just before it, that layer is assumed to be the true starting point.

Figure 8.2 shows the performance of the algorithm. The correlation between the true shower starting layer and the one found by the algorithm for $18\,\mathrm{GeV}$ pions, shown in figure 8.2(a), is 97%. The average difference between the two, shown in figure 8.2(b), is 0.5 AHCAL layers.

However, the performance of the algorithm depends on the beam energy and the physics list used. For the analysis presented in this thesis, the algorithm was modified to reduce these dependencies. The fixed threshold parameter $E_\mathrm{thr} = 25\,\mathrm{MIP}$ of the algorithm has been replaced by a linear function of the energy E_vis deposited in the calorimeter $E_\mathrm{thr}(E_\mathrm{vis}) = m \cdot E_\mathrm{vis} + b$, which is shown in figure 8.2(c). The information of the beam energy, which is only available at the test beam, is not used by the algorithm.

The correlation between the true first interaction position and the one found by the algorithm is shown as a function of the beam energy in figure 8.2(d). Before the improvement (dashed line) the correlation increased with growing beam energy from approximately $82\,\%$ at $8\,\mathrm{GeV}$ to $91\,\%$ at $80\,\mathrm{GeV}$. After the refinement, the energy dependency almost vanishes completely and the value raises to $(91 \pm 1)\,\%$.

Figures 8.2(e) and 8.2(f) show the mean[3] difference $< \Delta >$ between the true shower starting layer and the one found by the algorithm for the FTF_BIC physics list as a function of the beam energy before and after the improvement. The uncertainty is indicated by the grey band which shows the range of Δ for 66% of all events. One can see a clear reduction of the energy dependency, and the asymmetry in the uncertainty vanishes.

Still, the performance of the algorithm depends on the physics list used in the simulation (cf. appendix A), and an implementation of energy dependent thresholds also for the variables $(A_i + A_{i+1})$ and $\left(N_i^\mathrm{hit} + N_{i+1}^\mathrm{hit}\right)$ is suggested. In the following this is taken into account in the uncertainty estimation when the different physics lists are compared to data.

8.2. Event Selection

The data obtained from negative pions showering in the AHCAL have been chosen for this analysis. As the particle beams delivered at the test beam site are not pure, pions need to be separated from electrons and muons in the same run.

To get a clean data sample several selection criteria have to be applied. Information from the veto counter, the muon counter and the multiplicity counter in the beam line instrumentation (cf. figure 5.3) are used. In addition, the energy deposited in

---

[3] The mean value of the histogram shown in figure 8.2(b) that is spoiled by the entries in the very high and low bins. In the text, the arithmetic mean of the central 90% of the entries is stated, which is a better measure for the uncertainty of the algorithm.

the ECAL and the position of the first hard interaction are used.

Only events fulfilling the following criteria are accepted:

- beam trigger: a coincident signal from both $10 \times 10 \, \text{cm}^2$ scintillators (Sc1 and Sc2);

- rejection of multiple particle events: no signal above threshold may be present in the veto and multiplicity (Sc2) counters;

- muon rejection: no signal present in the $100 \times 100 \, \text{cm}^2$ scintillator wall (Mc1);

- showers starting in the front part of the AHCAL: the Primary Track Finder algorithm has to find a single track in the ECAL and the first interaction has to take place in the AHCAL layers $1 - 10$.

The requirement on the algorithm to find a single track in the ECAL and to find the first interaction point in the AHCAL is an electron rejection, since effectively all electrons start to shower in the 24 X_0 radiation lengths of the ECAL. It is also an additional rejection of empty events caused by fake triggers, multiple particle events, and muons.

The restriction on showers starting in the front part of the AHCAL minimizes the leakage of shower energy into the TCMT.

Table 8.1 shows the selection of runs chosen for this analysis. For all energies, at least $100 \cdot 10^3$ events have been recorded. At lower energies the amount of electrons in the beam is higher which leads to a smaller pion statistics.

Energy	Tot. ev.	Ev. after cuts	Efficiency
8 GeV	105773	14494	13.7 %
10 GeV	178504	26414	14.8 %
12 GeV	261601	45113	17.2 %
15 GeV	179131	36677	20.5 %
18 GeV	178369	37662	21.1 %
20 GeV	180279	38764	21.5 %
25 GeV	177620	38492	21.7 %
40 GeV	223952	49628	22.2 %
50 GeV	225897	50157	22.2 %
80 GeV	229843	51878	22.6 %

Table 8.1.: Set of runs investigated in this note. The shower is required to start in the front part of the AHCAL. The number of events after the event selection is given in column three and as a relative value in the last column.

Figure 8.3 shows the reconstructed energy in all three CALICE prototypes before and after the requirement on the layer where the shower starts. The energy distribution in the ECAL after this requirement is consistent with that of a minimum ionizing

particle. A large fraction of the pion energy is contained in the AHCAL. A tail to smaller energies is still present in the AHCAL energy distribution due to leakage to the TCMT. No further effort is made to select showers contained in the AHCAL in order to avoid a bias of the longitudinal shower profiles to a particular type of events. The bottom row shows the correlation between the energy deposited in the TCMT and the sum of energy deposited in the ECAL and the AHCAL. One can clearly see a peak at $\approx$ 1-2 GeV due to muons and late pion showers before applying the cuts (left) which are no longer present afterwards (right).

8.3. Measurement of the Hadronic Interaction Length

The coordinate of the shower starting position is the point closest to first nuclear interaction in the AHCAL prototype. The distribution of the shower starting point found with the Primary Track Finder algorithm is shown in figure 8.4(a) measured with 25 GeV negative pion showers. For this measurement, it was only requested that the shower starts in the AHCAL - the requirement on the shower to start which is introduced in section 8.1 is not applied. From this graph, one can directly extract the effective nuclear interaction length $\lambda_{\mathrm{int}}^{\pi}$ in the material mix of the AHCAL. It is obtained by fitting an exponential function to the distribution of the shower starting point using the maximum likelihood method. The first two layers are excluded since the uncertainty of the algorithm is largest there. In addition, the last eight layers are excluded due to the coarse module structure there. The algorithm has not been adapted to the lower number of cells in these layers and its performance deteriorates. The dip at $z = 800$ mm is also visible in all other investigated runs and can be attributed to dead cells or missing calibrations in layer 26.

Figures 8.4(b)-8.4(d) show the extracted values for the interaction length for data and the various physics lists. No energy dependence of the interaction length is observed for data. The measurements yield an average of $\lambda_{\mathrm{int}}^{\pi} = (29 \pm 1)$ cm. The measured values for the data at the several energies and the uncertainties are summarized in table 8.2. The statistical error on $\lambda_{\mathrm{int}}^{\pi}$ extracted from the fits for data and simulations is $0.5 - 1\%$. The uncertainty of the algorithm distorts the exponential form of the shower starting point distribution and translates into a systematic error on the interaction length. The systematic error is estimated from the comparison of the true interaction length extracted from the simulations to the one found with the algorithm. It depends strongly on the performance of the algorithm for the several physics lists at different beam energies (also cf. appendix A) and varies from roughly 5% at 8 GeV to approximately 3% at 80 GeV.

All physics lists agree with the data in the uncertainty, except for LHEP which gives a significantly smaller value and CHIPS which gives a higher value. This result is not surprising since the interaction length is directly proportional to the inelastic pion-nucleon cross sections. The cross sections are in common to all physics lists apart from LHEP and CHIPS which have their own implementations [75]. One

can see clearly the effect of the LEP model applied at energies below $20\,\mathrm{GeV}$ in QGSP_BERT (LEP used from 9.5 to 25 GeV) and QGS_BIC (LEP used from 1.2 to 25 GeV). For QGSP_BERT an increase of λ_{int} below $10\,\mathrm{GeV}$ is observed, which is the energy range where the Bertini cascade is used in this physics list.

Energy [GeV]	8	10	12	15	18	20	25	40	50	80
λ_{int} [mm]	288	289	294	291	294	291	289	290	293	291
Δ_{fit} [%]	1.01	0.76	0.59	0.65	0.64	0.63	0.63	0.56	0.55	0.54
$\Delta_{\mathrm{algorithm}}$ [%]	5.43	4.36	3.36	3.43	2.83	2.94	3.18	3.27	3.11	2.72
$\Delta_{\mathrm{calibration}}$ [%]	0.24	0.35	0.36	0.28	0.2	0.22	0.20	0.21	0.21	0.24

Table 8.2.: Measured pion interaction length in the AHCAL with systematic errors. The fit uncertainties Δ_{fit} are comprised in the stated uncertainty of the algorithm $\Delta_{\mathrm{algorithm}}$. The contributions from the calibration uncertainties $\Delta_{\mathrm{calibration}}$ are negligible.

8.4. Visible Energy

The visible energy in the AHCAL is the sum of the single cell signals. For every event that passed the selection described in section 8.2, the single cell amplitudes are calibrated to the MIP scale as described in chapter 6. In order to reject noise, the signals from calorimeter cells with an amplitude below $0.5\,\mathrm{MIP}$ are not taken into account. The signal from a cell above this threshold is referred to as hit.

The distribution of the hit energy sum is shown for $80\,\mathrm{GeV}$ pion showers in figure 8.5. The expected Gaussian shape of the energy sum distribution is disturbed by a tail to lower energies due to showers not fully contained in the AHCAL. For these, only a fraction of the usually visible energy can be detected. In the following, the mean value of the energy sum without leakage correction of several physics lists is compared to data. Figure 8.6(a) shows the mean energy sum as a function of the beam energy for the data. The ratio between simulations and data is plotted in figures $8.6(\mathrm{b}) - 8.6(\mathrm{d})$.

The CHIPS model has recently been extended and can now be applied over the full energy range. This is of interest because no transition between different models is necessary in this case. Here the CHIPS implementation in the patched version Geant $4.9.3\mathrm{p}01$[4] is presented which is known to have the low energy inelastic neutron cross-sections not properly implemented [76]. A visible energy too high by $\sim 7\,\%$ compared to data is observed. However, the ratio of response between CHIPS and the data is constant within $1.5\,\%$ over the full energy range, while all other physics lists show a stronger energy dependent behaviour.

---

[4]CHIPS was already available in the official released version 4.9.3 but had a poor performance due to accidentally wrong adjusted parameters.

The LHEP physics list originates from the old GHEISHA simulation code. The LEP and HEP models are however still in use by other physics lists (e.g. in QGSP_BERT) and should be replaced in future Geant 4 versions. An underestimation of the visible energy in the calorimeter by $5 - 10\,\%$ is found for LHEP.

The performance of the QGSP_BERT and the QGS_BIC physics lists in describing the data is strongly energy dependent. One can clearly see the transition to the LEP model in the in the range $9.9 - 25\,\mathrm{GeV}$ and $1.3 - 25\,\mathrm{GeV}$, respectively. The higher value at $8\,\mathrm{GeV}$ compared to the 10 and $12\,\mathrm{GeV}$ points seems to be an artefact due to the LEP model, since QGSP_BERT and QGS_BIC are the only physics lists applying LEP and it also visible in LHEP. Both lists tend to underestimate the calorimeter signal at lower energies and to overestimate it at higher beam energies. The visible energy predicted by QGS_BIC is slightly below that of QGSP_BERT which becomes more distinct at energies below $12\,\mathrm{GeV}$. This can be attributed to the difference between the Binary and the Bertini cascade which is also observed for the combination with the Fritiof models in the physics lists discussed below.

In the QGSP_FTFP_BERT the LEP model is replaced by the FTFP model. A behaviour much more similar to the FTFP_BERT physics list is observed. Note that the response is higher compared to QGSP_BERT even at beam energies above 25 GeV where both apply the QGS model. The reason for this is the contribution of FTFP_BERT in the reaction of secondary particles.

While the FTF_BIC physics list applies the Fritiof model at high energies and the Binary cascade at low energies with a transition between the two in the range 4-$- 5\,\mathrm{GeV}$, the FTFP_BERT model uses the Bertini cascade for low energies with the same transition range. For both, a smooth increase in the ratio between simulation and data is observed with growing beam energies. The FTF_BIC physics list predicts a too low calorimeter signal at pion energies below $12\,\mathrm{GeV}$ and is consistent with the data above. A higher response compared to FTF_BIC is found for the FTFP_BERT physics list which reproduces the data within the uncertainty except for $80\,\mathrm{GeV}$. A different transition region of $6 - 8\,\mathrm{GeV}$ is used in the FTFP_BERT_TRV list. However, in the studied energy range no impact on the simulated calorimeter response is visible. To investigate this, lower energies would be necessary.
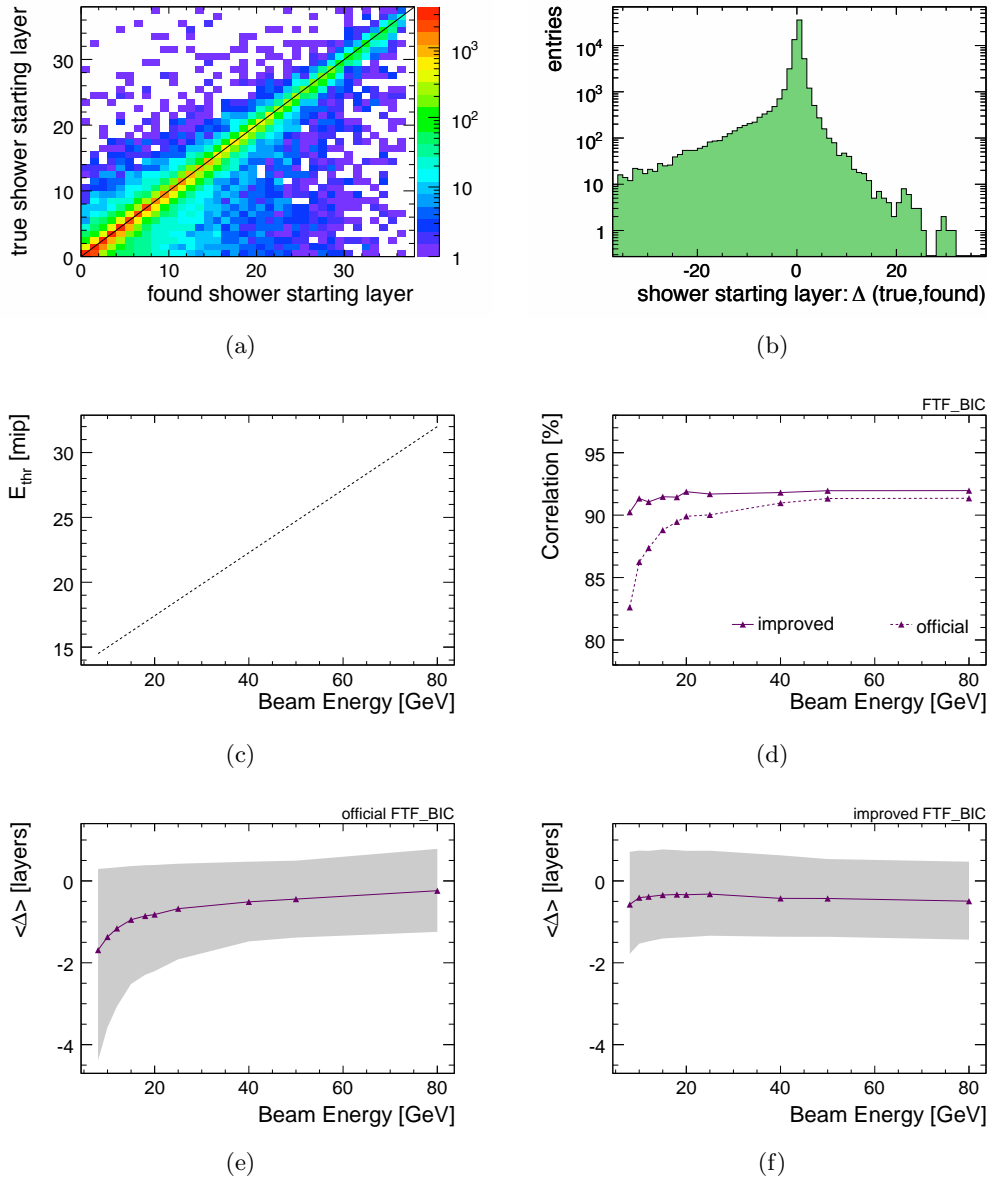
(a)

(b)

(c)

(d)

(e)

(f)

Figure 8.2.: Correlation (a) and difference (b) between the true layer of the first hard interaction in Monte Carlo and the one found by the algorithm for the FTF_BIC physics list simulating an $18\,\text{GeV}$ π^- beam. (c) Threshold E_{thr} as a function of the visible Energy Evis in the calorimeter. (d) Correlation before (dashed line) and after (solid line) the refinement of the algorithm as a function of the beam energy. Mean difference before (e) and after (f) the modification.
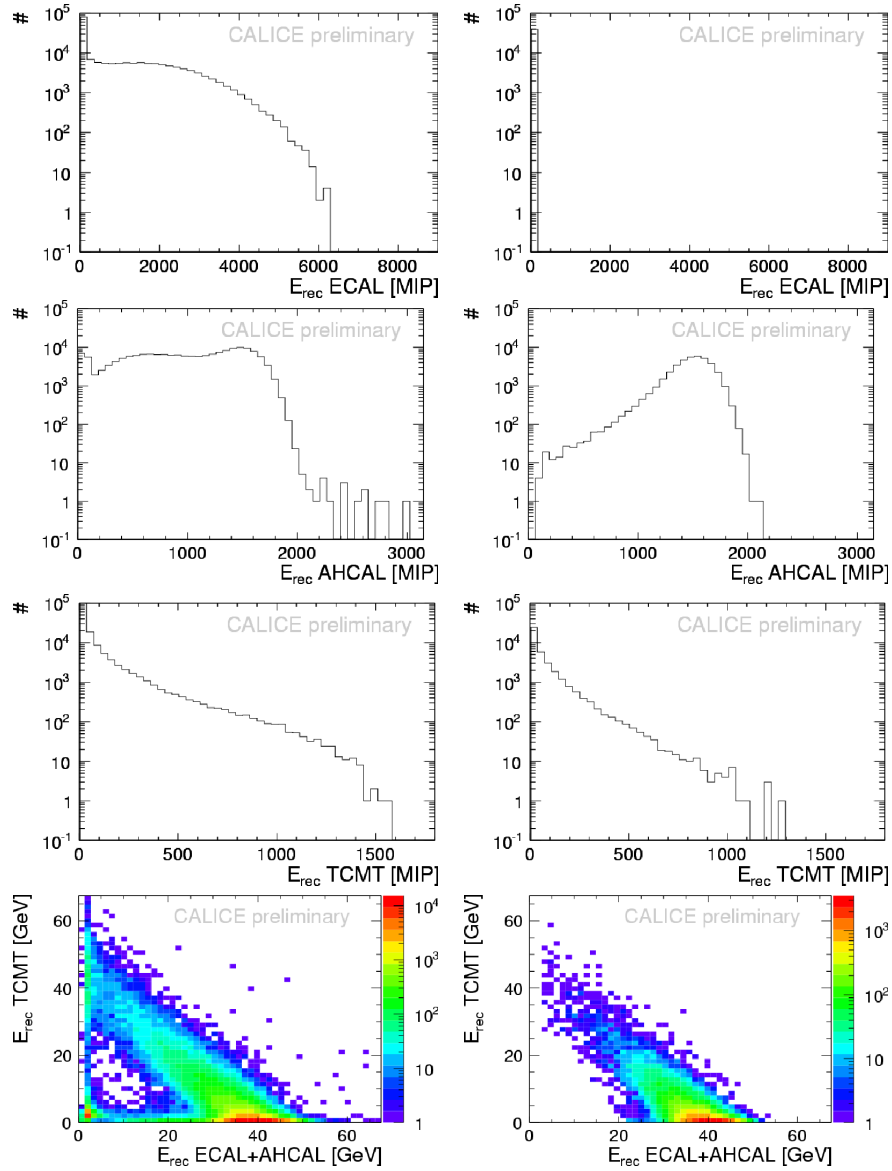
Figure 8.3.: Distributions of reconstructed energy from 40 GeV pion showers in all three CALICE calorimeters before (left) and after (right) applying the event selection. In the bottom plots the correlation between the energy deposited in the TCMT and the sum of the energy deposited in the ECAL and AHCAL in units of GeV is shown.

(a)

(b)

(c)

(d)
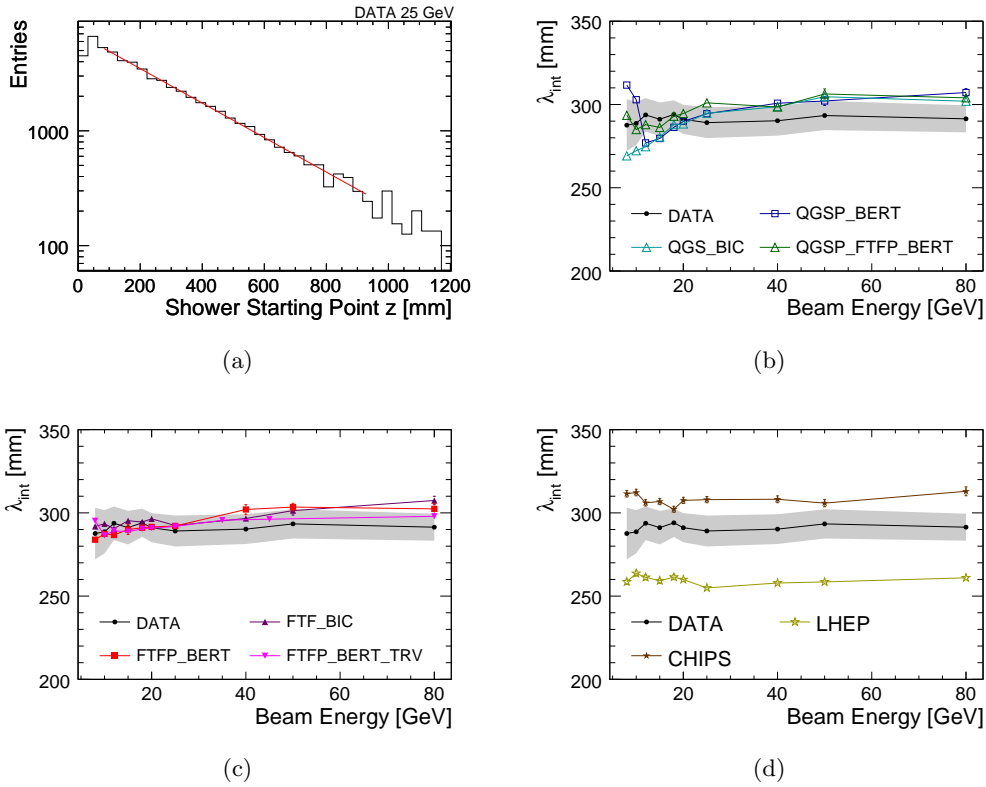
Figure 8.4.: (a) Distribution of the shower starting position found with the Primary Track Finder algorithm. (b-d) Extracted values for the interaction length from data and simulation models. The error bars shown are the uncertainty from the fitting. The uncertainty from the algorithm to determine the first interaction layer is indicated by the grey band around the data points. The contribution of the calibration uncertainties is negligible (cf. table 8.2).
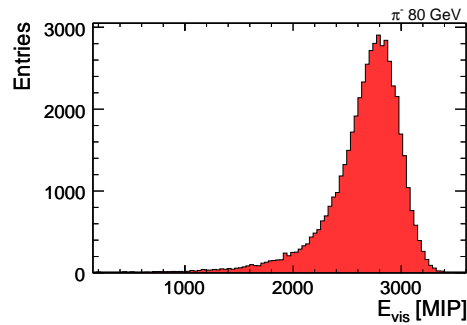

Figure 8.5.: Visible energy sum spectra for 80 GeV pion showers in the AHCAL. The tail at lower energies is due to showers not fully contained.
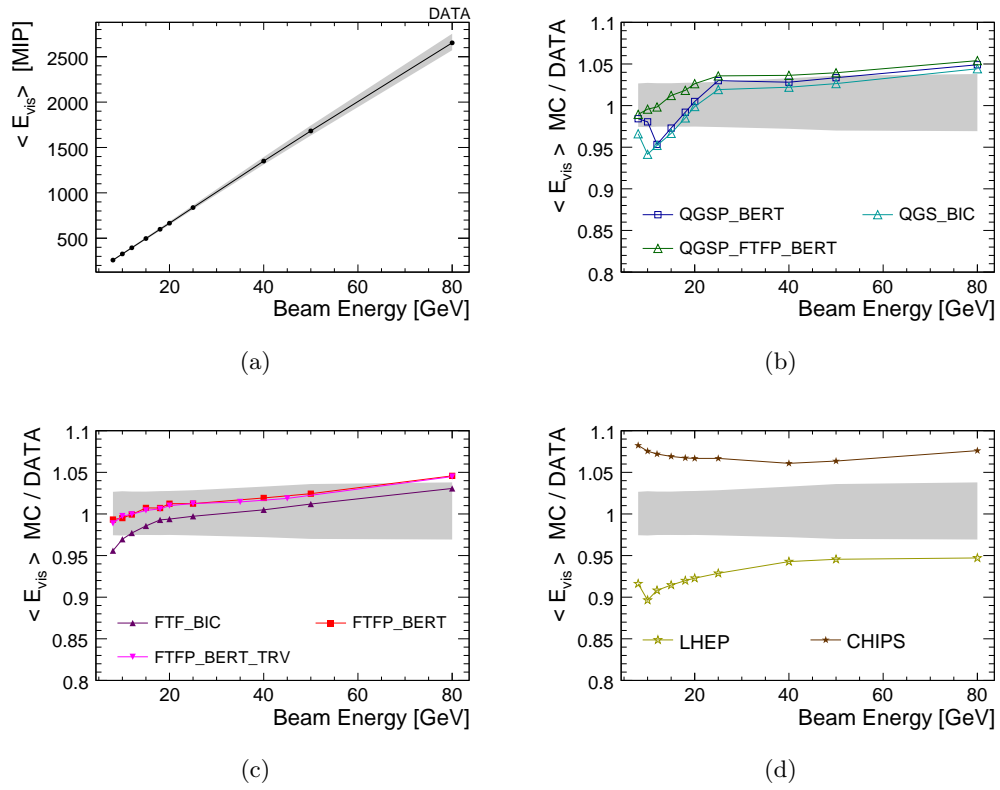
Figure 8.6.: (a) Reconstructed mean energy sum from data as a function of the beam energy. (b)-(d) Ratio of the mean energy sum between simulations and data. The error band shows the calibration uncertainty on the data.

8.5. Shower Shapes

For the Particle Flow approach, the overlap of showers in the calorimeters is a critical parameter as the achievable energy resolution depends on its capability to separate them. Therefore a realistic modelling of the radial and longitudinal shower development in the simulations is very important for the design of the detectors and the development of the Particle Flow algorithm.

Longitudinal Shower Development

The fine segmentation of the AHCAL into 38 layers can be used to study the longitudinal shower development in great detail. The longitudinal shower profile is defined as the average energy deposited in each layer as a function of the calorimeter depth.

Using the position information on the first hard interaction of the impacting hadrons, the intrinsic longitudinal shower development can be deconvolved from the fluctuation of the shower starting position. In figure 8.7 two longitudinal profiles are shown: one shower profile from the calorimeter front face (filled) and one relative to the first interaction point (black line). The layer-to-layer fluctuations visible in the profile from the calorimeter front are due to calibration uncertainties and dead channels. They are smeared out in the relative profile which looks shorter and much more similar to an electromagnetic shower profile. In the following the longitudinal profiles relative to the first hard interaction in the calorimeter are investigated.
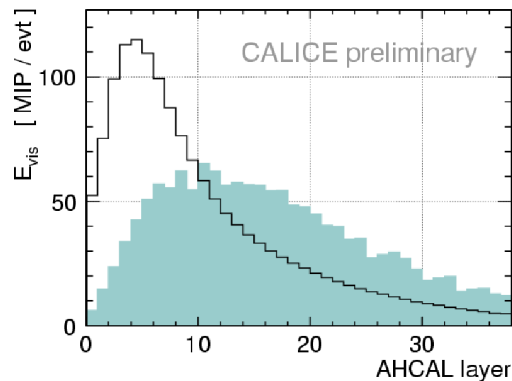

Figure 8.7.: Longitudinal profile of 45 GeV pions measured in the AHCAL relative to the calorimeter front face (filled) and relative to the first hard interaction (black line).

Longitudinal Profiles

Longitudinal profiles from simulations with the LHEP, QGSP_BERT, FTF_BIC, and the CHIPS physics lists measured relative to the first hard interaction are compared

to profiles from pion data in figure 8.8. The ratio between the simulations and the data is plotted in the bottom row. Beam energies of 8, 18, and 80 GeV have been selected in order to investigate the different contributions from the low, medium, and high energy models. The calorimeter depth is expressed in units of nuclear interaction lengths of pions. The black points are measured data which are compared to the simulations shown as filled histograms. The errors shown include the uncertainty of the algorithm to find the shower start and the calibration uncertainty in the data. The decomposition technique described in chapter 7.4 was used to overlay the energy depositions by single particle species in the simulations. This additional information helps to understand which physics processes have the strongest contribution at different stages in the shower development. The sum of the energy deposition from electrons and positrons is highly correlated to the electromagnetic shower fraction (cf. chapter 9) and plotted in red. Protons, negative and positive pions as well as muons from the decay of the latter are comprised as hadrons and their contribution to the visible energy is shown in blue.

At 8 GeV, the LEP model is applied in LHEP. In the first $0.8\lambda_{int}$, it describes the data within the uncertainty and underestimates the deposited energy in the rear of the calorimeter by down to -50%. The Bertini model used by the QGSP_BERT physics lists agrees with the data within the uncertainty and reproduces the shower tail found in data well. The transition between the Binary Cascade and the Fritiof model takes place at $4-5$ GeV in FTF_BIC. The interplay between the two shows a performance similar to the Bertini model with slightly shorter simulated showers. FTF_BIC tends to underestimate the visible energy in the calorimeter after a depth of approximately $1\,\lambda_{int}$. The CHIPS model is in agreement with the data in the first $0.6\,\lambda_{int}$, but predicts too long showers. The energy deposition in the back of the calorimeter is overestimated up to 50%. The high energy deposition in the first calorimeter layer ($0.1\,\lambda_{int}$) is dominated by hadrons in all simulations, while in the range $0.1-1.0\,\lambda_{int}$ the energy deposition is governed by the electromagnetic shower fraction represented by electrons and positrons. After $\sim 1\,\lambda_{int}$ the hadron contribution is again slightly higher than the electromagnetic one. The highest hadron signal is found for the QGSP_BERT physics lists and the lowest for CHIPS. Vice versa, the visible energy deposited by electrons and positron is lowest in the former and highest in the latter. The single contributions in FTF_BIC are very similar to QGSP_BERT, and in LHEP they are in between those of FTF_BIC and CHIPS.

All physics lists are close to data until approximately one λ_{int} after the first hard interaction at 18 GeV beam energy. Bigger differences become visible after this point for CHIPS (up to 30% overestimation) and LHEP (down to 30% too little energy deposition). Data are well described by QGSP_BERT besides slightly too short showers. The performance of FTF_BIC is a little worse but comparable to QGSP_BERT. Too much energy is deposited by CHIPS in the shower maximum and the showers are too long. As expected, at 18 GeV the electromagnetic contribution is higher than at 8 GeV. The highest visible energy from electrons and positrons is

found again in the CHIPS model, where it is even larger than the hadron energy in the first $0.1\,\lambda_{\mathrm{int}}$. The strongest contribution from hadrons after the first interaction is now found in the LHEP and FTF_BIC.

At 80 GeV LHEP simulates the tail of the shower profile quite well, but the energy deposition in the shower maximum is too low by almost 20 %. The other three physics lists overestimate the energy in the shower maximum by $20 - 25$ %. The highest energy deposition is predicted by QGSP_BERT followed by FTF_BIC. Both simulate too short showers. The longitudinal shower shape predicted by CHIPS is closer to the data at this energy. Still, there is too much energy in the shower maximum and the showers are too long. Since the energy deposition in the shower maximum is dominated by electrons and positrons, the overshoot in the energy there predicted by QGSP_BERT, FTF_BIC and CHIPS hints to a too high electromagnetic fraction at 80 GeV.

Shower Centre and Longitudinal Length

The centre of gravity in longitudinal direction is the energy weighted mean of the hit z coordinates relative to the first hard interaction:

$$< z > = \frac{\sum_i E_i \cdot z_i}{\sum_i E_i}. \tag{8.2}$$

It corresponds to the mean value of the longitudinal profiles shown in this section. Their root mean square (RMS) is defined as

$$\sqrt{< z^2 > - < z >^2} = \sqrt{\frac{\sum_i E_i \cdot (z_i - < z >)^2}{\sum_i E_i}}, \tag{8.3}$$

and is a measure for the longitudinal shower length. In order to summarize the performance of the various physics lists in describing the longitudinal shower development, they are compared along these two variables to data over the full energy range of this study.

In figure 8.9(a) the centre of gravity $< z >$ is plotted as a function of the beam energy for simulations and for data. Figures 8.9(b) - 8.9(d) show the ratio between simulations and data, where the differences become more distinct. The grey band comprises the uncertainty from the algorithm to find the shower starting position and the calibration uncertainty. The latter has almost no impact on this variable and is at maximum 1 % at 80 GeV. From 8 to 20 GeV, the FTF model is dominant in the first hard interaction simulated with the QGSP_FTFP_BERT, the FTFP_BERT, FTFP_BERT_TRV, and the FTF_BIC physics lists. All four make similar predictions and underestimate the data by $4 - 5$ %. Up to 20 GeV the QGSP_BERT physics list performs best and describes data within 2 %. This can to be attributed to the combination of the Bertini Cascade with the LEP model which is applied in this energy region. The QGS_BIC model predicts a centre of gravity before $8 - 10$ % the

one found in data in this energy range. Above 20 GeV, the difference between the string models becomes distinct: the QGS model estimates $< z >$ before the data by $\approx 8\,\%$, the FTF model by $\approx 6\,\%$. The CHIPS simulation predicts the centre of gravity to be $10\,\%$ later than in data at 8 and 10 GeV. It comes closer to that of the data with increasing energy, and at 80 GeV, it agrees with data within $1\,\%$. The LHEP physics list behaves the other way round. At 8 GeV, the position of the shower centre is predicted $15\,\%$ before that of the data, and at 80 GeV it is simulated to be $4\,\%$ after it.

Figure 8.10(a) shows the RMS as a function of the beam energy. The ratios between simulation and data are shown in figures 8.10(b) $-$ 8.10(d). As expected, the systematic error of the algorithm to find the first hard interaction cancels almost completely. The picture is consistent to what was observed in figure 8.8. The CHIPS model is the only one which overestimates the longitudinal shower extension by $1 - 7\%$. The LEP model in combination with the Bertini cascade in the QGSP_BERT physics lists below 20 GeV agrees within $2\,\%$ with the data. The FTF and QGS model behave quite similar and both predict a $\approx 4\%$ too short shower extension compared to the data. However, QGS in combination with the Binary cascade simulates shorter showers by $6 - 10\,\%$. No big difference between the Fritiof physics lists is visible, they agree within $1\,\%$ with each other and describe the data within $5\,\%$ at all energies. The shower length of LHEP relative to the one observed in data is $15\,\%$ too short at 8 GeV and grows with energy. At 80 GeV it agrees with data within $1\,\%$.
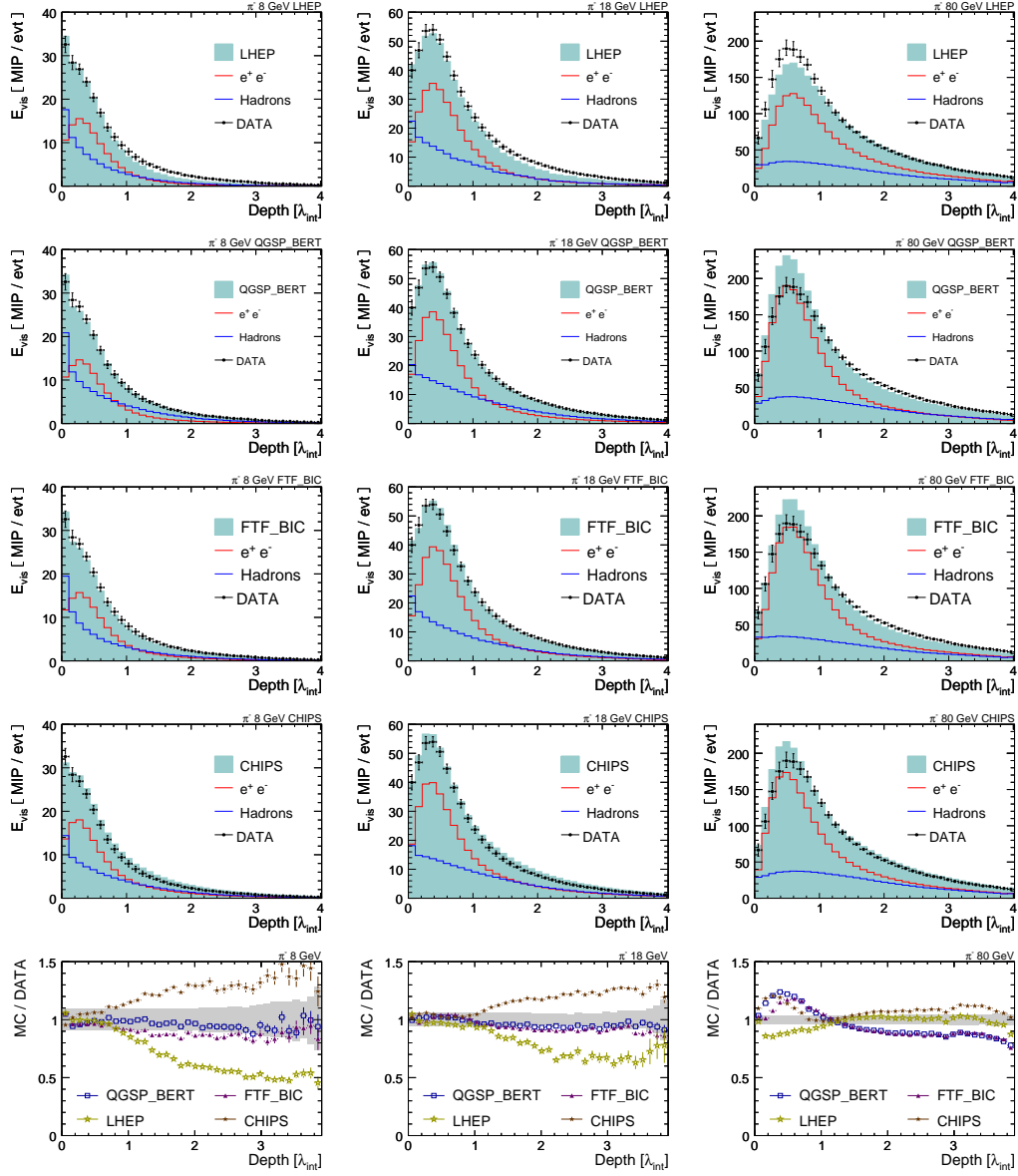
Figure 8.8.: Longitudinal shower profiles relative to the first hard interaction for 8, 18, and 80 GeV pions. The ratio between simulated and measured longitudinal profiles is shown in the bottom row. The error bars comprise the statistical error as well as the uncertainty introduced by the algorithm and the uncertainty from the calibration.

(a)

(b)

(c)

(d)

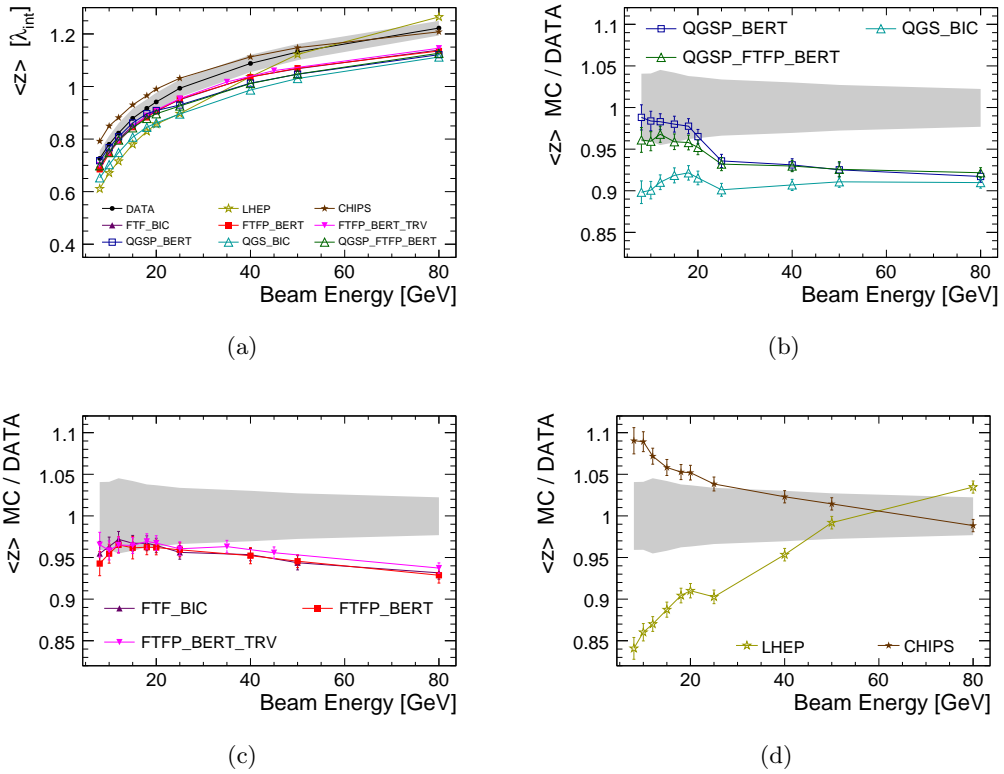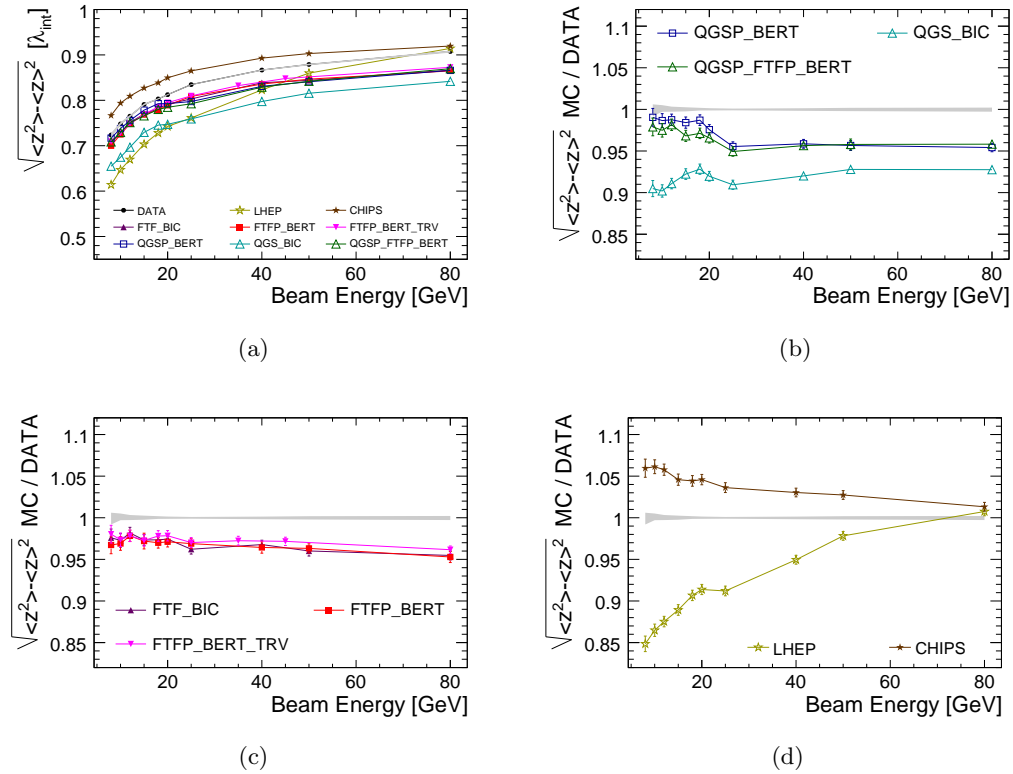Figure 8.9.: Centre of gravity in longitudinal direction as a function of the beam energy.

Figure 8.10.: The root mean square of the longitudinal profiles as a function of the beam energy. The grey band comprises the uncertainty of the algorithm and the calibration. In this variable the uncertainty of the algorithm cancels almost completely

Transverse Shower Development

In this part, the highly granular segmentation of the AHCAL layers is exploited to study the transverse shower development. For each AHCAL cell i, the radial distance to the incoming particle track is determined as:

$$r_i = \sqrt{(x_i - x_0)^2 + (y_i - y_0)^2} \qquad (8.4)$$

where (x_i, y_i) is the coordinate of the cell centre and (x_0, y_0) is the position of the energy weighted shower centre:

$$x_0 = \frac{\sum_i E_i \cdot x_i}{\sum_i E_i} \quad \text{and} \quad y_0 = \frac{\sum_i E_i \cdot y_i}{\sum_i E_i}. \qquad (8.5)$$

The transverse profiles in figure 8.11 show the average energy deposited in the calorimeter as a function of the distance r to the incoming track for pion showers at beam energies of 8, 18, and 80 GeV. The filled histograms are simulations with the same set of physics lists already presented before in this chapter for the longitudinal direction. The measured data are overlaid as black points. In the bottom row, the ratios between the simulations and the measured data are shown. The grey error band indicates the uncertainty from the calibration. As for the longitudinal profiles, the simulated contributions from the electromagnetic and the hadron shower components are overlaid. In the following, the simulations are compared to the measured data at the three different energies.

At 8 GeV, the QGSP_BERT describes data within 4 % in the range of $0 - 40$ mm and underestimates the deposited energy down to 10 % for larger distances. The FTF_BIC physics list behaves quite similar: it shows agreement with the data within 5% in the range $0 - 40$ mm and predicts down to 15 % too low visible energy at distances larger than 40 mm. The CHIPS physics list overestimates the energy deposited in the shower core by almost 20 % and agrees with the data for radii larger than 60 mm. The LHEP physics lists overestimates the energy deposited in the shower core by more than 20 %, crosses the data at 40 mm and simulates an almost 40% to low energy at 200 mm distance from the shower centre.

At 18 GeV, only little differences between the QGSP_BERT, FTF_BIC, and LHEP physics list are observable in the range $r = 0 - 30$ mm. They predict $12 - 15$ % too much energy closest to the shower centre, and predict the same amount of energy as in data at 30 mm. After this point, differences between them become visible: FTF_BIC predicts an $8 - 11$ % to low energy, QGSP_BERT is too low by roughly 14 %, and LHEP goes down to 35 % too little visible energy. The CHIPS physics list shows a different picture: it agrees with data up to 30 mm and overestimates the deposited energy at larger distances up to 9 %.

At 80 GeV, the cell structure of the calorimeter becomes visible because of the narrower beam spread at this energy. One can clearly see groups of three bins which correspond to the cell size of 30 mm in the fine core of the AHCAL. In the cells closest

to the shower centre, QGSP_BERT simulates a 20 % too high energy deposition and at larger distances the underestimation is roughly 15 %. The FTF_BIC physics list shows similar behaviour but is closer to data by $1-5\,\%$. The HEP model is dominant at this energy in the LHEP physics lists which is closer to data in the shower core. The jump at $r = 30$ mm is a binning effect. At larger distances, LHEP still underestimates the data by down to 27 %. At this higher energy, the CHIPS physics list is close to data at low distances to the shower centre and overestimates the visible energy by up to 15%

Hadronic showers in general have a narrow electromagnetic core, while the energy deposition by hadrons can spread wide in the calorimeter. The reason for this is that the energy necessary for the creation of π_0 particles is only available close to the initial hard interaction point. The electromagnetic component stems almost only from the decay $\pi_0 \rightarrow \gamma\gamma$ which occurs almost instantly after the π_0 is created, and thus close to the shower axis. In the overlaid simulated electromagnetic and hadronic contributions, it is observed that QGSP_BERT has the narrowest electromagnetic core at all energies. The hadronic contribution becomes dominant after 40 mm at 8 GeV and after 90 mm at 80 GeV. In LHEP the electromagnetic core is wider and stronger than the hadronic contribution until 70 mm from the shower axis at 8 GeV and until 110 mm at 80 GeV. CHIPS simulates the widest electromagnetic core of all models which is the reason for the overestimation of the tails. Comparison with the shape of the transverse energy distribution in data at 8 GeV suggests that the Bertini model simulates the shower composition better than the combinations the Binary cascade and the Fritiof model. At higher energies, the Fritiof model is closer to data than QGSP_BERT. In general a too short transverse shower extension is predicted by LHEP which can be attribution to a too low hadronic contribution in the tails.

Mean Shower Radius

In the figure 8.11, four different simulations have been compared in the range 0- -200 mm from the first interaction in transverse direction. In the following, the simulations are compared to data along the energy weighted mean shower radius $< r >$ averaged over the full calorimeter. It is defined as

$$< r > = \frac{\sum_i E_i r_i}{\sum_i E_i} \qquad (8.6)$$

and is shown as function of the beam energy for all tested physics lists in figure 8.12. The calibration uncertainty shown is below 1 % at all energies.

The observed shower radii become narrower with increasing energy in both data and simulations. All simulations underestimate the mean shower radius at all energies, except for CHIPS which is the only model that agrees with the data at 80 GeV. Above 20 GeV, the CHIPS model differs only by 5 % from data. The QGSP_BERT and QGSP_FTFP_BERT model underestimate the mean shower radius by 12 %. At

lower energies, the combination of the Bertini and the LEP model in QGSP_BERT is slightly closer to the data then the combination of the Bertini and the Fritiof model in QGSP_FTFP_BERT. The QGS_BIC model simulates roughly $16 - 20\%$ too small shower radii. Compared to the FTFP_BERT_TRV and FTFP_BERT models, the FTF_BIC is closer to data and simulates an approximately 10% too small mean shower radius, whereas the former predicts a 12% too low value. The LHEP physics list underestimates the data by 26% at $8\,\mathrm{GeV}$. With growing energy it comes closer to the data, but still shows a 14% to low shower radius at $80\,\mathrm{GeV}$.

Transverse Shower Extension

The root mean square of the energy weighted shower radius

$$\sqrt{<r^2> - <r>^2} = \sqrt{\frac{\sum_i E_i\,(r_i - <r>)^2}{\sum_i E_i}} \tag{8.7}$$

is another quantification of the transverse shower extension. It is plotted in figure 8.13 as a function of the beam energy. Also for this variable, all physics lists underestimate the shower extension found in data. For CHIPS, this is no contradiction to the larger transverse shower extension compared to the data which is shown in figure 8.11, since there only the narrow range of $r = 0 - 200\,\mathrm{mm}$ is investigated. Above $18\,\mathrm{GeV}$, the FTF_BIC physics list is closest to the data and agrees within 4%. The FTFP_BERT list and its variation FTFP_BERT_TRV underestimate the data by 6% in this range. The QGS_BERT and QGSP_BERT show the same behaviour and underestimate the shower extension by approximately 6% compared to data. The application of the Binary cascade instead of the Bertini model in QGS_BIC results in 10% narrower showers than in data. The underestimation of the data by LHEP is 16% at $8\,\mathrm{GeV}$ and 10% at $80\,\mathrm{GeV}$.

8.6. Summary

In this chapter, hadronic showers recorded at CERN in 2007 from negative pions have been investigated along several variables. This data set has been chosen, since the data acquisition environment and the beam quality at CERN were already analysed in other studies [39, 77, 40, 42] and are better understood than those at Fermilab. In addition, the modelling in the simulation is the most advanced for the CERN setup and beam line instrumentation. Eight physics lists are studied, which are currently in discussion in the ongoing development of the Geant 4 simulation software. Apart from validation with thin target data [78], the CALICE test beam data are a valuable source to investigate the strengths and weaknesses of the hadronic models. The performance of the simulations with the several physics lists in describing the AHCAL data is summarized in this section. An overview is given in table 8.3.

Throughout this analysis the Primary Track Finder algorithm was used in the event selection and for the measurement of the hadronic interaction length. Its performance in finding the position of the first hard interaction was investigated and improved in the framework of this thesis. The mean difference between the true shower starting position in simulations and the one found by the algorithm could be reduced to value below one AHCAL layer. In addition, the energy dependence of its performance was reduced in the refinement of the algorithm. However, there is still room for improvement. The uncertainty to detect the correct shower starting position in a single event can still be minimized until the natural limit of one AHCAL layer is reached. Furthermore, the capability to find the correct shower starting position still depends on the physics lists used which is taken into account in the estimation of the uncertainties presented throughout this study. An approach to improve the algorithm could be to additionally include the transverse calorimeter information and the use of energy dependent parametrizations for all applied thresholds.

The effective hadronic interaction length λ_{int} has been measured using the information on the position of the first hard interaction in the AHCAL. This is a consistency check of the validity of the algorithm and yields the same effective nuclear interaction length within the uncertainty for all physics lists besides CHIPS and LHEP. The different interaction lengths found for CHIPS and LHEP are no surprise, since both are known to use different cross sections than the Fritiof and QGS physics lists. For data, an effective hadronic interaction length of $\lambda_{\mathrm{int}} = 29 \pm 1\,\mathrm{cm}$ was measured which is compatible with the expected value of $28.1\,\mathrm{cm}$ [30] and is consistent with the majority of the simulations.

All physics lists but CHIPS show an energy dependent performance in describing the visible energy E_{vis} in the calorimeter compared to the data. One can clearly see the transition between the models the physics lists are composed of. This unwanted behaviour is most distinct in the QGS physics lists which tend to underestimate the calorimeter response at lower particle energies and to slightly overestimate it at higher energies. A smoother transition between the models is observed for the Fritiof lists which also agree better with the data. The LHEP model predicts a too low energy deposition and does not describe what is observed in the data. The restriction on the showers to start in the front of the AHCAL in the event selection reduces the amount of leakage which has an impact on the mean visible energy in the calorimeter. No further effort is made to correct for the leakage still present after applying this cut. The differences between data and simulation might partially be due to the different amount of leakage. However, the observed behaviour of the simulations compared to data are in agreement with other studies using a different set of data and applying correction for leakage [42].

The longitudinal and transverse shower development has been investigated. All QGS and FTF physics lists predict the centre of gravity in longitudinal direction before that observed in data and shorter showers than in data. The same holds true for the LHEP physics list except for the $80\,\mathrm{GeV}$ showers where the HEP model is most

dominant. Too long showers and a centre of gravity too late in the calorimeter is found with the CHIPS physics list. In transverse direction all simulations are too narrow compared to data.

Four different simulations have been compared at low, medium, and high energies along high-resolution longitudinal profiles relative to the first hard interaction. The too low visible energy compared to data predicted by the LHEP physics list is missing in the tails of the longitudinal profiles when only the LEP model is applied (8 and 18 GeV) and in the shower maximum at 80 GeV where HEP is dominant. For CHIPS the excess in the visible energies shows up in the tails at 8 and 18 GeV, and for 80 GeV in addition in the shower maximum. The QGSP_BERT and the FTF_BIC physics lists describe the longitudinal shower shape relatively well at 8 and 18 GeV, but exceed the shower maximum found in data at 80 GeV. In the transverse profiles extracted for the same physics lists and beam energies in the core of the shower ($r = 0 - 200 \, \text{mm}$), one observes too narrow showers compared to data for all simulations but CHIPS which predicts too wide showers in the core.

The decomposition of the deposited energy into the contribution from single particle species shows where the hadronic and electromagnetic shower components are most dominant. While the influence of hadronic energy deposition in longitudinal direction is strongest after the first hard interaction and in the shower tails, the shower maximum is dominated by the electromagnetic component. In transverse direction, this component governs in the core and the hadronic component has impact on the tails. Future steps in this analysis would be to use this information to model the shape of the single contributions and develop a method to extract the fraction of electromagnetic and hadronic energy deposition from the data. The transverse and longitudinal information can be combined to select areas in which the contribution of the different components becomes most distinct. An approach could be to study transverse shower profiles restricted to layers around the shower maximum where the electromagnetic component is most dominant.

	QGSP_BERT	QGSP_FTFP_BERT	QGSP_BIC	FTFP_BERT	FTFP_BERT_TRV	FTF_BIC	CHIPS	LHEP
λ_{int}	⊕	⊕	⊕	⊕	⊕	⊕	⊙⊙	⊙
E_{vis}	⊕	⊕	⊙⊙	⊕	⊕	⊕	⊙⊙	⊙⊙
Long. Prof. 8 GeV	⊕⊕					⊙	⊖⊖	⊖⊖
Long Prof. 18 GeV	⊕					⊙	⊖⊖	⊖⊖
Long Prof. 80 GeV	⊖⊖					⊖	⊖	⊖
$<z>\ E = 8 - 20\,\mathrm{GeV}$	⊕⊕	⊕	⊙⊙	⊕⊕	⊕⊕	⊕⊕	⊙⊙	⊙
$<z>$ above 20 GeV	⊙⊙	⊙⊙	⊙⊙	⊙⊙	⊙⊙	⊙⊙	⊕⊕	⊙⊙
$<z>_{\mathrm{RMS}}\ E = 8 - 20\,\mathrm{GeV}$	⊕	⊕	⊙⊙	⊕	⊕	⊕	⊙⊙	⊙
$<z>_{\mathrm{RMS}}$ above 20 GeV	⊕	⊕	⊙⊙	⊕	⊕	⊕	⊕	⊙⊙
Trans. Prof. 8 GeV	⊙⊙					⊙	⊖	⊖⊖
Trans. Prof. 18 GeV	⊙					⊙⊙	⊙⊙	⊖⊖
Trans. Prof. 80 GeV	⊖					⊙	⊙	⊖⊖
$<r>\ E = 8 - 20\,\mathrm{GeV}$	⊙⊙	⊙	⊖	⊙	⊙	⊙	⊙	⊖⊖
$<r>$ above 20 GeV	⊙	⊙	⊖	⊙	⊙	⊙⊙	⊕	⊖
$<r>_{\mathrm{RMS}}\ E = 8 - 20\,\mathrm{GeV}$	⊕	⊕	⊙⊙	⊙⊙	⊙⊙	⊙⊙	⊙	⊖
$<r>_{\mathrm{RMS}}$ above 20 GeV	⊕	⊕	⊙⊙	⊕	⊕	⊕	⊕	⊙

Table 8.3.: Summary of the performance of the single physics lists in describing the data.

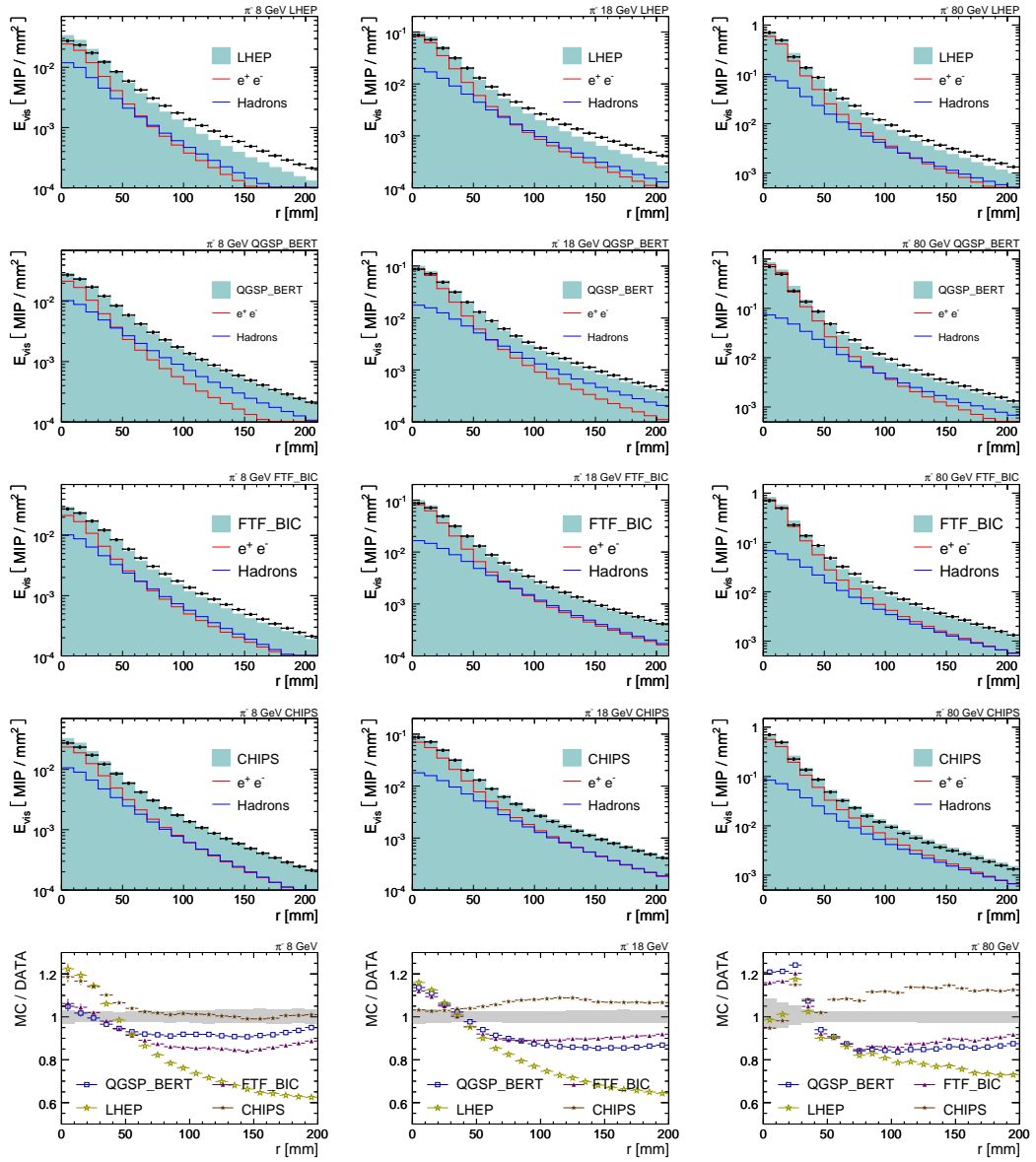|			
⊕⊕	within uncertainty,	⊕	within $\approx 5\,\%$
⊙⊙	within $\approx 10\,\%$,	⊙	within $\approx 15\,\%$
⊖	within $\approx 20\,\%$,	⊖⊖	$> 20\,\%$.

Figure 8.11.: Transverse shower profile for 8, 18 and 80 GeV pions simulated with the QGSP_BERT, FTF_BIC, LHEP and the CHIPS physics lists. The bottom row shows the ratio between simulations and data.
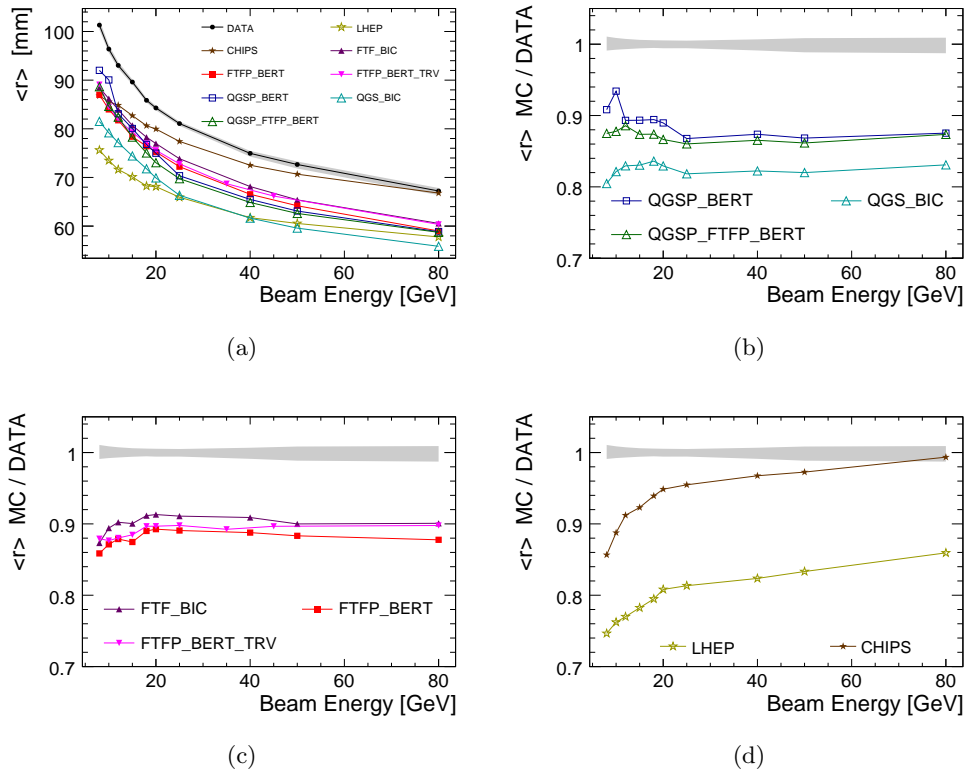
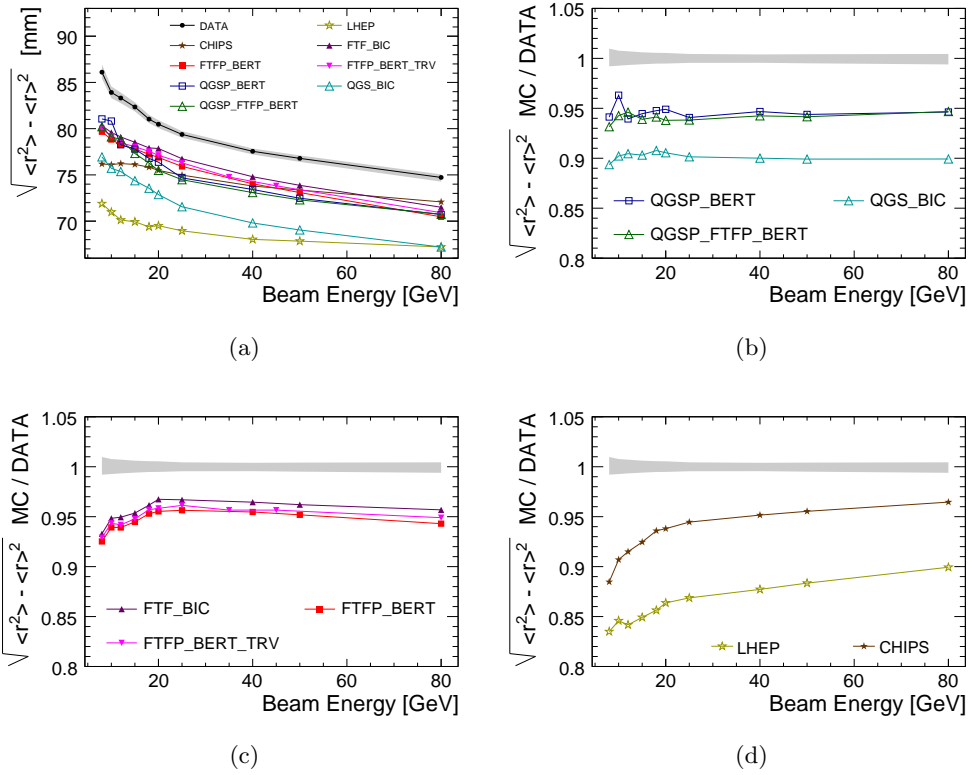Figure 8.12.: The energy weighted mean as a function of the beam energy.

(a)

(b)

(c)

(d)

Figure 8.13.: The root mean square of the energy weighted shower radius as a function of the beam energy.

9. The Electromagnetic Fraction

In general, hadron showers contain a component originating from electromagnetically decaying particles with a characteristically higher energy density compared to the rest of the shower. As mentioned in chapter 2, the fluctuation in the electromagnetic shower component is one of the main reasons for the poor energy resolution of non-compensating hadronic calorimeters. An event wise measurement of the electromagnetic component allows to apply a different weight for this component in the energy reconstruction. This can significantly improve the resolution of the hadron energy measurements [79, 80, 81].

In the AHCAL, the distribution of the energy in the shower volume can be investigated with an unprecedented granularity. In this chapter, the attempt to access the electromagnetic fraction in hadron showers using the high resolution energy density measurement is presented. An ad-hoc clustering algorithm is applied to the data which classifies shower components by their energy density. In the first section, the information on the shower composition from the simulations is briefly discussed. These informations have been used to tune the parameters of the algorithm and to reduce the energy dependence of its performance which is discussed in the second section.

9.1. Information Available in the Simulations

The major contribution to the electromagnetic component in hadron showers is from the decay of π^0 and η particles [3]. For this analysis, a plugin for the Mokka simulation software has been developed that tracks the total energy of all π^0 decaying in the detector as well as the total energy of all photons emerging from the η decay. In the following, this energy will be referred to as $E_{\pi^0\eta}$. The true electromagnetic shower fraction is defined as the ratio between the electromagnetic energy $E_{\pi^0\eta}$ and the energy E_{beam} of the primary particle:

$$f_{\text{EM}} = \frac{E_{\pi^0\eta}[\text{GeV}]}{E_{\text{beam}}[\text{GeV}]}. \tag{9.1}$$

Figure 9.1 shows f_{EM} as a function of the beam energy for copper (circles) [3], for the scintillator steel ATLAS Barrel Tile HCAL prototype [82] (dashed line) and for the AHCAL prototype simulated with the FTFP_BERT physics lists (squares). Both curves from the literature follow the parametrization described in equation 2.12 with the values $E_0 = 0.72\,\text{GeV}$ and $k = 0.82$ for copper and $E_0 = 1.00\,\text{GeV}$ and $k = 0.85$

for the ATLAS calorimeter. The fit of parametrization through to the simulated AHCAL points yields $E_0 = (1.17 \pm 0.01)\,\text{GeV}$ and $k = 0.831 \pm 0.001$.
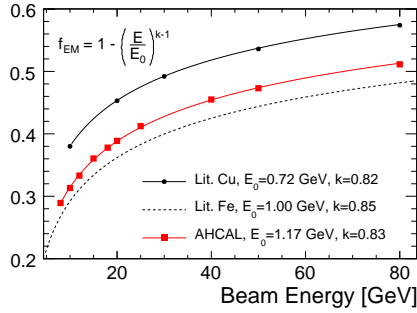

Figure 9.1.: Electromagnetic fraction for hadronic showers in copper [3] and simulated with the FTFP_BERT physics list in the AHCAL.

The variables $E_{\pi^0\eta}$ and f_{EM} are of course only available in the simulations using the Mokka plugin. For the test beam data, it is tried to measure these quantities applying the clustering algorithm described in the next section.

9.2. The Deep Analysis Clustering Algorithm

The Deep Analysis Algorithm was originally developed by V. Morgunov [83] and was later ported to the CALICE analysis framework. It is an ad-hoc clustering algorithm based on the analogue energy density information and it allows to study the composition of hadronic showers in highly granular calorimeters. The Deep Analysis Algorithm was first applied to AHCAL data in [39], where also detailed studies have been performed on data to Monte Carlo simulation comparison. However, there the analysis is performed with data from an only partly equipped AHCAL and beam energies in the range $6 - 20\,\text{GeV}$. In this analysis, the algorithm is applied to the pion data and the corresponding simulations in the range $8 - 80\,\text{GeV}$ which have already been presented in chapter 8 using the same event selection discussed there.

Working Principle

The concept of the algorithm is to separate a hadronic shower in four contributions: tracks, the hadronic fraction, the electromagnetic fraction, and neutrons. Clusters of hits, i.e. cells with a signal above the 0.5 MIP noise threshold, are found in several steps. Here, only a brief summary of how the algorithm works is given. A more detailed description can be found in [84].

In the first step, all hits are sorted according to their energy and assigned to one of the four contribution types named above without regarding their geometrical position in

the detector. Figure 9.2 shows the energy spectrum of single hits from simulations and an example of energy cuts to identify their type. In the implementation of the algorithm applied to the AHCAL data, hits with energies from $0.5 - 1.7\,\text{MIP}$ are identified to be track like. Hits in the range $1.7 - 3.7\,\text{MIP}$ are tagged hadron-like and hits above $3.7\,\text{MIP}$ are assigned to the electromagnetic fraction.

As the second step, a two-dimensional clustering is performed in each calorimeter layer. Afterwards, the three-dimensional distances between the two-dimensional clusters in the full calorimeter are calculated. Clusters are joined to a three dimensional object, if their distance is below a certain threshold.

The clustering step is performed first on the electromagnetic-like hit collections. After the clusters have been found, an additional step is applied for the electromagnetic-like component. Around each electromagnetic-like cluster an ellipsoid is built, defined by three parameters: a transverse, a backward, and a forward radius. All additional hits included in the ellipsoid are added to the electromagnetic-like cluster and removed from track-like or hadron-like hits collections.

The clustering step is then performed on the track-like and the hadronic-like hit collections without the ellipsoid step. All separate left over hits, i.e. hits without neighbours that were not joined into clusters, are classified as neutron-like hits.
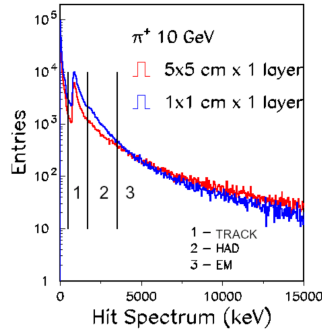

Figure 9.2.: Hit classification by energy in the Deep Analysis algorithm. Picture taken from [84].

Performance

Only the sum of energy E_{EC} deposited in the electromagnetic-like clusters identified by the algorithm is studied here. In order test the performance of the algorithm, E_{EC} is compared to the real electromagnetic component $E_{\pi^0 \eta}$ in the Monte Carlo simulations introduced before. The algorithm returns E_{EC} in units of MIP. For the comparison it is necessary to convert E_{EC} to the GeV scale, which is done with the energy scaling factor $w_{\text{MC}} = 41.9\,\text{MIP/GeV}$ obtained from positron data in 6.4. Figure 9.3(a) shows the correlation between E_{EC} and $E_{\pi^0 \eta}$ for simulated $80\,\text{GeV}\ \pi^-$ showers. Beside the good correlation between the two, one can recognize a second

type of events with high energy deposition in the electromagnetic-like clusters. In figure 9.3(b), the correlation between the energy

$$E_{3.7} = \sum_{E_i > 3.7\,\mathrm{MIP}} E_i \tag{9.2}$$

deposited in calorimeter hits with an energy above 3.7 MIP and $E_{\pi^0\eta}$ is plotted for the same set of events. There, no such events are visible which proves that the artefact is introduced by the clustering algorithm. The too high energy deposition in electromagnetic like clusters was identified to occur in events where the algorithm assigns all found clusters to be electromagnetic. This can be seen in figure 9.3(c) where the total number of clusters (red) is overlaid to number of electromagnetic like clusters found (blue). In a fraction of roughly 16 % of the events, the number of total clusters found is equal to number of electromagnetic-like clusters. It is assumed that the reason for this behaviour is a failure of the mechanism which collects additional hits in the ellipsoid surrounding the electromagnetic like clusters in case of very compact showers [85]. A variable adaption of the parameters defining the ellipsoid size might solve this problem. The effect is currently under investigation and an improvement of the algorithm is foreseen as future work.

In the following discussion, all events where the clustering algorithm fails are ignored, i.e. all events where all clusters are found to be electromagnetic or no electromagnetic clusters are found at all. Regarding $E_{\pi^0\eta}$, one can clearly see that the events which are removed would shift its mean to higher values. It has to be stated clearly at this point that all results concerning the electromagnetic shower component shown in the following are shifted systematically to lower values due to this cut.

Uncertainty

The aim of this study is to compare the fraction of energy deposited in electromagnetic-like clusters

$$f_{\mathrm{EC}} = \frac{E_{\mathrm{EC}}\,[\mathrm{GeV}]}{E_{\mathrm{beam}}\,[\mathrm{GeV}]} \tag{9.3}$$

identified by the algorithm between simulations and data. To be able to do this comparison, the uncertainty of the algorithm has to be estimated first. This is done by comparing f_{EC} to the true electromagnetic fraction f_{EM} in the simulations. Figure 9.4(a) shows a correlation of roughly 83 % between the two for 80 GeV pions simulated with the FTFP_BERT physics list. The distribution of the difference $\Delta = f_{\mathrm{EC}} - f_{\mathrm{EM}}$ is plotted in figure 9.4(b) and has a mean value of $-1.7\,\%$ with and a RMS of 8.9 %.

In the version of the algorithm implemented into the official CALICE reconstruction software at the time this study was done, the threshold for the identification of electromagnetic hits was fixed to 3.7 MIP. In the framework of this thesis, the software was modified with the aim to improve the performance of the algorithm in detecting the fraction of energy deposition by electrons and positrons. An energy dependent
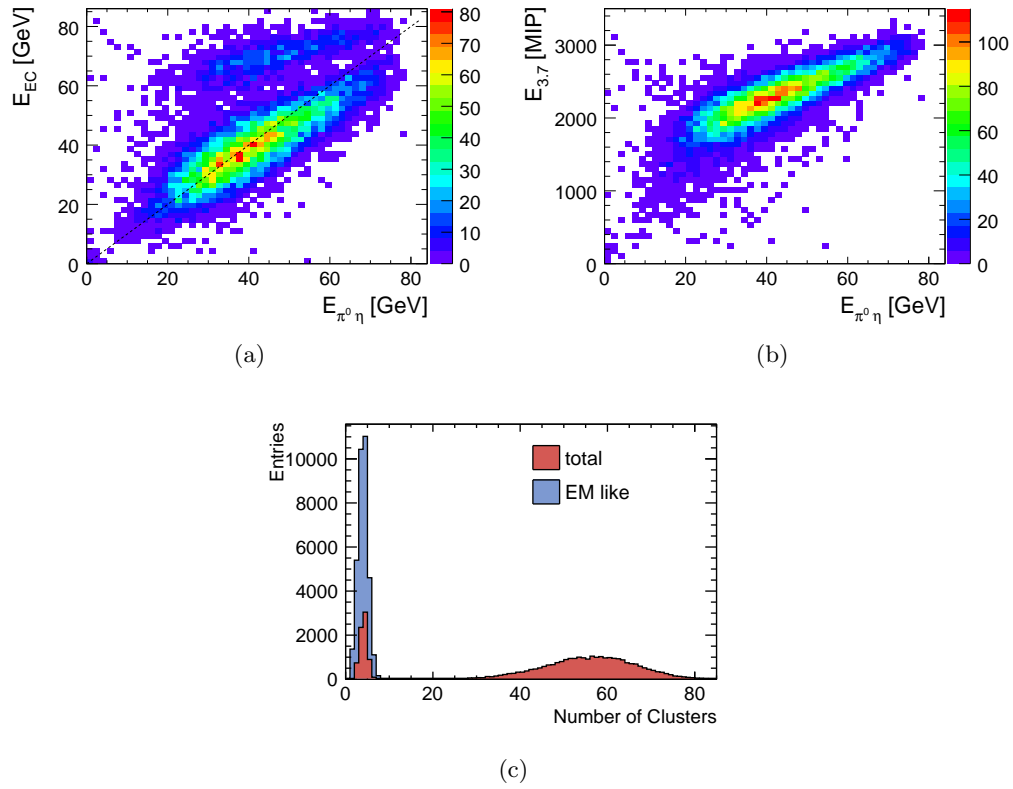
(a)

(b)

(c)

Figure 9.3.: (a) Correlation between E_{EM} and $E_{\pi^0\eta}$ for simulated $80\,\mathrm{GeV}$ π^- showers. (b) Correlation between the energy $E_{3.7}$ deposited in calorimeter hits with an energy above 3.7 MIP and $E_{\pi^0\eta}$ for the same set of events. (c) Number of clusters found by the algorithm.
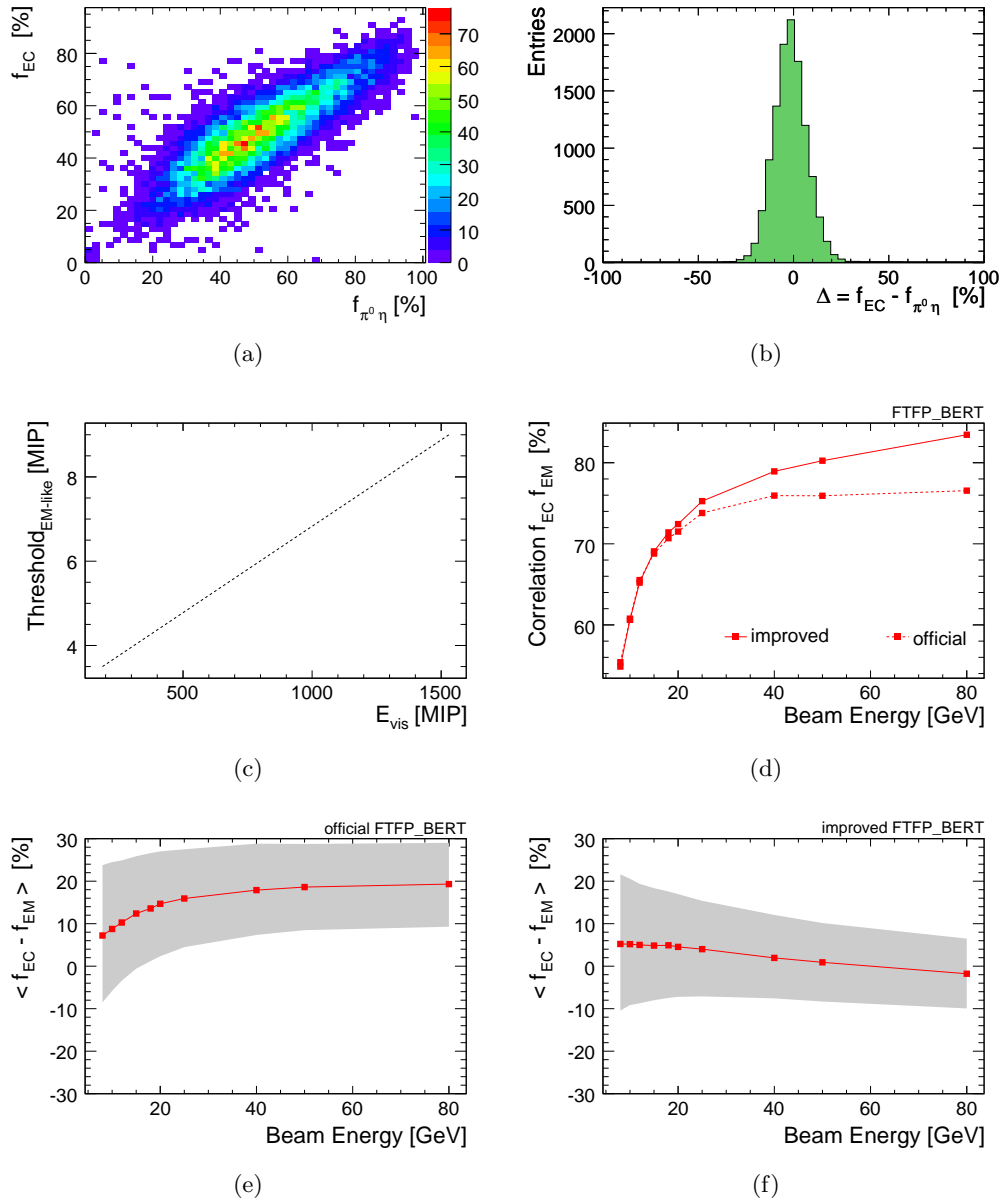
(a)

(b)

(c)

(d)

(e)

(f)

Figure 9.4.: Correlation (a) and difference(b) between the fraction of visible energy deposited in electromagnetic like clusters f_{EC} and the electromagnetic fraction f_{EM} after the refinement of the energy threshold. (c) Energy dependent parametrization of the threshold to identify hits a electromagnetic like. (d) The Correlation as a function of beam energy before (dashed line) and after (solid line) the application of the parametrization. Mean difference between f_{EC} and f_{EM} as a function of the beam energy before (e) and after (f) the refinement of the algorithm.

parametrization for the threshold to identify the electromagnetic-like hits has been implemented and optimized for this analysis. Since the beam energy is only available in test beam setups, it is not used and the thresholds are applied according to the sum of energy deposited in the calorimeter prototype. Figure 9.4(c) shows the parametrization of the threshold as a function of the energy. The parametrization was optimized using the FTFP_BERT physics list. The correlation of f_{EC} and f_{EM} as a function of the beam energy for simulations with the FTFP_BERT physics lists is shown in figure 9.4(d). While the modification of the algorithm does not change the correlation in the lower energy range, above $18\,\text{GeV}$ an improvement between $2 - 8\,\%$ is visible. After the attempt to enhance the performance of the algorithm, there is still almost no correlation at lower energies and only a correlation of $83\,\%$ at $80\,\text{GeV}$.

The average difference $<\Delta>=< f_{\text{EC}} - f_{\text{EM}} >$ before and after the implementation of the dynamic threshold is compared in figures 9.4(e) and 9.4(f). The grey band indicates the range which holds $66\,\%$ of the events in the distribution of Δ. The width of this range is a measure for the event-wise uncertainty of the method which varies from roughly $\pm15\,\%$ at $8\,\text{GeV}$ to roughly $\pm8\,\%$ at $80\,\text{GeV}$ after the improvement. In the official version with the fixed threshold of the algorithm, $<\Delta>$ grows from $7\,\%$ at the lowest energy point to $20\,\%$ at the highest energy point. After the modification, there is a negative energy dependence and $<\Delta>$ varies from $5\,\%$ at $8\,\text{GeV}$ to $-2\,\%$ at $80\,\text{GeV}$. Such a shift could be easily corrected for; it is however strongly dependent on the physics lists used for the simulation which can be seen in appendix C where the performance of the algorithm applied to simulations with the other physics lists is presented.

Results

Due to energy dependent shift between f_{EC} and f_{EM}, the fraction of events where the algorithm fails, and the strong dependence on the physics lists used, the algorithm with the parameters applied here cannot be used to measure the electromagnetic fraction. Nevertheless, the results obtained are shown in figure 9.5 to discuss the performance of the algorithm.

Figures 9.5(a), 9.5(c), and 9.5(e) show the fraction of energy f_{EC} deposited in electromagnetic like clusters found by the algorithm for the several physics lists and for data. The grey band attached to the data points is the uncertainty of the algorithm estimated from RMS of the difference between f_{EC} and f_{EM}. Below $15\,\text{GeV}$, where the correlation between f_{EC} and f_{EM} is worst (cf. figure 9.4(d) and appendix C), all physics lists agree with the data within the uncertainty. Above $15\,\text{GeV}$, the algorithm finds a higher f_{EC} in the simulations with the QGS and Fritiof physics lists than in data.

Regarding the data one can clearly see, that the presented variable f_{EC} cannot be the real electromagnetic fraction, because the value does not increase above $40\,\text{GeV}$ and even decreases at $80\,\text{GeV}$. A similar behaviour is observed for the LHEP and

CHIPS physics lists. The reason for this is shown in figures 9.5(b), 9.5(d), and 9.5(f) where the differences between f_{EC} and the real electromagnetic fraction f_{EM} in the simulations are plotted. For all physics lists f_{EC} is too high at smaller energies and too low at larger beam energies compared to f_{EM}, except for CHIPS where f_{EM} is too low at all energies (cf. figure 9.4(f) and appendix C). This behaviour can be changed by adjusting the parameters of the algorithm as shown before in this chapter and is subject to future steps in this study.

Despite the fact that the f_{EC} cannot be taken as a measure for the real electromagnetic fraction, it is interesting that the algorithm reacts in a similar way to data and to the simulations with the CHIPS physics list. At beam energies above $20\,\text{GeV}$, the two agree within $2\,\%$. This could be a hint to a better matching description of the energy deposition in the AHCAL by CHIPS compared to the other physics lists. It is consistent with the observation that the description of the energy density ρ is closest to data for simulations with the CHIPS physics list. The energy density is defined as the ratio between the sum of the total reconstructed energy in the AHCAL E_{vis} and the number of active cells N_{hit}:

$$\rho = \frac{E_{vis}[\text{MIP}]}{N_{hit}}. \tag{9.4}$$

The distribution of ρ is plotted for simulations of $80\,\text{GeV}$ pions with the QGSP_BERT, FTF_BIC and CHIPS physics lists in the filled histograms in figures 9.6(a), 9.6(b), and 9.6(c) respectively. The data are overlaid black circles. The mean values of these histograms as a function of the beam energy is shown in figure 9.6(d) for all physics lists. In this variable the CHIPS simulation is closest to data at all energies. Above $15\,\text{GeV}$, the two agree within the calibration uncertainty.

Summary

In this chapter, a clustering algorithm is applied to the highly granular AHCAL data with the aim to access the electromagnetic component in pion showers. The performance of the algorithm is evaluated by comparing the amount of energy deposited in electromagnetic like clusters to the true electromagnetic component of the showers in simulations. The uncertainty of the algorithm to determine the electromagnetic fraction f_{EM} ranges from roughly $\pm 15\,\%$ at $8\,\text{GeV}$ to $\pm 8\,\%$ at $80\,\text{GeV}$. However, a physics lists and energy dependent systematic shift between the electromagnetic like-fraction f_{EC} found by the algorithm and the true f_{EM} is observed which is positive at lower energies and negative at higher energies. Nevertheless, it has been shown that its performance can be enhanced by adjustment of the parameters and additional tuning will further improve its potential to access the electromagnetic fraction. Future studies will use the information to apply different weights to the electromagnetic and hadronic shower components in order to compensate the different calorimeter response which will improve the energy resolution.
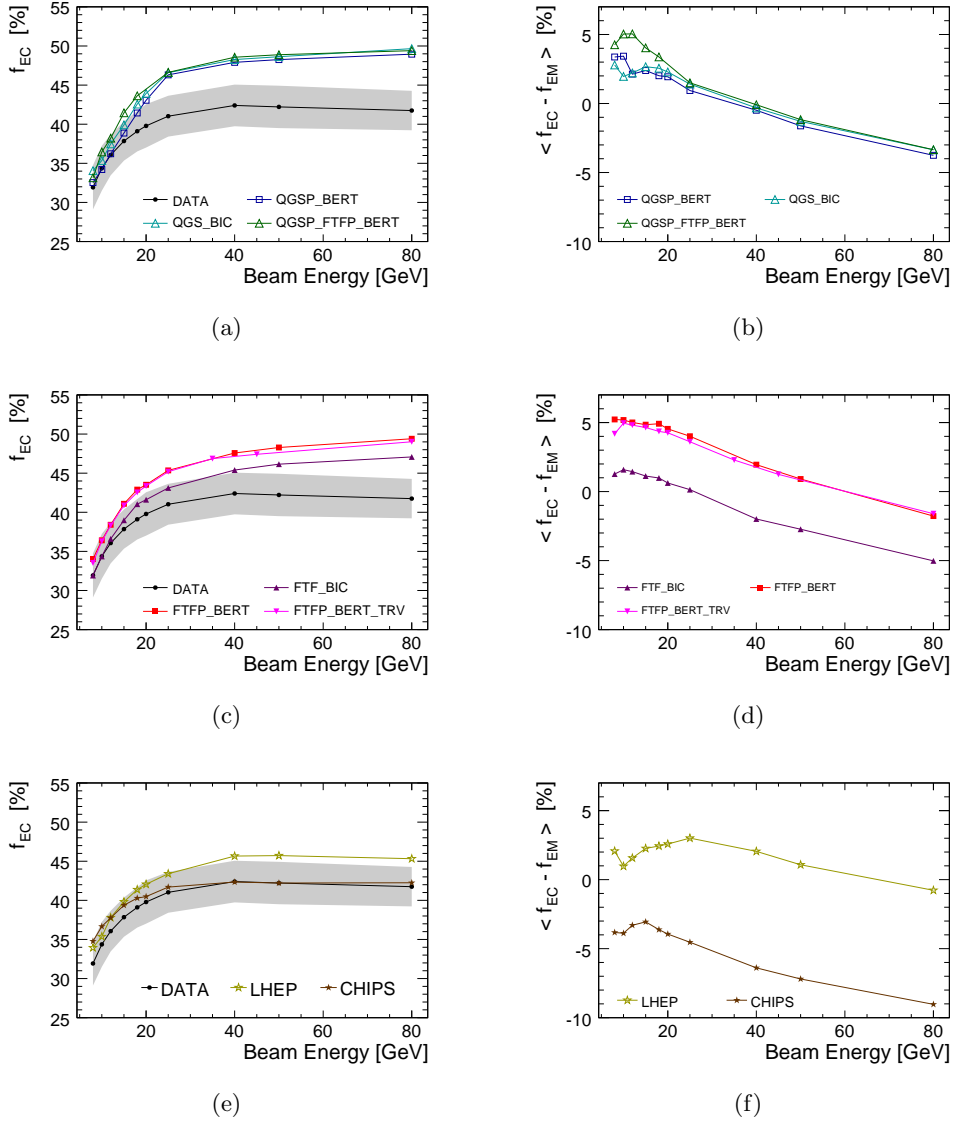
Figure 9.5.: (a),(c) and (d): Fraction of energy f_{EC} deposited in electromagnetic-like clusters found by the Deep Analysis algorithm as a function of the beam energy in data and simulations. (b),(d) and (e): Difference between f_{EC} and the real electromagnetic fraction f_{EM} in the simulations for each physics list separately.
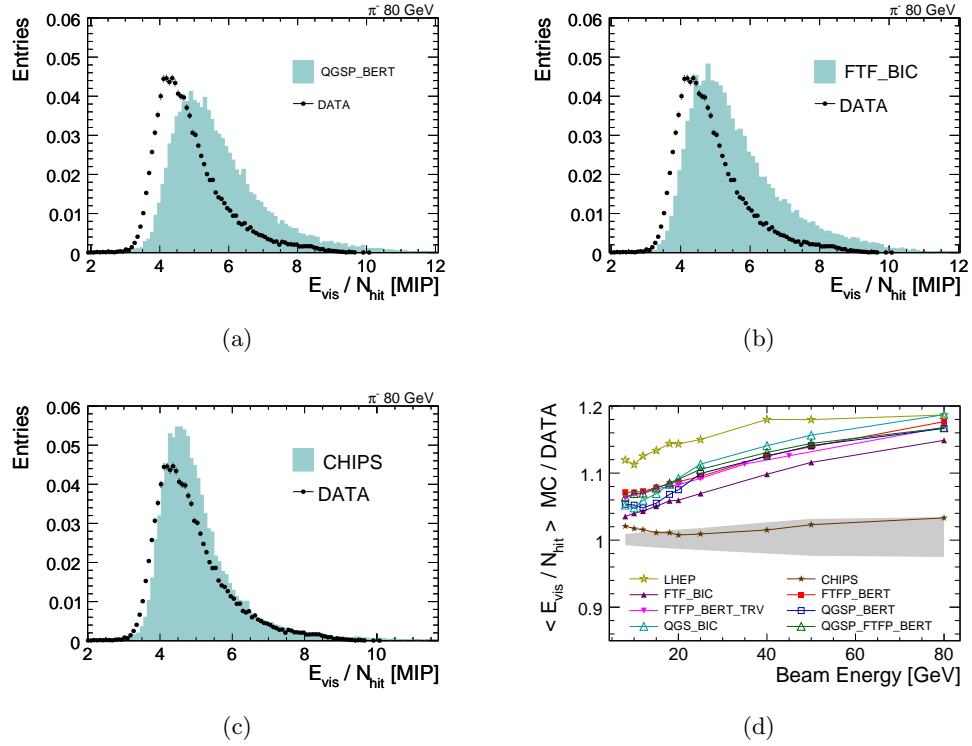
Figure 9.6.: (a)-(c): Distribution of the energy density $\rho = E_{\mathrm{vis}}/N_{\mathrm{hit}}$ for simulations using the QGSP_BERT, the FTFP_BERT and the CHIPS physics lists. Data are overlaid as black points. (d) Ratio of ρ between simulations and data as a function of the beam energy.

10. Conclusion and Summary

The subject of this thesis is the study of the CALICE AHCAL as a prototype for a hadron calorimeter at a future lepton collider. As one of the first large scale applications of the novel SiPM sensors, the AHCAL is a feasibility study for the realization of a highly granular calorimeter using this new type of photodetectors. The work presented comprises the operation of the prototype during the test beam data taking periods, the calibration of all calorimeter cells, the study of new approaches for the hadronic shower reconstruction, and the examination of different models to simulate hadronic interactions in matter.

Test Beam Data Acquisition

In the framework of this thesis, the combined setup consisting of the AHCAL and the Si-W ECAL, the TCMT, the trigger system, and various devices for particle identification and monitoring of the beam parameters was installed and commissioned at CERN in 2007 and at Fermilab in 2008. In order to increase the rate of triggered pion events and to reduce the electron events from the low-energy mixed beam at Fermilab, a Čerenkov counter was integrated into the trigger system. The ongoing analysis of the Fermilab data shows that the application of the Čerenkov information in the trigger decision successfully increased the pion fraction in the low energy beams. During the second period of the Fermilab test beam campaign, the new ScECAL prototype was installed and integrated into the common data acquisition system. Data has been acquired with the detectors shifted and rotated relative to the beam axis. A stable operation of the calorimeters over several months was achieved. Several million events with showers created by electron, positron, pion and proton beams have been collected in the energy range from 1 to 180 GeV.

Calibration

Besides the many advantages of the SiPM sensors, their temperature dependent and non-linear behaviour poses a challenge on the calibration of the AHCAL. A MIP based calibration is used, which is obtained from muon test beam data. The gain and the saturation behaviour of the SiPMs is determined using the LED system. The temperature dependent gain and response of the SiPMs have been measured and correction factors were obtained for the individual channels.

A method to correct the temperature dependence of the SiPMs has been developed and integrated into the official CALICE reconstruction framework. The temperature

correction has been validated with positron data in the energy range $10 - 50\,\mathrm{GeV}$. By applying these temperature corrections, the measured calorimeter response can be brought into agreement with the predictions from simulations. Without the temperature correction, an energy scale factor of $w_{\mathrm{ntc}} = (38.3 \pm 0.5)\,\mathrm{MIP/GeV}$ is found for data which is not compatible with $w_{\mathrm{MC}} = (41.9 \pm 0.5)\,\mathrm{MIP/GeV}$ determined for the simulations. The value $w_{\mathrm{avg}} = (42.9 \pm 0.5)\,\mathrm{MIP/GeV}$ obtained from data with the temperature correction applied is in good agreement with w_{MC}. The deviation from linearity which is below $1\,\%$ in the energy range $10 - 30\,\mathrm{GeV}$, is not affected by the temperature correction. It was shown that, with the given temperature measurement precision of $\pm 0.5\,^{\circ}\mathrm{C}$, it is sufficient to correct the behaviour of all SiPMs with the correction factors for the gain and for the MIP calibration averaged over all channels. No improvement in the resolution or linearity of the calorimeter response is gained if individual values on the single channels are applied.

The method to transport the calibration constants to different temperatures was also successfully applied in a study in reply to the questions from the International Detector Advisory Group (IDAG). The questions concerned the calibration of the energy response of the hadronic scintillator calorimeter as part of the ILD detector [86]. In this study, the information from the test beam data is used to extrapolate the calibration uncertainty including temperature variations to the full size detector. It is proven that the calibration constants obtained during the higher temperatures at Fermilab can be applied to the data from CERN without degrading the linearity and energy resolution of the prototype.

Data Analysis

In this thesis, pion showers acquired at CERN in 2007 in the energy range from 8 to $80\,\mathrm{GeV}$ have been analysed. The high granularity of the AHCAL has been exploited to use new ways in the investigation of hadronic showers.

The First Hadronic Interaction

An existing algorithm to determine the position of the first nuclear interaction of hadrons in the calorimeter has been studied and improved. An energy dependent parametrization of one of the thresholds used to find the first interaction was implemented and tuned. The refinement improved the offset and the correlation between the true position of the first interaction in the simulation and the one found by the algorithm for all physics lists at lower energies. The performance after the revision is much more independent of the beam energy and the mean offset is -0.5 layers with an uncertainty of ± 1.1 layers. As a future improvement, the implementation of an energy dependent parametrization for all thresholds is suggested. Instead of using the accumulated average as it is implemented in the current version of the algorithm, the derivative of the energy deposition in longitudinal direction should be a more suitable variable to judge the position of the first interaction. The reason

for this is that the energy deposition in the calorimeter is almost constant until the shower starting point where it increases. This increase should be most distinct in the derivative than in the accumulated energy. Further improvement might be achieved including the transverse information since the lateral spread of the energy deposition also increases after the first interaction.

Comparison of Hadronic Shower Measurements and Simulations

Several different models for the description of hadronic interaction in matter exist in the Geant 4 simulation framework. They are actively being developed and are widely used in high energy physics, e.g. by the CMS and ATLAS experiments at the LHC. The high-resolution test beam data from the AHCAL allows to investigate the models at a new level of detail. In this analysis, seven models combined in different ways in eight physics lists have been studied and compared to data. For each energy point and each physics list at least $200 \cdot 10^3$ events have been simulated and processed by the CALICE AHCAL reconstruction chain. The time necessary to simulate hadronic interactions including the simulation of the AHCAL detector effects on this level of detail is comparable with the time needed to collect the events in the test beam measurements. The high statistics would not be achievable without massive parallel computing, which only has become available in the last years. The production of simulated events still requires a non-negligible amount of time-consuming work.

The simulations have been tested with the test beam data along several variables. The effective hadronic interaction length of pions in the AHCAL has been measured in data to be $\lambda_{int} = 29.1 \pm 1.0 \, cm$ which is compatible with the expected value of $28 \, cm$ [30] and in agreement with the QGS and Fritiof physics lists at most energies.

The detector response has been studied as well as the longitudinal and transverse shower development. In the longitudinal direction, the algorithm to find the first interaction inside the AHCAL has been used to study high-resolution longitudinal profiles relative to the shower starting position. While the hadronic interaction length of pions and the response of the AHCAL is described reasonably well by the QGS and Fritiof physics lists, in the lateral and transverse shower development there are still discrepancies visible throughout all physics lists. In general the simulations with the QGS and Fritiof physics lists agree with data within approximately $20\,\%$ in all studied properties (cf. table 8.3). The LHEP physics list is not in agreement with data in many points and the presented results suggest not to use the LEP and HEP models as a stop-gap in other physics lists, as it is currently still the case. The recently extended CHIPS model is promising because it can be applied over the full energy range studied and no combination of different models is necessary. However, it does not describe the observations in data in its current development state[1]. Further tuning of some of its parameters are meant to improve its predictions. The

---

[1]This study refers to the version in Geant 4.9.3p01.

author has already pointed out the key reasons of the disagreement and identified possible improvements [76]. The results from the comparison of the data to the various simulations are a valuable source of information for their future improvement. Results obtained in this analysis have been given as feedback to the Geant 4 developers [87].

The Electromagnetic Fraction

The fluctuations in the electromagnetic fraction are the main reason for the poor resolution in non-compensating hadronic energy measurements. To identify the electromagnetic fraction event-by-event is a challenge but can lead to a significant improvement of the energy resolution. The high granularity of the AHCAL offers the possibility of the topological reconstruction of electromagnetic like clusters in the calorimeter hits. An ad-hoc clustering algorithm has been applied to the test beam data and the simulations and its capabilities to access the electromagnetic component in pion showers has been studied for the first time. The algorithm is still in development and an attempt to improve its performance is presented. A dynamic threshold for the identification of electromagnetic like hits depending on the energy deposited in the calorimeters has been implemented. After this modification, the uncertainty of the algorithm to determine the electromagnetic fraction ranges from roughly $\pm 15\%$ at $8\,\mathrm{GeV}$ to approximately $\pm 8\,\%$ at $80\,\mathrm{GeV}$. However, the difference between the real electromagnetic fraction and the fraction of energy deposited in electromagnetic like clusters identified by the algorithm is still varying with energy and depends strongly on the physics lists. Nevertheless the correlation between the electromagnetic cluster energy found by the algorithm and the true electromagnetic component in simulations looks promising. Further adjustments of the parameters of the algorithm will improve its performance.

Outlook

In the framework of this study, the AHCAL simulation software has been extended to extract additional information about the contribution of several particle species to the energy deposition inside the calorimeter volume. The technique has been applied to overlay the electron and positron energy deposition as well as the one by hadrons to the high-resolution shower profiles in transverse and longitudinal direction. This information provides insight where in the detector volume the single components have their strongest contribution. The longitudinal shower shape relative to the first hadronic interaction is clearly dominated by the electromagnetic component at higher energies. In future studies, this information can be used to select regions in the calorimeter where a certain component is particularly dominant. This would possibly allow to measure the average electromagnetic component from transverse shower profiles in the AHCAL.

The study of the Fermilab data is ongoing and the next steps are to extend the

analysis presented here to the low energy regime. The comparison of Monte Carlo simulations at energies down to 1 GeV are of special interest since they would allow to differentiate better between the low energy Binary and Bertini cascade models. Up to now only a partial description of the Fermilab beam line instrumentation exists and a more exact modelling of the setup is planned.

The clustering algorithm investigated in this thesis has the potential to measure the electromagnetic fraction in hadronic showers event wise. In future studies, this information will be used to correct for the different response of the AHCAL to the electromagnetic and hadronic shower components. This will hopefully result in an improvement of the hadronic energy resolution which is also interesting for a full scale ILC detector for high energy jets in which the Particle Flow approach fails.

10. Conclusion and Summary

A. Primary Track Finder Performance

Figures A.1 and A.2 show the mean difference $<\Delta>$ between the true shower starting layer and the one found by the algorithm for all physics lists tested as a function of the beam energy before and after the improvement. The uncertainty is indicated by the grey band which shows the range of Δ for 66% of all events. One can see a clear reduction of the energy dependency, and the asymmetry in the uncertainty vanishes.

The correlation between the true first interaction position and the one found by the algorithm is shown as a function of the beam energy in figure A.3. Before the improvement (dashed line) the correlation increased with growing beam energy. After the refinement (solid line), the correlation is higher for all physics lists and the energy dependency almost vanishes completely.

Still, after the improvement the performance of the algorithm is strongly dependent on the physics lists used. Almost the same behaviour is observed for the Fritiof physics lists. Also, the performance of the algorithm is similar for QGS lists. The performance is best for LHEP and worst for CHIPS.
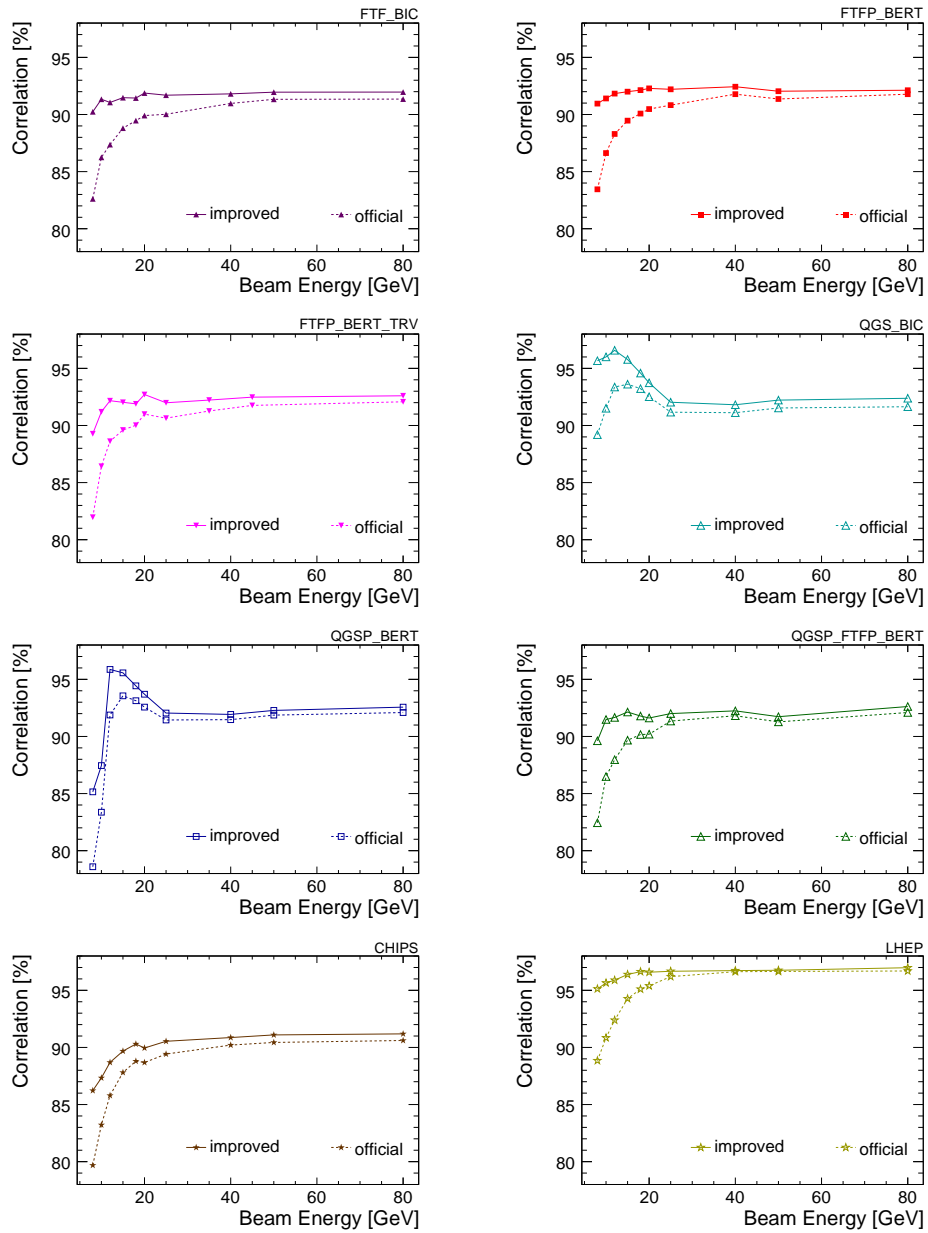
Figure A.1.: Mean difference between the true layer of the first hard interaction in the simulations and the one found by the detection algorithm before and after the improvement.
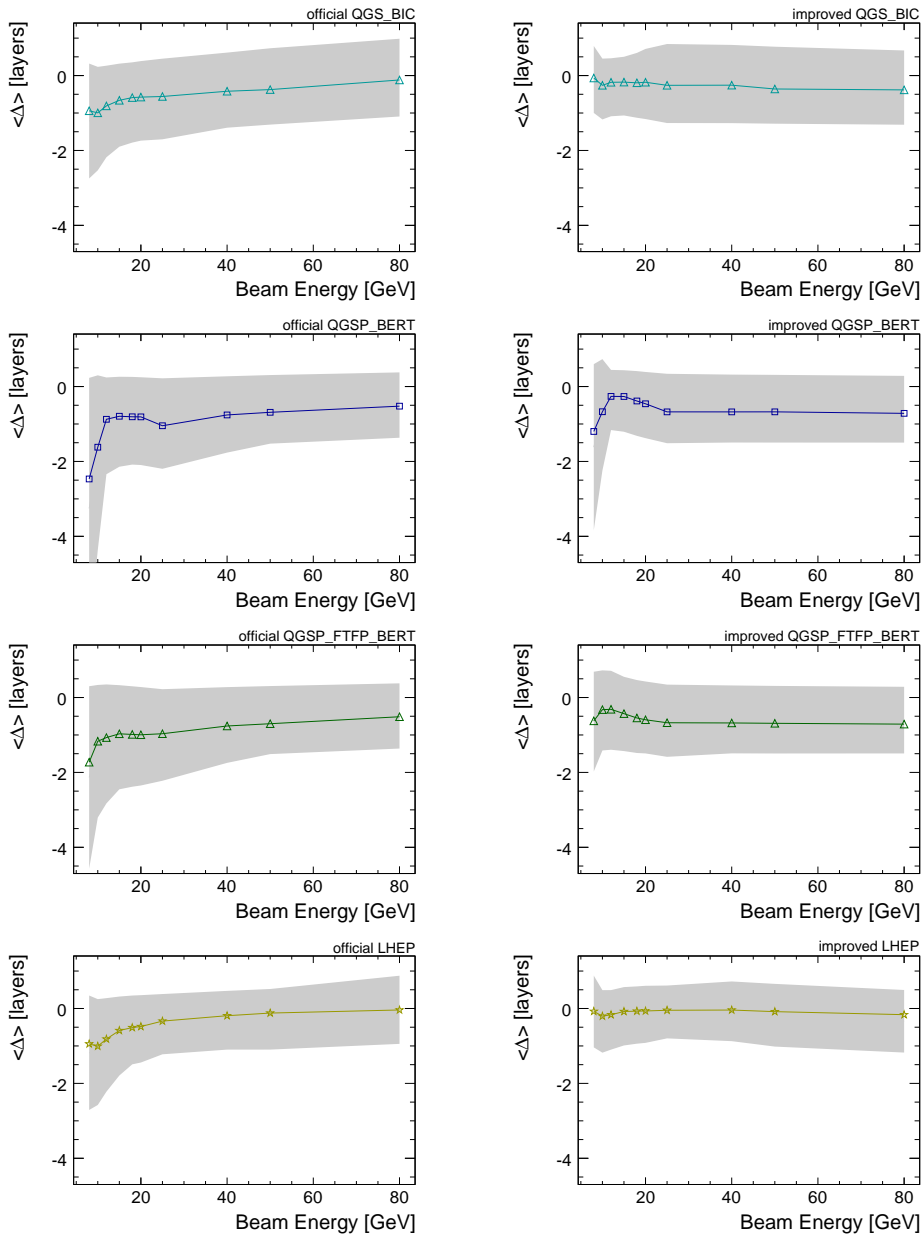
Figure A.2.: Mean difference between the true layer of the first hard interaction in the simulations and the one found by the detection algorithm before and after the improvement.

Figure A.3.: Correlation between the true layer of the first hard interaction in the simulations and the one found by the detection algorithm before (dashed line) and after (solid line) the improvement.

B. Calibration Uncertainties

In order to estimate the impact of the calibration uncertainties on the data studied in this thesis, the data have been reconstructed several times varying the input parameters used in the AHCAL calibration chain by the values listed in table B.1. The motivation for these variation are explained briefly in this chapter.

The AHCAL calibration procedure is described in chapter 6.1. In order to make the equations below better readable, the following definitions are used:

$$
\begin{align}
a &= A_i \, [\mathrm{ADC}] - P_i \, [\mathrm{ADC}] \tag{B.1}\\
m &= M_i \, [\mathrm{ADC}] \tag{B.2}\\
g &= G_i \, [\mathrm{ADC}] \tag{B.3}\\
ic &= I_i \tag{B.4}
\end{align}
$$

The calibration of a single calorimeter cell from the ADC to the MIP scale is summarized in equation 6.2, which can be transformed to:

$$
\begin{align}
E \, [\mathrm{MIP}] &= \frac{a}{m} \cdot f_{sat}^{-1}\left(N_{\mathrm{pix}}\right) \tag{B.5}\\
&= \frac{1}{m} \cdot \frac{g}{ic} \cdot N_{\mathrm{pix}} \cdot f_{sat}^{-1}\left(N_{\mathrm{pix}}\right) \tag{B.6}\\
&= \frac{1}{m} \cdot \frac{g}{ic} \cdot N_{\mathrm{pix}} \cdot \frac{-N_{\mathrm{eff}}}{N_{\mathrm{pix}}} \cdot \ln\left(1 - \frac{N_{\mathrm{pix}}}{N_{\mathrm{eff}}}\right) \tag{B.7}\\
&= \frac{-N_{\mathrm{eff}}}{m} \cdot \frac{g}{ic} \cdot \ln\left(1 - \frac{N_{\mathrm{pix}}}{N_{\mathrm{eff}}}\right) \tag{B.8}\\
&= \frac{-N_{\mathrm{eff}}}{m} \cdot \frac{g}{ic} \cdot \ln\left(1 - \frac{a}{N_{\mathrm{eff}}}\frac{ic}{g}\right) \tag{B.9}
\end{align}
$$

Equation B.9 is implemented in the calibration code in the CALICE reconstruction software.

Due to the mismatch between the wavelength-shifting fibre cross-section and the active area of the SiPMs, the effective number of pixels of the SiPMs in the AHCAL N_{eff} is calculated from the effective number of pixels determined on the ITEP test bench n_{eff}:

$$
N_{\mathrm{eff}} = S \cdot n_{\mathrm{eff}} \tag{B.10}
$$

Parameter	Description	Uncertainty
m	MIP Constant	$\pm 2\,\%$
dm/dT	MIP Temperature Dependence	$\pm 30\,\%$
S	Saturation Scaling	$\pm 10\,\%$
ic	Inter-calibration	cancel
g	Gain Constant	cancels
dg/dT	Gain Temperature Dependence	not significant

Table B.1.: Systematic uncertainty assumption for the calibration parameters.

The measurement of S depends linearly on $\frac{ic}{g}$:

$$S = \tilde{s} \cdot \frac{ic}{g} \tag{B.11}$$

Replacing B.11 and B.10 in B.9 shows that the uncertainty on g and ic cancel in the single cell calibration:

$$E\,[\text{MIP}] = \frac{-\tilde{s} \cdot n_{\text{eff}}}{m} \cdot \ln\left(1 - \frac{a}{\tilde{s} \cdot n_{\text{eff}}}\right) \tag{B.12}$$

However, in reconstruction procedure unfortunately not the single cell rescaling factors S are used, but the average $<S>$. To estimated the impact on the calibration uncertainty on the data studied in this thesis the uncertainty on $\frac{ic}{g}$ is assumed to cancel nevertheless and the relatively large $10\,\%$ spread of the distribution of S shown in figure 6.9(b) is applied an uncertainty on S.

The validation of the temperature correction procedure explained in chapter 6.4 showed that effect of the uncertainty on the temperature dependence dg/dT of the gain is not significant.

Individual values of the MIP calibration constants are applied for each single channel of the calorimeter. The uncertainty on the determination of the MIP values is $2\,\%$ [51].

Since for the MIP temperature dependence the average value of the distribution shown in figure 6.12(a) for all AHCAL channels its relatively large value of $\pm 30\,\%$ is assumed as uncertainty on dM/dT.

C. Deep Analysis Performance

The average difference $<\Delta>=<f_{\mathrm{EC}}-f_{\mathrm{EM}}>$ before and after the implementation of the dynamic threshold is compared in figures C.1 and C.2. The grey band indicates the range which holds $66\,\%$ of the events in the distribution of Δ. The width of this range is a measure for the event-wise uncertainty of the method. In the official version with the fixed threshold of the algorithm, $<\Delta>$ grows with increasing beam energy. After the modification, there is a negative energy dependence. Such a shift could be easily corrected for; it is however strongly dependent on the physics lists.

The correlations of f_{EC} and f_{EM} as a function of the beam energy for all tested simulations are shown in figure C.3. While the modification of the algorithm does not change the correlation in the lower energy range, above $18\,\mathrm{GeV}$ an improvement is visible for all physics lists. After the attempt to enhance the performance of the algorithm, there is still almost no correlation at lower energies and only a correlation of $77-85\,\%$ at $80\,\mathrm{GeV}$, depending on the physics list.

Figure C.1.: Mean difference between the true electromagnetic fraction f_{EM} and the fraction of energy deposited in electromagnetic like clusters f_{EC} before and after the improvement of the algorithm.
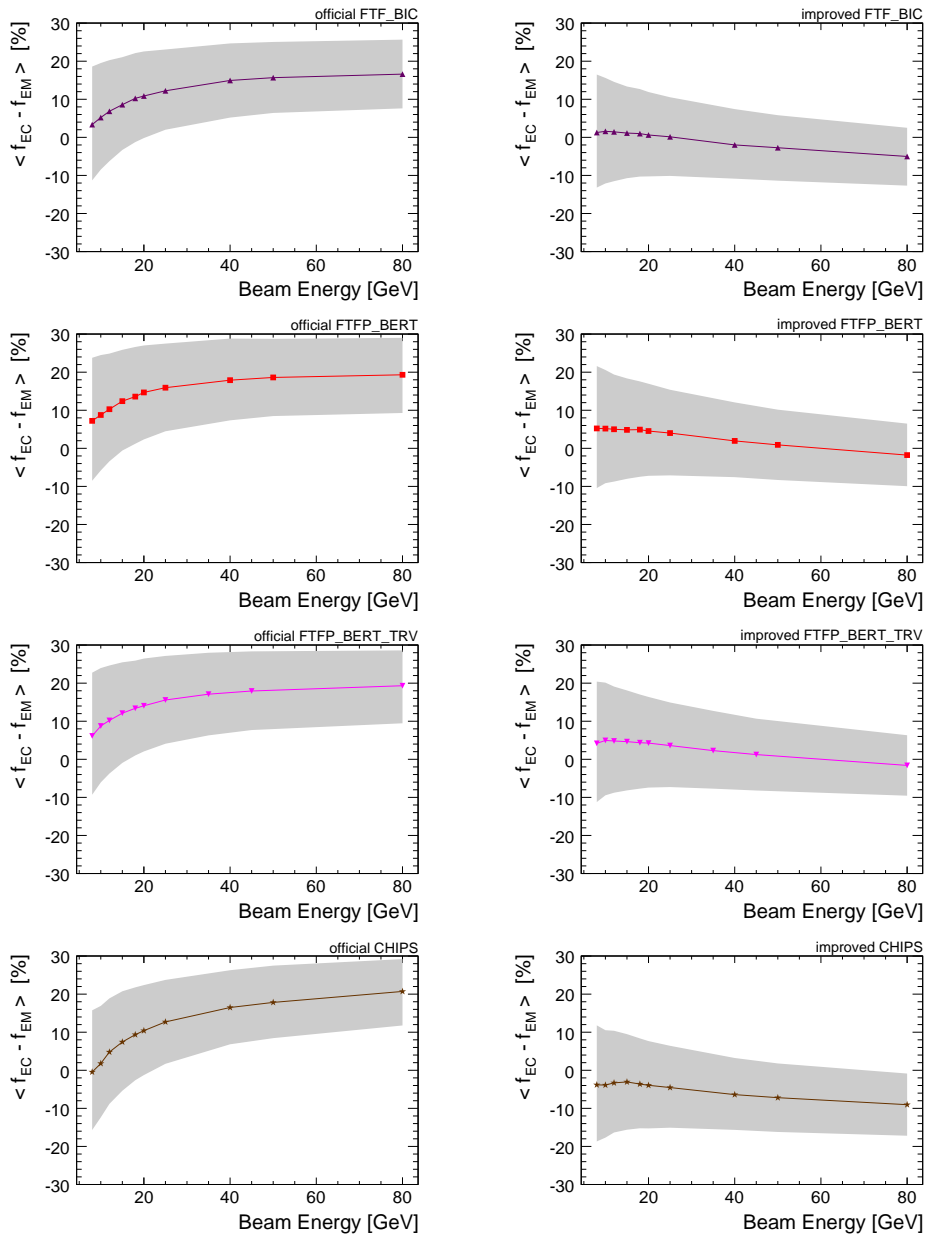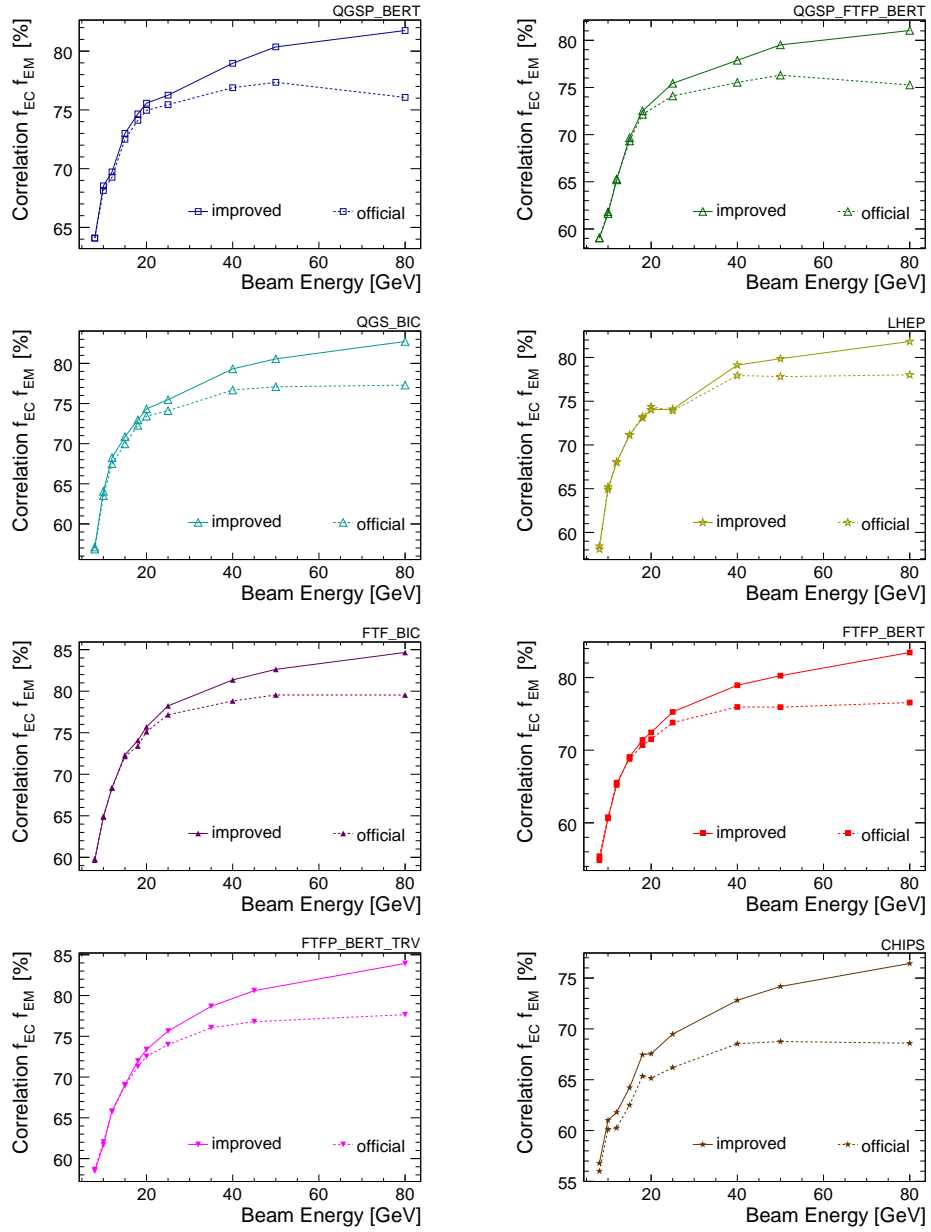
Figure C.2.: Mean difference between the true electromagnetic fraction f_{EM} and the fraction of energy deposited in electromagnetic like clusters f_{EC} before and after the improvement of the algorithm.

Figure C.3.: Correlation between the true electromagnetic fraction f_{EM} and the fraction of energy deposited in electromagnetic like clusters f_{EC} before (dashed line) and after (solid line) the improvement of the algorithm.

Bibliography

[1] M. Thomson, "Particle Flow Calorimetry and the PandoraPFA Algorithm," *Nucl.Instrum.Meth.* **A611** (2009) 25–40, `arXiv:0907.3577 [physics.ins-det]`.

[2] C. Leroy and P. Rancoita, *Principles of radiation interaction in matter and detection.* World Scientific, 2009. `http://books.google.com/books?id=jENKPwAACAAJ`.

[3] R. Wigmans, *Calorimetry: energy measurement in particle physics.* International series of monographs on physics. Clarendon Press, 2000. `http://books.google.com/books?id=vD9RFluMD5sC`.

[4] W. Lohmann and R. Kopp and R. Voss, "Energy Loss of Muons in the Energy Range $1 - 10000\, GeV$," *CERN yelllow report* (1985) CERN 85–03. `http://cdsweb.cern.ch/record/158706/files/CERN-85-03.pdf`.

[5] B. Rossi, *High-energy particles.* Prentice-Hall physics series. Prentice-Hall, 1952. `http://books.google.de/books?id=hr9EAAAAIAAJ`.

[6] T. Gabriel, D. Groom, P. Job, N. Mokhov, and G. Stevenson, "Energy dependence of hadronic activity," *Nuclear Instruments and Methods in Physics Research Section A: Accelerators, Spectrometers, Detectors and Associated Equipment* **338** no. 2-3, (1994) 336 – 347. `http://www.sciencedirect.com/science/article/B6TJM-473FMY7-1JJ/2/24d8e877c1c74d367cf6e5cee5ad1b4a`.

[7] D. E. Groom, "Energy flow in a hadronic cascade: Application to hadron calorimetry," *Nuclear Instruments and Methods in Physics Research Section A: Accelerators, Spectrometers, Detectors and Associated Equipment* **572** no. 2, (2007) 633 – 653. `http://www.sciencedirect.com/science/article/B6TJM-4MR1GTX-2/2/757148c5940f2db642f2782795dcf317`.

[8] C. Leroy and P.-G. Rancoita, "Physics of cascading shower generation and propagation in matter: principles of high-energy, ultrahigh-energy and compensating calorimetry," *Reports on Progress in Physics* **63** no. 4, (2000) 505. `http://stacks.iop.org/0034-4885/63/i=4/a=202`.

[9] N. Akchurin, O. Atramentov, K. Carrell, K. Gms, J. Hauptman, H. Kim, H. Paar, A. Penzo, and R. Wigmans, "Separation of scintillation and Cherenkov light in an optical calorimeter," *Nuclear Instruments and Methods in Physics Research Section A: Accelerators, Spectrometers, Detectors and Associated Equipment* **550** no. 1-2, (2005) 185 – 200.

http://www.sciencedirect.com/science/article/B6TJM-4GR32SV-1/2/08240b47bafaafce560d8be746222945.

[10] J. Brau et al., "ILC Reference Design Report." http://www.linearcollider.org/about/Publications/Reference-Design-Report, Dec, 2007.

[11] ILC / form one visual communication, "A schematic layout of the International Linear Collider."
HTTP://WWW.INTERACTIONS.ORG/CMS/?PID=2100&IMAGE_NO=OT0104.

[12] J. Brau et al., "ILC Reference Design Report Volume 3: Accelerator."
http://www.linearcollider.org/about/Publications/Reference-Design-Report, Dec, 2007.

[13] Copyright 2006 DESY, "Photograph of a TESLA niobium cavity."
HTTP://WWW.INTERACTIONS.ORG/CMS/?PID=2100&IMAGE_NO=DE0083.

[14] GLD Concept Study Group, "GLD Detector Outline Document," *ArXiv Physics e-prints* (July, 2006) , arXiv:physics/0607154.

[15] LDC Group for the RDR of the ILC, "Detector Outline Document for the Large Detector Concept."
http://www.ilcild.org/documents/ldc/outlinedoc/view, 2006.

[16] SiD Concept Group, "Silicon Detector Letter of Intent."
https://confluence.slac.stanford.edu/display/SiD/LOI, March, 2009.

[17] The Fourth (4th) Detector Collaboration, "Letter of Intent."
http://www.4thconcept.org/4LoI.pdf, 2009.

[18] ILD Concept Group, "Letter of Intent," March, 2009.

[19] R. Wigmans, "The DREAM project–Towards the ultimate in calorimetry,"
Nuclear Instruments and Methods in Physics Research Section A: Accelerators, Spectrometers, Detectors and Associated Equipment **617** no. 1-3, 129 – 133.
http://www.sciencedirect.com/science/article/B6TJM-4XDD017-5/2/ac392fc3bbff1c9337ea3b1a6c3300cf. 11th Pisa Meeting on Advanced Detectors - Proceedings of the 11th Pisa Meeting on Advanced Detectors.

[20] J. Brau et al., "ILC Reference Design Report Volume 4: Detectors."
http://www.linearcollider.org/about/Publications/Reference-Design-Report, Dec, 2007.

[21] The CALICE collaboration, "Design and Electronics Commissioning of the Physics Prototype of a Si-W Electromagnetic Calorimeter for the International Linear Collider," *Journal of Instrumentation* **3** no. 08, (2008) P08001. http://stacks.iop.org/1748-0221/3/i=08/a=P08001.

[22] K. Kotera, "Study of the granular electromagnetic calorimeter with PPDs and scintillator strips for ILC," *NIM A* **In Press, Corrected Proof** (2010) .
http://www.sciencedirect.com/science/article/B6TJM-50H1WHP-N/2/2f478fbd35c80a60534c25cad691f83b.

[23] Misato Hayashida, "CALICE meeting in Korea," *ILC Newsline* .

[24] B. Bilki, J. Butler, T. Cundiff, G. Drake, W. Haberichter, E. Hazen, J. Hoff, S. Holm, A. Kreps, E. May, G. Mavromanolakis, E. Norbeck, D. Northacker, Y. Onel, J. Repond, D. Underwood, S. Wu, and L. Xia, "Calibration of a digital hadron calorimeter with muons," *Journal of Instrumentation* **3** no. 05, (2008) P05001. http://stacks.iop.org/1748-0221/3/i=05/a=P05001.

[25] C. Adloff, J. Blaha, J.-J. Blaising, M. Chefdeville, A. Espargilière, and Y. Karyotakis, "Monte Carlo study of the physics performance of a digital hadronic calorimeter," *Journal of Instrumentation* **4** no. 11, (2009) P11009. http://stacks.iop.org/1748-0221/4/i=11/a=P11009.

[26] Jae Yu, "GEM DHCAL status." HTTP://ILCAGENDA.LINEARCOLLIDER.ORG/GETFILE.PY/ACCESS?CONTRIBID= 150&SESSIONID=18&RESID=1&MATERIALID=SLIDES&CONFID=4572, 2011.

[27] C. Adloff, J. Blaha, M. Chefdeville, A. Dalmaz, C. Drancourt, A. Espargilière, R. Gaglione, Y. Karyotakis, J. Prast, and G. Vouters, "Beam test of a small MICROMEGAS DHCAL prototype," *Journal of Instrumentation* **5** no. 01, (2010) P01013. http://stacks.iop.org/1748-0221/5/i=01/a=P01013.

[28] K. Francis, *Results Of Beam Tests of a Prototype Calorimeter For a Linear Collider*. PhD thesis, Northern Illinois University, 2010.

[29] The CALICE Collaboration, "PandoraPFA tests using overlaid charged pion test beam data," *paper in preparation* (2011) .

[30] The CALICE Collaboration, "Construction and commissioning of the CALICE analog hadron calorimeter prototype," *Journal of Instrumentation* **5** no. 05, (2010) P05004. http://stacks.iop.org/1748-0221/5/i=05/a=P05004.

[31] **CALICE Collaboration** Collaboration, R. Fabbri, "CALICE Second Generation AHCAL Developments," arXiv:1007.2358 [physics.ins-det].

[32] N. Feege, *Silicon Photomultipliers: Properties and Application in a Highly Granular Calorimeter*. Diploma thesis, University of Hamburg, 2008. http://www-library.desy.de/preparch/desy/thesis/desy-thesis-08-050.pdf.

[33] Erika Garutti et al., "Magnetic Field Dependence Studies for Silicon Photomultiplier." http://www-flc.desy.de/store/hcal/paper/LC-DET-2004-025.ps, 2004. LC-DET-2004-025.

[34] B. Dolgoshein et al., "Status report on silicon photomultiplier development and its applications," *Nuclear Instruments and Methods in Physics Research Section A: Accelerators, Spectrometers, Detectors and Associated Equipment* **563** no. 2, (2006) 368 – 376. http://www.sciencedirect.com/science/article/B6TJM-4JJGFF4-3/2/3e3847074c213064b69eb4c1db368c91. TRDs for the Third Millenium - Proceedings of the 3rd Workshop on Advanced Transition Radiation Detectors for Accelerators and Space Applications.

[35] P. Buzhan, B. Dolgoshein, A. Ilyin, V. Kantserov, V. Kaplin, *et al.*, "An advanced study of silicon photomultiplier," *ICFA Instrum.Bull.* **23** (2001) 28–41.

[36] S. Blin et al., "Dedicated very front-end electronics for an ILC prototype hadronic calorimeter with SiPM readout," *LC-Note* (2006) LC–DET–2006–007. http://www-flc.desy.de/lcnotes/notes/LC-DET-2006-007.pdf.

[37] B. Lutz, *Commissioning of the Readout Electronics for the Prototypes of a Hadronic Calorimeter and Tailcatcher and Muontracker.* Diploma thesis, University of Hamburg, 2006. http://www-library.desy.de/preparch/desy/thesis/desy-thesis-06-038.pdf.

[38] N. Wattimena, *Commissioning of an LED Calibration & Monitoring System for the Prototype of a Hadronic Calorimeter.* Diploma thesis, University of Hamburg, 2006. http://www-library.desy.de/preparch/desy/thesis/desy-thesis-06-039.pdf.

[39] M. Groll, *Construction and Commissioning of a Hadronic Test-Beam Calorimeter to Validate the Particle-Flow Concept.* PhD thesis, University of Hamburg, 2007. http://www-library.desy.de/preparch/desy/thesis/desy-thesis-07-018.pdf.

[40] N. Wattimena, *Calorimetry at the International Linear Collider - From Simulation To Reality.* PhD thesis, University of Hamburg, 2009. http://www-library.desy.de/preparch/desy/thesis/desy-thesis-10-006.pdf.

[41] I. Efthymiopoulos, "Target Station T4 Wobbling - Explained." sba.web.cern.ch/sba/Documentations/Target/T4/T4Wobbling3.pdf, February, 2003. CERN SPS SBA documentation, AB / ATB-EA / IE.

[42] B. Lutz, *Hadron Showers in a Highly Granular Calorimeter.* PhD thesis, University of Hamburg, 2010. http://www-flc.desy.de/hcal/documents/2010/PhD_Thesis_beni_Lutz_2010.pdf.

[43] J. Spanggaard, "Delay Wire Chambers - A Users Guide." http://sl.web.cern.ch/SL/Publications/bi98-023.pdf, 1998.

[44] "The Fermilab Test Beam Facility." http://www-ppd.fnal.gov/FTBF/.

[45] N. Feege, "Low-energy Pions in the Analogue HCAL." http://ilcagenda.linearcollider.org/getFile.py/access?contribId=17&sessionId=4&resId=0&materialId=slides&confId=4391, 2010.

[46] J. R. et al., "Design and electronics commissioning of the physics prototype of a Si-W electromagnetic calorimeter for the International Linear Collider," *Journal of Instrumentation* **3** no. 08, (2008) P08001. http://stacks.iop.org/1748-0221/3/i=08/a=P08001.

[47] The CALICE Collaboration, "The Scintillator-ECAL Beam Test at DESY in 2007 - Update 1," *CALICE Analysis Note* **006** (2007) .

[48] Toshi Ikuno, "Preliminary test beam anlysis during the data acquistion at FTBF in September 2008.".

[49] N. D'Ascenzo, "The reconstruction of the energy lost by a 120 GeV muon in the highly granular hadron calorimeter for the International Linear Collider," *CALICE Analysis Note* **009** (2008) .

[50] The CALICE Collaboration, "Construction and commissioning of the CALICE analog hadron calorimeter prototype," *Journal of Instrumentation* **5** no. 05, (2010) P05004. http://stacks.iop.org/1748-0221/5/i=05/a=P05004.

[51] The CALICE Collaboration, "Muon response of a highly granular hadronic calorimeter," *to be published* (2011) .

[52] A.Kaplan, "Correction of SiPM temperature dependencies," *Nuclear Instruments and Methods in Physics Research Section A: Accelerators, Spectrometers, Detectors and Associated Equipment* **610** no. 1, (2009) 114 – 117. New Developments In Photodetection NDIP08, Proceedings of the Fifth International Conference on New Developments in Photodetection.

[53] The CALICE Collaboration, "Electron data with the CALICE tile AHCAL prototype at the CERN test-beam - Effect of temperature correction ," *CALICE Analysis Note* **014** (2008) .

[54] A. Vargas, "Muon Calibration." Private communication.

[55] S. Agostinelli et al., "Geant 4 – a simulation toolkit," *NIM A* **506** no. 3, (2003) 250 – 303. http://www.sciencedirect.com/science/article/B6TJM-48TJFY8-5/2/23ea98096ce11c1be446850c04cfa498.

[56] P.M. de Freitas et al., "Mokka - a detailed Geant4 simulation for the International Linear Collider detectors." http://polzope.in2p3.fr:8081/MOKKA/.

[57] G. Folger and J. Wellisch, "String parton models in GEANT4," arXiv:nucl-th/0306007 [nucl-th].

[58] "Geant 4 Physics Reference Manual." https://geant4.web.cern.ch/geant4/UserDocumentation/UsersGuides/PhysicsReferenceManual/fo/PhysicsReferenceManual.pdf.

[59] H. Fesefeldt, "The Simulation Of Hadronic Showers: Physics And Applications." http://alice.cern.ch/format/showfull?sysnb=0074252, Dec., 1985.

[60] J. J. Griffin, "Statistical Model of Intermediate Structure," *Phys. Rev. Lett.* **17** no. 9, (Aug, 1966) 478–481.

[61] A. Heikkinen, N. Stepanov, and J. P. Wellisch, "Bertini intranuclear cascade implementation in GEANT4," arXiv:nucl-th/0306008 [nucl-th].

[62] K. Nakamura and P. D. Group, "Review of Particle Physics," *Journal of Physics G: Nuclear and Particle Physics* **37** no. 7A, (2010) 075021.

http://stacks.iop.org/0954-3899/37/i=7A/a=075021.

[63] G. Folger, V. N. Ivanchenko, and J. P. Wellisch, "The Binary Cascade," *The European Physical Journal A - Hadrons and Nuclei* **21** (2004) 407–417. http://dx.doi.org/10.1140/epja/i2003-10219-7. 10.1140/epja/i2003-10219-7.

[64] P. Degtyarenko, M. Kosov, and H. Wellisch, "Chiral invariant phase space event generator. I: Nucleon antinucleon annihilation at rest," *Eur.Phys.J.* **A8** (2000) 217–222.

[65] P. Degtyarenko, M. Kossov, and H. Wellisch, "Chiral invariant phase space event generator. II: Nuclear pion capture at rest and photonuclear reactions below the Delta(3,3) resonance," *Eur.Phys.J.* **A9** (2000) 411–420.

[66] P. Degtyarenko, M. Kossov, and H. Wellisch, "Chiral invariant phase space event generator. III: Modeling of real and virtual photon interactions with nuclei below pion production threshold," *Eur.Phys.J.* **A9** (2000) 421–424.

[67] A. Lucaci, "HCAL prototype in the test beam Mokka model." http://www.desy.de/~lucaci/Others/hcalTBeam.pdf.

[68] J. Birks, *The theory and practice of scintillation counting.* International series of monographs on electronics and instrumentation. Pergamon Press; [distributed in the Western Hemisphere by Macmillan, New York], 1964. http://books.google.com/books?id=rJ9pAAAAMAAJ.

[69] M. Hirschberg, R. Beckmann, U. Brandenburg, H. Bruckmann, and K. Wick, "Precise measurement of Birks kB parameter in plastic scintillators," *Nuclear Science, IEEE Transactions on* **39** no. 4, (Aug., 1992) 511 –514.

[70] A. Tadday, "Measurement of the Birks coefficient for the AHCAL scintillator material and improvement of the Geant 4 implementation of Birks Law." Private communication.

[71] S. Richter, *Validation of the Calibration Procedure for a Highly Granular Calorimeter with Electromagnetic Processes.* Diploma thesis, University of Hamburg, 2008. http://www-flc.desy.de/hcal/documents/2008/diplom.2008.richter.pdf.

[72] The Particle Data Group, "Monte Carlo Particle Numbering Scheme." http://pdg.lbl.gov/2006/mcdata/mc_particle_id_contents.html.

[73] Alexander Kaplan, "Pion Showers in the CALICE AHCAL," *CALICE Analysis Note* **026** (2010) .

[74] M. Chadeeva, "Primary Track Finder Processor." http://www-flc.desy.de/hcal/meetings/internal/minutes2009/090326-MC_hadrons2.pdf.

[75] A. Dotti, "Implementation of the pion-nucleon cross-sections for the different physics lists in Geant 4." Private communication.

[76] M. Kosov, "CHIPS physics list in Geant4." http://ilcagenda.linearcollider.org/getFile.py/access?contribId=

126&sessionId=31&resId=0&materialId=slides&confId=4649.

[77] Nicola D'Ascenzo, *Study of the neutralino sector and analysis of the muon response of a highly granular hadron calorimeter at the International Linear Collider.* PhD thesis, University of Hamburg, 2009. http://www-library.desy.de/preparch/desy/thesis/desy-thesis-09-004.pdf.

[78] S. Banerjee et al., "Validation of GE ANT 4 Hadronic Generators versus Thin Target Data." http://geant4.cern.ch/results/papers/thin-target-validation-MC2010.pdf, 2010.

[79] N. Akchurin, K. Carrell, J. Hauptman, H. Kim, H. Paar, A. Penzo, R. Thomas, and R. Wigmans, "Hadron and jet detection with a dual-readout calorimeter," *Nuclear Instruments and Methods in Physics Research Section A: Accelerators, Spectrometers, Detectors and Associated Equipment* **537** no. 3, (2005) 537–561.

[80] Marina Chadeeva, "A new approach to software compensation for the CALICE AHCAL," *CALICE Analysis Note* **028** (2010) .

[81] K.Seidel and F.Simon, "Software Compensation for Hadronic Showers in the CALICE AHCAL and Tail Catcher with Cluster-based Methods," *CALICE Analysis Note* **021** (2010) .

[82] P. Amaral, "Hadronic shower development in Iron-Scintillator Tile Calorimetry," *Nuclear Instruments and Methods in Physics Research Section A: Accelerators, Spectrometers, Detectors and Associated Equipment* **443** no. 1, (2000) 51 – 70. http://www.sciencedirect.com/science/article/B6TJM-3YTT063-6/2/d2875eab655f182df9b7f4bdf695f5c6.

[83] V. Morgunov, "Deep Analysis of Hadronic Shower." HTTP://WWW.DESY.DE/~MORGUNOV/TALKS_ARTICLES/DEEPANALYSIS.PDF, 2007.

[84] V. Morgunov, E. Garutti , "Documentation of the DeepAnalysis code." http://www.desy.de/~garutti/DOCU/deepanalysis.pdf, 2007.

[85] V. Morgunov , "private communication.".

[86] The CALICE Collaboration, "Calibration of the Scintillator Hadron Calorimeter of ILD," *CALICE Analysis Note* **018** (2009) .

[87] J. Apostolakis, A. Dotti, E. Garutti, A. Kaplan, M. Kosov, V. Uzhinskiy, and D. Ward, "Validation of GEANT4 hadronic models using CALICE data," *EUDET-Memo-2010-15* (February, 2011) .

Bibliography

Danksagung

Ich möchte mich hier bei allen bedanken, die diese Doktorarbeit ermöglicht haben und die mich auf meinem Weg unterstüzt haben.

Zuerst bei meinem Doktorvater Herrn Prof. Dr. Hans-Christian Schultz-Coulon für die angenehme Atmosphäre in Heidelberg und das entgegengebrachte Vertrauen, mich als Gast in der AHCAL Gruppe am DESY arbeiten zu lassen. Besonders möchte ich mich dafür bedaken, dass er es mir ermöglicht hat in einer internationalen Kollaboration zu arbeiten und dass er meine intensive Mitwirkung an der Datennahme am CERN und am Fermilab unterstützt hat.

Herrn Prof. Dr. Dirk Dubbers danke ich für die freundliche Bereitschaft die Zweitkorrektur zu übernehmen.

Vielen Dank an meinen Mitbetreuer Herrn Dr. Rainer Stamen in Heidelberg, der sich für Fragen und Diskussionen immer Zeit genommen hat.

Special thanks goes to my advisor in Hamburg Dr. Erika Garutti for her never ending patience and for standing my chaotic way to work. Thank you for all the help and support with my work and beyond. Grazie di tutto!

Mein Dank gilt der gesamten FLC Gruppe am DESY, die mich freundlich aufgenommen hat und deren Gast ich seit 2007 sein durfte, besonders meinen Kollegen in der AHCAL Gruppe und deren Leiter Herrn Dr. Felix Sefkow.
Ein paar von ihnen möchte ich hier namentlich erwähnen: the software experts Niels, Angela, and Shaojun as supporters in the fight with the CALICE software and the DESY computing environment; Vasiliy for increasing my humble knowledge on shower physics; Sebastian Schätzel, Marius, Sebastian Schmitt, Nanda, Ivan, Andrea, Clemens, Mark, Riccardo, Marina, Jaroslav; Beni und Nils mit denen ich die Ehre hatte die Tage und Nächte mit Arbeiten am Testrahlaufbau zu vetrieben.

I also would like to thank all friends and colleagues in the CALICE collaboration who supported me over the time:

Prof. Dr. David Ward, Dr. Jose Repond, Dr. Fabrizio Salvatore and Dr. Matthew Wing for the review and discussion of my analysis; everyone who contributed to the test beam programs for the good collaboration, especially our hosts at CERN and at Fermilab; Aria Soha, Dr. Erik Ramberg, Todd Nebel, Winslow Baker, the whole Japanese test beam team, Prof. Dr. Thoru Takeshita, Prof. Dr. Satoru Uozumi, Dr. Katsushige Kotera and Dr. Daniel Jeans, the whole TCMT team, Dr. Vishnu Zutshi, Dr. Kurt Francis and Patrick Salcido; Prof. Dr. Paul Dauncey for support with the DAQ system; Karsten Gadow, Uwe Cornett, Sven Karstensen, Dr. Peter